Doctoral Dissertation
博士論文

High-spatial-resolution laser ablation ICP mass spectrometry for U–Th–Pb geochronology

（U–Th–Pb 年代学のための
高空間分解能レーザーアブレーション ICP 質量分析法）

A Dissertation Submitted for the Degree of Doctor of Science
December 2023
令和５年１２月博士（理学）申請

Department of Chemistry, Graduate School of Science,
The University of Tokyo
東京大学大学院理学系研究科化学専攻

Sota Niki
仁木　創太

Abstract

Age data from rock and mineral samples can provide key information to understand the hidden and underlying order in the world. Geochemists have not been content to see geological events as unconnected and inexplicable, and thus, they are still keen to obtain precise and accurate age data from the rock and mineral samples. Among these, many geochemists, environmental chemists, and geologists are increasingly interested in geological events that operated at Quaternary period as a diagnostic of rapid changes in environmental dynamics. For the age determinations of Quaternary samples, U-series isotope systematics is particularly important to derive reliable age data concerning multiplicated rock-forming processes through magmatism. Among U-series isotopes, the radioisotope dating method based on ^{230}Th (i.e., ^{238}U–^{230}Th dating method) with the half-life of about 75 thousand years is useful to understand the millennial-scale evolution of igneous activities, especially involved in felsic magmatism. To do this, mass spectrometric techniques utilising the atmospheric pressure plasma as an ion source (ICP-MS) is a principal choice for radioisotope dating. Combination of the ICP-MS and laser ablation (LA) sampling technique enables us to derive age data from specific minerals, obviating the risk of contamination and analysis of secondary minerals during the age determinations of individual grains having sub-grain-sized internal textures. Basic backgrounds of the isotope geochronology are overviewed in Chapter 1, and the fundamentals of the *in situ* dating method based on U–series isotope systematics are described in Chapter 2.

Based on the elemental/isotopic analyses from bulk samples, it is widely recognised that the resulting radioisotope age can be erroneous because most of the rocks are potentially the mixture of various minerals/phases having different ages. Age determinations from specific minerals/phases are very important to understand the meaning of "age" of samples as reflecting various geological events. To achieve this, many geologists or geochemists are interested in age determinations using a high

sensitivity *in situ* analytical technique. In last decades, data quality obtained by the LA-ICP-MS is dramatically improved. However, there remains several analytical challenges to improve data quality, especially for age determinations for young samples including Quaternary rocks. The major analytical errors in the age determinations are mass spectrometric and non-spectral interferences ubiquitously found in most mass spectrometers. Contribution of these interferences was carefully investigated and minimised through the rigorous testing of the age data (Chapter 3).

The level of the non-spectral interference can be well documented by the elemental/isotopic ratios (e.g., Pb/U or Pb/Th). The deviations of the isotope ratio data from true values are the major source of systematic errors in the age determinations, and the contribution of the non-spectral interference found in LA-ICP-MS is discussed in the section 3.2. The measured Pb/Th values can be different even under the identical system setup and operational conditions. The magnitude of deviations in the elemental ratio values are dependent upon various conditions such as physicochemical properties (e.g., volatility) of elements or sample matrices, and thus, the incomplete correction of the mass bias and fractionation effects causes systematic errors in the measured ages. In this study, the physicochemical processes of analytes during the laser ablation process were investigated through a high-speed analysis of $^{208}Pb/^{232}Th$ from individual particles generated by femtosecond LA. Hence, the combination of newly developed high-time-resolution multiple-collector ICP-MS and micron-resolution femtosecond LA systems was used in this study. The measured particles have two decoupled $^{208}Pb/^{232}Th$ compositions of Pb-bearing particles and Pb-depleted particles. The particles enriched in volatile elements (i.e., Pb) are the condensates from laser-induced gas phases, whereas the particles depleted in Pb are originating from molten regions where volatile components including Pb were effectively lost through the laser-induced vaporisation. The production of molten samples also induces the release of large-sized sample particles. The injection of large-sized sample particles causes the analytical errors in Pb/Th measurements because of contribution of the counting loss of ^{232}Th due to the extended refresh time (i.e., detector dead time). The difference in the proportion (mass fraction) of the Pb-enriched and Pb-depleted (Th-enriched) particles is severely dependent upon various parameters such as (a) chemical feature of the elements, (b) chemical composition of samples, and (c) physical properties of solid materials, and thus, matrix-matched

calibration references are required for the reliable correction of the mass bias and fractionation effects found in LA-ICP-MS.

Another source of analytical errors is the mass spectrometric interference on analyte ions. The mass spectrometric interference at *m*/*z* 230 and the developed analytical protocol for reducing them are discussed in the section 3.3. The major interfering ions are Zr-related polyatomic ions (e.g., $Zr_2O_3^+$), and the tailing from adjacent peaks, such as $^{232}Th^+$. The Zr-related polyatomic ions are especially important for *in situ* analysis of zircon. In this study, the kinetic energy discrimination (KED) based on collision cell technique equipped with quadrupole-based MS is utilised for selective removal of interfering ions while keeping the ion transmission of Th. After the optimisation of the KED condition, the contribution of mass spectrometric interference was reduced to a negligible level. Hence, the *in situ* $^{238}U-^{230}Th$ dating method using LA-ICP-MS can be conducted without interference correction scheme used in the conventional system setup, resulting in the better accuracy of age determination.

Another important issue to derive the reliable age data from geological samples is to avoid elemental/isotopic analysis from inappropriate areas through careful observations of zoning textures. Mineral samples formed through multiplicated magmatic events can retain multiple chronological information preserved in each growth texture corresponding to each event. To resolve micron-scaled growth textures inside minerals, high-spatial elemental imaging analysis is necessary for observing the internal structures and deciphering the formation processes in terms of geochemical contexts. In this study, the micron-resolution femtosecond laser ablation system was developed, and the technique was applied to trace-element imaging analysis of zircon with the spatial resolution of 2 μm. In the section 3.4, the improved spatial resolution of trace-element maps is demonstrated compared to the elemental maps obtained by the conventional LA system. Moreover, based on the high-resolution elemental images, the correlation between U and Th concentrations can be useful for understanding the multiple formation processes of minerals.

For the geochronological application of the developed techniques through the investigation on the analytical issues, *in situ* $^{238}U-^{230}Th$ dating of zircon separated from a Holocene rhyolite sample occurring in Mt. Tenjo, Kozushima was carried out in Chapter 4. Prior to the age determination, high-spatial-resolution elemental imaging analysis was

performed, and based on the obtained elemental images, the zircons demonstrate the zoning texture of the core with low concentrations of incompatible elements and the rim with high concentrations of them. The separate age determinations were conducted for the core and the rim, and the resulting $^{238}U–^{230}Th$ ages were 17 ± 5 ka (1s) and 5 ± 4 ka (1s), respectively. In spite of the large uncertainty of the acquired ages, the age data suggest the older stage of the core formation prior to the eruption timing of 1.2 ka. The obtained results for $^{238}U–^{230}Th$ ages in this study indicate the importance of the developed methods using high-spatial-resolution LA-ICP-MS for the combined approach based on elemental imaging analysis and *in situ* $^{238}U–^{230}Th$ age determination.

Contents

1. General introduction to chronology **1**

1.1 Basic principles of radioisotope dating methods 2

1.2 U–Pb and Th–Pb isotope systematics 5

1.3 Quaternary geochronology based on U-series isotope systematics 11

1.4 U-series isotope systematics in zircon and monazite 13

2. Fundamentals of analytical methods for U-series isotopes **16**

2.1 Conventional techniques for U-series isotopic analysis 17

2.2 Inductively coupled plasma mass spectrometry (ICP-MS) 21

2.3 *In situ* sampling method using laser ablation (LA) 24

2.4 Analytical challenges 27

3. Analytical challenges with LA-ICP-MS **30**

3.1 Big lesson for better results 31

3.2 Non-spectral interference caused by laser ablation 34

3.2.1 Background of non-spectral interference 34

3.2.2 Experimental 42

3.2.2.1 Instrumentation 42

3.2.2.2 Scheme for data reduction of time-resolved isotope signals 46

3.2.3 Results and discussion 47

3.2.3.1 Multiple isotope signal profiles of single-shot laser ablation with high-time-resolution analysis 47

3.2.3.2 Fractionation of $^{208}Pb/^{232}Th$ through evaporation/recondensation processes 53

3.2.4 Conclusion 57
3.3 Mass spectrometric interference 58
3.3.1 Introduction 58
3.3.1.1 Mass spectrometric interferences on *m*/*z* 230 58
3.3.1.2 Enhancement of SBR 61
3.3.2 Experimental 63
3.3.2.1 Optimisation of instrumental conditions 63
3.3.2.2 Reference materials and Quaternary samples 68
3.3.2.3 Calculation Procedures 69
3.3.3 Results and discussion 72
3.3.3.1 Evaluation of data quality 72
3.3.3.2 ^{238}U-^{230}Th ages of Quaternary samples 74
3.3.4 Conclusive remarks 78
3.4 High-spatial-resolution elemental imaging technique 80
3.4.1 Introduction 80
3.4.2 Experimental 83
3.4.2.1 Instrumentations and system setup 83
3.4.2.2 Reference materials and the measured zircon sample 88
3.4.2.3 Data reductions 89
3.4.3 Results and discussion 90
3.4.3.1 Analytical capability of the micron-resolution LA system 90
3.4.3.2 Visualisation of data obtained from imaging analysis of the Ashizuri zircon 92
3.4.3.3 Correlation analysis of elemental abundances 96
3.4.4 Conclusion 98

4. Geochronological application 99

4.1 Introduction to magmatism in intra-oceanic arc systems 100
4.2 Experimental 102
4.2.1 Sample preparation of zircon 102
4.2.2 Experimental conditions of trace-element imaging analysis 102
4.2.3 Experimental conditions of ^{238}U–^{230}Th age determination 103

4.3 Results and discussion 103
4.3.1 Internal zoning textures of zircon 103
4.3.2 ^{238}U–^{230}Th ages of zircon 104
4.4 Conclusion 105

5. Summary and outlook **112**

List of acronyms

CCT: Collision cell technique

CL: Cathodoluminescence

EPMA: Electron probe microanalysis

fsLA: Femtosecond laser ablation

FT: Fission-track

HTR: High time resolution

ID-TIMS: Isotope dilution-thermal ionisation mass spectrometry

ICP-MS: Inductively coupled plasma mass spectrometry

ICP-Q-MS: Quadrupole-based inductively coupled plasma mass spectrometry

ICP-SF-MS: Sector field-based inductively coupled plasma mass spectrometry

KED: Kinetic energy discrimination

LA: Laser ablation

LA-ICP-MS: Laser ablation inductively coupled plasma mass spectrometry

Ln: Lanthanides

MC-ICP-MS: Multiple-collector inductively coupled plasma mass spectrometry

MS: Mass spectrometry

SBR: Signal-to-background ratio

SEM: Secondary electron microscopy

SEM-EDS: Secondary electron microscopy-energy-dispersive X-ray spectroscopy

SEM-WDS: Secondary electron microscopy-wavelength-dispersive X-ray spectroscopy

SHRIMP: Sensitive high resolution ion microprobe

SIMS: Secondary ionisation mass spectrometry

TIMS: Thermal ionisation mass spectrometry

Chapter 1
General introduction to chronology

述往事 思来者--- 司馬遷.[1)]

This phrase refers to the recounting of the past and pondering of the future. This comes from Shiji written by Sima Qian during the era of the Han dynasty in China and demonstrates his approach to writing the historical record. Since ancient times, humans have sought to comprehend the past and anticipate the future, and this leads to the creation of historical records. However, no direct evidence predating human civilisations exists in historical records. Decoding the history of the Earth requires deriving chronological information from natural things formed through ancient natural events occurring in the history of the Earth. For this purpose, absolute age determination through radioisotope dating methods become essential.

1.1 Basic principles of radioisotope dating methods

Radioisotope dating methods are based on radioactive decay of unstable isotopes with the constant unique decay rates of each isotope.[2)] Owing to the constant decay rates of radioactive nuclides, chronological information can be derived from the number of surviving parent isotopes and produced daughter isotopes after the timings of separation of parent and daughter isotopes by geological and cosmological processes, such as melting, vaporisation, and crystallisation. The numeric description of the law of the radioactive decay is described in the following equation (1.1–1.6).

$$\frac{dN_p}{dt} = -\lambda N_p \tag{1.1}$$

where N_p is the number of a parent isotope, t is time, and λ is the decay constant of the parent isotope.

$$N_p = N_{p\,t=0} e^{-\lambda t} \tag{1.2}$$

where $N_{p\,t=0}$: the number of a parent isotope at the initial state. The number of a daughter isotope (N_d) derived from the radioactive decay is denoted by the equation (1.3).

$$N_d = N_{p\,t=0}(1 - e^{-\lambda t}) \tag{1.3}$$

The ratio of the numbers of parent and daughter isotopes is expressed by the following equation (1.4).

$$\frac{N_d}{N_p} = e^{\lambda t} - 1 \tag{1.4}$$

The equation (1.4) is used for age calculation from isotope ratios in the case of the absence in the non-radiogenic daughter isotope. When the non-radiogenic daughter isotope is present at the initial state, the number of a daughter isotope (N_d) is represented by the following equation (1.5) using the number of daughter isotope at the initial state ($N_{d\,t=0}$), and the equation (4) can be converted to the equation (1.6).

$$N_d = N_{d\,t=0} + N_{p\,t=0}(1 - e^{-\lambda t}) \tag{1.5}$$

$$\frac{N_d}{N_p} = \frac{N_{d\,t=0}}{N_p} + e^{\lambda t} - 1 \tag{1.6}$$

Thus, when the presence of the initial daughter isotope is not negligible, the estimation of $\frac{N_{d\,t=0}}{N_p}$ is required for the age calculation.

For decoding the Earth's history through 4.5 billion years, radioisotope dating methods have been used for age determinations of geological and cosmological samples. The radioactive elements and daughter elements commonly used for geo- and cosmo-

chronology are summarised in Fig. 1.1.

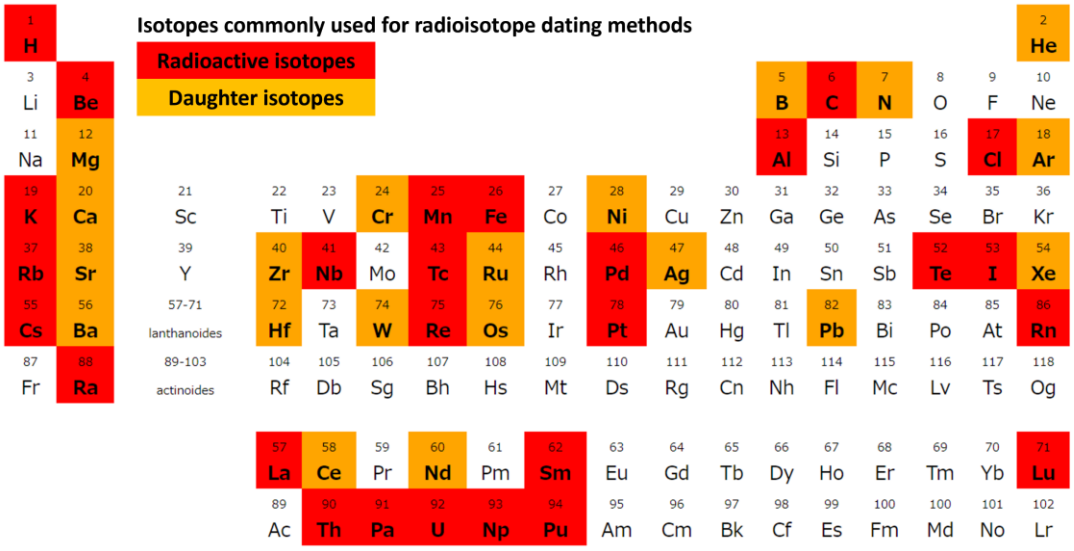

Figure 1.1 Radioactive isotopes commonly used for geo- and cosmo-chronology. Elements coloured in red and orange on the periodic table are those with radioactive isotopes and daughter isotopes, respectively.

In chronological studies, development of dating methods for young geological samples is increasingly important. Based on the age determination of young geological samples, high temporal resolution data can be derived, and this is important for understanding the mechanisms of geological processes based on the high-time-resolution sequences. For instance, when the age of a sample 100 thousand years ago (i.e., 100 ka) is determined by the precision of the isotope ratios with 10%, the resulting uncertainty accompanied with the radioisotope age is ten thousand years, while the resulting age uncertainty is identical for the age determination of a 1 billion-year-old sample (i.e., 1 Ga) with a high level of precise isotope analysis used in chronological studies (0.1%). Based on the age determination of young samples, the absolute temporal resolution to trace the time evolution of geological processes can be improved even when the relative uncertainty of parent–daughter isotope ratios is large.

When utilising the radioactive nuclides, the accumulated amounts of isotopes from radioactive decay is less for geological samples with younger ages. Therefore, for age determination, detecting subtle deviations of the isotope ratios from the stable or natural isotope ratios without the accumulation of the daughter nuclides is required. For

instance, the applications of the K–Ar isotope system for geological samples with the younger ages than 100 ka is practically difficult due to the contamination of Ar from air, and the previously reported cases are limited.[3] Hence, for age determinations of young samples with the ages of younger than 100 ka, the radioactive nuclides with the short half-lives less than 100 thousand years is important because of large variations in the time-dependent isotope ratios involved in the radioactive decay. Among the radioisotope with the short half-lives, ^{14}C with the half-life of about 5730 years is commonly used.[4] However, the ^{14}C dating method has limitations in terms of applicable materials. For the application of the ^{14}C dating method, samples containing ^{14}C should be experienced to an isotopic equilibrium of ^{14}C with atmospheric CO_2 in air, indicating that the dating method can provide chronological information for only geological phenomena recorded as changes of surface environments on the Earth. Thus, the radiocarbon dating method cannot be applied to the samples without containing ^{14}C inside the Earth, which is critical for elucidating hidden geological processes, such as rock-forming processes of magmatism and metamorphism, or seismological activities.

Especially for magmatic processes, even during dormant phases of eruptive activities, magmatic processes including generation, exhumation, storage, cooling and solidification of magma in the mantle and crust can continue, and the timescales of them are key issues for understanding the pre-eruptive phases.[5] Despite the importance of age determinations of eruption times based on the radiocarbon ages recorded as the surface changes, the whole magmatic activities inside the Earth during the dormant phases are not recorded in surface environments, and other dating methods for understanding these processes are necessary.

The time intervals of eruptions at a single volcano are ranging from 0 to 10^6 years, and the longer repose time is basically observed in volcanoes having more acidic magma.[6] The long hiatus of more than 10^3 years for felsic magmatism is attributed to several factors, such as high viscosity resulting in more time for movement of magma, and required time for differentiation due to fractional crystallisation, or changes in chemical compositions through the assimilation of surrounding country-derived rocks.[6] However, the exact reasons remain unclear, and the contribution of each factor may change depending on volcanoes. To resolve the processes hidden inside the Earth, chronological information prior to eruption events is necessary, and age determinations

should be conducted for phenocrysts formed in magma reservoirs reflecting the mineral-forming processes including generation, exhumation, injection, subsequent cooling and solidification of magma. Therefore, radioisotope dating methods of minerals with the temporal resolution ranging from 10^3 to 10^4 is required for elucidation of felsic-magma processes.

1.2 U–Pb and Th–Pb isotope systematics

Age determinations of young geological samples with the temporal resolution of 10^3–10^4 years can be conducted with the radioisotope dating methods using short half-lives. Most radioisotopes with the short half-lives are cosmogenic nuclides, such as ^{10}Be and ^{14}C, generated by interaction with high-energy cosmic rays in surface environments on the Earth,[7, 8] and magma and minerals crystallised from magma essentially contain undetectable amounts of them. Except for them, detectable amounts of ^{231}Pa, ^{230}Th, and ^{226}Ra belonging to the decay chains starting from ^{238}U and ^{235}U are contained in rock and mineral samples because of the abundance of U being ca. 1 μg g^{-1} for typical rocks, [9] and hence, these nuclides are practically the only candidates utilised for direct radioisotope dating of young rock and mineral samples, although they are still trace amounts to detect and highly sensitive analytical methods are required.

Uranium-238 and uranium-235 are the radioactive isotopes,[10] with which the uranium decay series and actinium decay series start, and, in addition to them, thorium-232 is also the starting point of the thorium decay series,[11] and three decay series shown in Fig. 1.2 are utilised for radioisotope dating methods since the early ages of chronological studies.[12, 13] In common with these decay series, the final products via multiple steps of radioactive decay are Pb isotopes of ^{206}Pb, ^{207}Pb, and ^{208}Pb, and conventionally radioisotope ages are calculated from ^{206}Pb/^{238}U, ^{207}Pb/^{235}U, and ^{208}Pb/^{232}Th based on the following equations (1.7–1.9) based on the equation (1.4) assuming the negligible contribution of the non-radiogenic Pb.

$$\frac{^{206}\mathrm{Pb}}{^{238}\mathrm{U}} = e^{\lambda_{238}t} - 1 \tag{1.7}$$

$$\frac{^{207}\mathrm{Pb}}{^{235}\mathrm{U}} = e^{\lambda_{235}t} - 1 \tag{1.8}$$

$$\frac{^{208}\mathrm{Pb}}{^{232}\mathrm{Th}} = e^{\lambda_{232}t} - 1 \qquad (1.9)$$

The decay constants for ^{238}U, ^{235}U, and ^{232}Th are represented as λ_{238}, λ_{235}, λ_{232}, respectively. Especially for the uranium series and actinium series, two radioisotope ages are identically calculated based on two Pb/U values (^{206}Pb/^{238}U and ^{207}Pb/^{235}U), and the concordance of two ages can be evaluated through a diagram where the ^{207}Pb/^{235}U and ^{206}Pb/^{238}U values are plotted on the X and Y axis (i.e., the Wetherill concordia diagram).[14] The Wetherill concordia diagram is useful for evaluating the contribution of secondary loss and gain, or initial incorporation of Pb, and deriving reliable radioisotope ages.

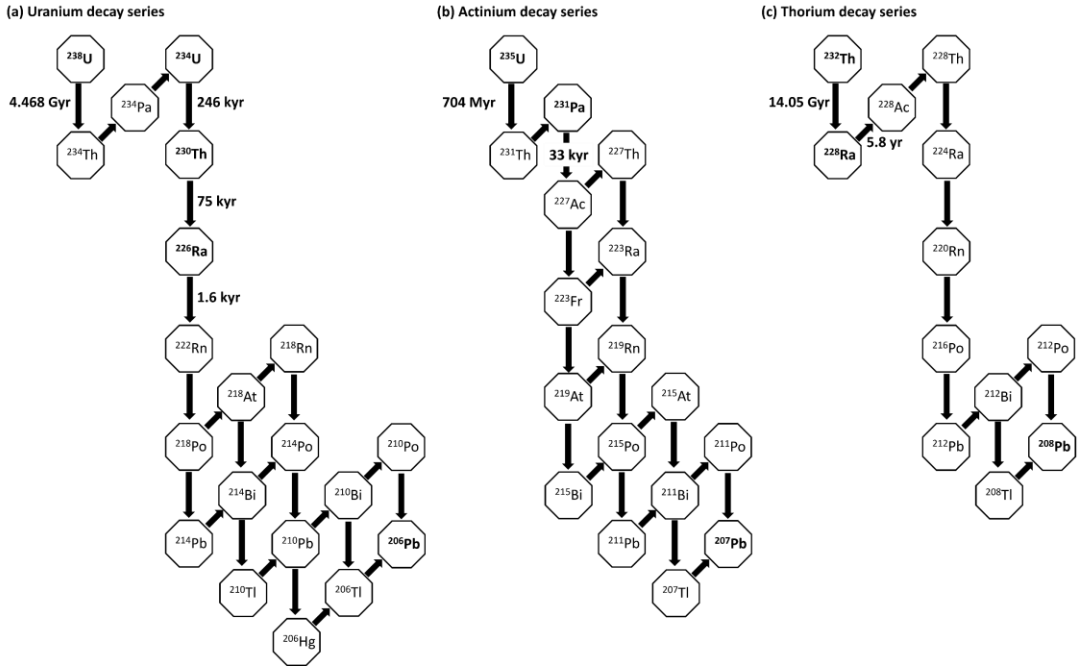

Figure 1.2 Schematic diagram of the decay chains beginning from (a) ^{238}U, (b) ^{235}U, and (c) ^{232}Th.[15] For the nuclide with the longer half-lives than 1 year, the half-lives are noted.

For age determinations on young samples, the contribution of the radioactive disequilibria for the intermediate nuclides to the isotope ratios can be significant even with low precision measurements.[16, 17] The radioactive disequilibria mean the state of unbalanced radioactivity among parent isotopes and the intermediate products and decrease or accumulation of the intermediate products continues until the steady state where the radioactivity is balanced (i.e., secular equilibrium).[18, 19] The isotope ratios in secular equilibria are approximately calculated from the ratio of the decay constants. The

radioactive disequilibria result in the excess or depleted amount of radiogenic Pb accumulated by radioactive decay compared to the amount calculated from the equation (1.7–1.9), causing the significant deviation of reckoned radiometric ages from the true values (Fig. 1.3).[16, 17] Among the intermediate nuclides, ^{234}U and ^{230}Th belonging to the uranium decay series, and ^{231}Pa belonging to the actinium decay series are important because of the longer half-lives of more than ten thousand years. For ^{234}U, which has the longest half-life among the intermediate products, the isotope fractionation of ^{238}U/^{234}U during high-temperature igneous processes can be negligible and the contribution of the disequilibrium related to ^{234}U can be ignored in usual volcanic rocks, except for altered rocks potentially demonstrating ^{234}U/^{238}U values in radioactive disequilibrium due to the interaction with aqueous phases[20, 21]. For ^{230}Th and ^{231}Pa demonstrating different chemical features from U, depletion or enrichment of ^{230}Th/^{238}U or ^{231}Pa/^{235}U occurs when minerals crystalise in a magma reservoir.[22, 23] To quantify the isotope ratios in the radioactive disequilibria, ^{230}Th can be denoted as the following equations (1.10−1.20).

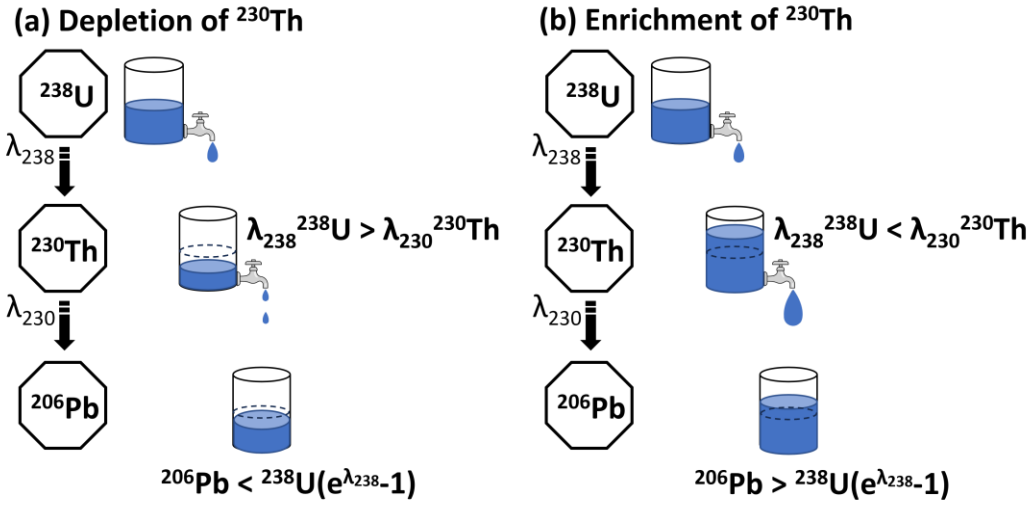

Figure 1.3 Schematic diagram of (a) smaller ^{206}Pb/^{238}U value and (b) larger ^{206}Pb/^{238}U value compared to the value defined from the equation (1.7) due to the ^{230}Th-depleted and ^{230}Th-enriched initial radioactive disequilibria, respectively.

For intermediate products of the decay series, both the decrease of the number of atoms by radioactive decay of themselves and increase of the number of atoms by input from the radioactive decay of the parent isotopes are considered, and the differential equations using time derivatives for the number of ^{230}Th atoms are expressed by the

following equations (1.10).

$$\frac{d^{230}\mathrm{Th}}{dt} = -\lambda_{230}{}^{230}\mathrm{Th} + \lambda_{238}{}^{238}\mathrm{U} \tag{1.10}$$

where λ_{230}: the decay constant of ^{230}Th.

Based on the equation (1.2), the number of ^{238}U atoms is represented by the equation (1.11) using the number of ^{238}U atoms at the initial state as $^{238}\mathrm{U}_0$.

$$^{238}\mathrm{U} = {}^{238}\mathrm{U}_0 e^{-\lambda_{238}t} \tag{1.11}$$

By solving the differential equation with the substitution of ^{238}U using the equation (1.11), the number of ^{230}Th is represented by the following equation (1.12).

$$^{230}\mathrm{Th} = {}^{230}\mathrm{Th}_0 e^{-\lambda_{230}t} + \frac{\lambda_{238}}{\lambda_{230}-\lambda_{238}}{}^{238}\mathrm{U}_0\left(e^{-\lambda_{238}t} - e^{-\lambda_{230}t}\right) \tag{1.12}$$

where $^{238}\mathrm{U}_0$ is the number of $^{230\mathrm{Th}}$ at the initial state.

The ^{206}Pb at $t = T$ is represented by the integration of the radioactivity for ^{230}Th as the following equation (1.13) when the radioactive disequilibria for other intermediate products are ignored.

$$^{206}\mathrm{Pb} = \int_0^T \left(\lambda_{230}{}^{230}\mathrm{Th}\right) dt \tag{1.13}$$

By dividing both the right and left sides of the equation (1.13) by the equation (1.11), ^{206}Pb/^{238}U is represented by the equation (1.14).

$$\frac{^{206}\mathrm{Pb}}{^{238}\mathrm{U}} = \frac{\int_0^T \left(\lambda_{230}{}^{230}\mathrm{Th}\right) dt}{^{238}\mathrm{U}_0 e^{-\lambda_{238}T}} \tag{1.14}$$

By performing the integral calculation, ^{206}Pb/^{238}U is formalised through the equation (1.15).

$$\frac{^{206}\mathrm{Pb}}{^{238}\mathrm{U}} = \frac{\lambda_{230}}{\lambda_{230}-\lambda_{238}}\left(e^{\lambda_{238}T}-1\right) + \left(\frac{^{230}\mathrm{Th}_0}{^{238}\mathrm{U}_0} - \frac{\lambda_{238}}{\lambda_{230}-\lambda_{238}}\right)\left(1-e^{-\lambda_{230}T}\right)e^{\lambda_{238}T} \tag{1.15}$$

The equation (1.15) has two variables of T and $^{230}\mathrm{Th}_0/^{238}\mathrm{U}_0$, and T cannot be determined to a unique solution. Then, the estimation of $^{230}\mathrm{Th}_0/^{238}\mathrm{U}_0$ or the direct measurement of $^{230}\mathrm{Th}_0/^{238}\mathrm{U}_0$ are required.

When ^{238}U–^{206}Pb dating of minerals crystallised from magma is conducted, the initial ^{230}Th/^{238}U is represented by the multiplication of the ratio of partition coefficients for Th and U between the mineral and the magma ($D_{\mathrm{Th/U}}$), and the initial ^{230}Th/^{238}U of the magma expressed by the following equation (1.16).

$$\frac{^{230}\mathrm{Th}_0}{^{238}\mathrm{U}_0} = D_{\mathrm{Th/U}} \times \left(\frac{^{230}\mathrm{Th}_0}{^{238}\mathrm{U}_0}\right)_{\mathrm{magma}} \tag{1.16}$$

Based on the assumption of the crystallisation of minerals from the magma in secular equilibrium, the initial $^{230}Th/^{238}U$ of the magma is the secular equilibrium value represented by the following equation (1.17).

$$\left(\frac{^{230}\mathrm{Th}_0}{^{238}\mathrm{U}_0}\right)_{\mathrm{magma}} = \lim_{t\to\infty}\frac{^{230}\mathrm{Th}}{^{238}\mathrm{U}} = \frac{\lambda_{238}}{\lambda_{230}-\lambda_{238}} \quad (1.17)$$

Subsequently, based on the equation (1.16) and (1.17), the initial $^{230}Th/^{238}U$ of the mineral can be described as the following equation (1.18).

$$\frac{^{230}\mathrm{Th}_0}{^{238}\mathrm{U}_0} = D_{\mathrm{Th/U}} \times \frac{\lambda_{238}}{\lambda_{230}-\lambda_{238}} \quad (1.18)$$

By substituting the equation (1.18) into the equation (1.15), the equation (1.19) is obtained.

$$\frac{^{206}\mathrm{Pb}}{^{238}\mathrm{U}} = \frac{\lambda_{230}}{\lambda_{230}-\lambda_{238}}\left(e^{\lambda_{238}T}-1\right) + \frac{\lambda_{238}}{\lambda_{230}-\lambda_{238}}\left(D_{\mathrm{Th/U}}-1\right)\left(1-e^{-\lambda_{230}T}\right)e^{\lambda_{238}T} \quad (1.19)$$

The first term is almost the same as the equation (1.7). The second term indicates the contribution of the initial ^{238}U–^{230}Th disequilibrium and corresponds to the correction term. For Th-depleted minerals ($D_{\mathrm{Th/U}} < 1$), the $^{206}Pb/^{238}U$ values are less than that in secular equilibrium, and for Th-enriched minerals, the $^{206}Pb/^{238}U$ values are more than that in secular equilibrium.

The similar equation to the equation (1.19) is deduced for the ^{235}U–^{207}Pb system with the ^{235}U–^{231}Pa disequilibrium as the following equation (1.20).

$$\frac{^{207}\mathrm{Pb}}{^{235}\mathrm{U}} = \frac{\lambda_{231}}{\lambda_{231}-\lambda_{235}}\left(e^{\lambda_{235}T}-1\right) + \frac{\lambda_{235}}{\lambda_{231}-\lambda_{235}}\left(D_{\mathrm{Pa/U}}-1\right)\left(1-e^{-\lambda_{231}T}\right)e^{\lambda_{235}T} \quad (1.20)$$

where λ_{230} is the decay constant of ^{231}Pa, and $D_{\mathrm{Pa/U}}$ is the ratio of partition coefficients for Pa and U between the mineral and the magma.

The equations (1.19) and (1.20) are important especially for accurate U–Pb dating of Quaternary samples.[17] Figure 1.4 shows the actual U–Pb isotope ratios obtained from the spot analyses of Quaternary zircon grains collected from the Bishop tuff (ca. 0.77 Ma)[17] plotting on the Wetherill concordia diagram. On the diagram, two concordia curves with and without consideration of the initial disequilibria are plotted based on the equations (1.7), (1.8), (1.19) and (1.20) as demonstrating the isotope ratios without the contribution of non-radiogenic Pb. For the U–Pb systems in zircon demonstrating the $D_{\mathrm{Th/U}}$ = 0.14 ± 0.02 and the $D_{\mathrm{Pa/U}}$ = 3.36 ± 0.40 (the coverage factor: k=2),[24, 25] the resulting concordia curve deviates from the curve without considering the disequilibria. The notable thing is that the uncertainty accompanied with the partition coefficient ratios

can be the source of systematic errors corresponding to about three thousand years and ten thousand years for ^{238}U–^{206}Pb ages and ^{235}U–^{207}Pb ages. The data points in Fig. 1.4 are distributed to the right off the disequilibrium-corrected concordia curve, and the leftmost data point is on the disequilibrium-corrected concordia curve. The absence of the data points to the left of the disequilibrium-corrected concordia curve indicates the significant contribution of the initial disequilibria in zircon as also mentioned in previous studies.[16], [17] The dispersion of the data points for the right direction is a contribution of non-radiogenic Pb, which is not involved in radioactive decay. The non-radiogenic Pb is derived from several sources, such as initially incorporated Pb inside the mineral sample, Pb contained in inclusion phases inside samples, contaminated Pb during sample preparation, and Pb blank of the analysis system. The less contribution of the non-radiogenic Pb is desired for more accurate and precise age determination. Practically, by using the correction methods for the contribution of the initial radioactive disequilibria and the non-radiogenic Pb, age determinations based on the U–Pb isotope systems can be conducted for zircon with the crystallisation ages of older than 100 ka.[25] For age dating of further younger samples, the lowering of the accuracy and precision with the radioisotope ages is essentially inevitable based on the U–Pb isotope systems due to the more contribution of the initial disequilibria and the non-radiogenic Pb.

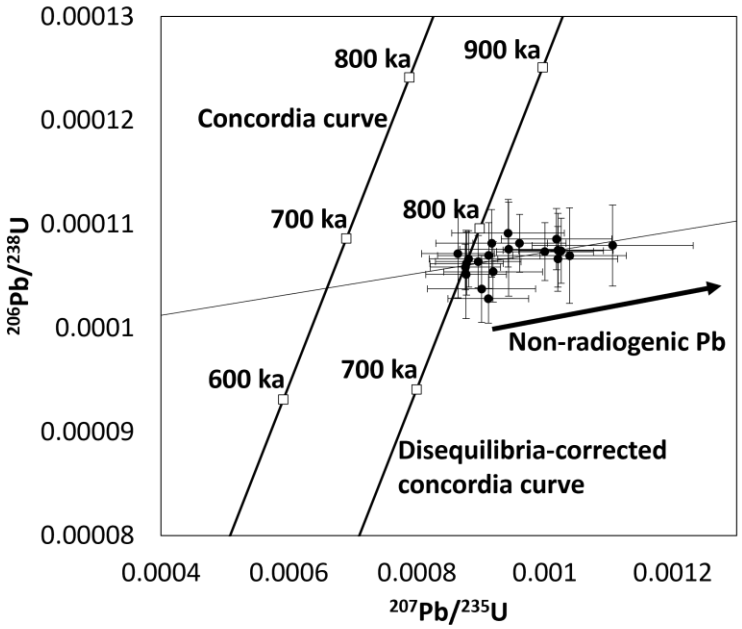

Figure 1.4 The U–Pb isotope ratios of the Bishop tuff zircon (0.77 Ma) plotting on the Wetherill concordia diagram. The uncertainty ranges with each data points are 2s. The left concordia curve is calculated without the contribution of the initial radioactive disequilibria, and the right concordia curve is reckoned based on the corrected Pb/U values for the initial radioactive disequilibria in the ^{238}U–^{230}Th–^{206}Pb and ^{235}U–^{231}Pa–^{207}Pb systems. The straight line is the regression line of the data points.

1.3 Quaternary geochronology based on U-series isotope systematics

There are two options for avoiding the systematic errors derived from radioisotope ages based on the U–Pb systems. The first option is using the ^{232}Th–^{208}Pb system instead of the U–Pb isotope systems. The ^{232}Th decay series does not have long-lived intermediate products with the half-lives of more than 10 years, and radiogenic $^{208}Pb/^{232}Th$ ratios can be directly converted to the radioisotope ages with the systematic error of only a few tens of years.[26] By using this scheme, Sakata and the co-authors reported the accurate ages of Quaternary zircons.[17] Despite the negligible contribution of the initial radioactive disequilibria, the non-radiogenic Pb can be significant for the resulting isotope ratios as well as the U–Pb systems, and the precise determination of Pb isotope ratios and the reduction of the non-radiogenic Pb should be required for the age determinations of further younger samples. Compared to zircon demonstrating the low

partition coefficient of Th than U, the ^{232}Th–^{208}Pb dating method can be more suitable for age determination of monazite, which is a Th-enriched mineral.

The second scheme is deriving chronological data based on the direct measurements of the intermediate products belonging to the U-series decay chain.[27] Among the intermediate products involved in the radioactive disequilibria in igneous systems, ^{230}Th with the half-life of 75584 ± 110 years[28] is suitable for deciphering felsic magmatism with the long reposed times ranging from 10^3–10^6 years.[5, 6]

The principle of the radioisotope dating method using ^{230}Th (i.e., ^{238}U–^{230}Th dating method) is governed by the following equations (1.21–1.25). By dividing both the left and right sides of the equation (1.12) by ^{232}Th, the following equation (1.21) is obtained.

$$\frac{^{230}\mathrm{Th}}{^{232}\mathrm{Th}} = \frac{^{230}\mathrm{Th}_0}{^{232}\mathrm{Th}} e^{-\lambda_{230}t} + \frac{\lambda_{238}}{\lambda_{230}-\lambda_{238}}\left(1 - e^{-(\lambda_{230}-\lambda_{238})t}\right)\frac{^{238}\mathrm{U}}{^{232}\mathrm{Th}} \quad (1.21)$$

The equation (1.21) is the principle of the ^{238}U–^{230}Th isochron method. Based on the equation (1.21), for instance crystallisation of minerals at one time, the isotopic data of various minerals with different ^{238}U/^{232}Th is plotted on a straight line (Fig. 1.5(b)) owing to the slope of $\frac{\lambda_{238}}{\lambda_{230}-\lambda_{238}}\left(1 - e^{-(\lambda_{230}-\lambda_{238})t}\right)$ in the equation (1.21) uniquely determined from time.

Based on the division of the equation (1.12) by ^{238}U using the equation (1.11), the obtained equation (1.22) represents the time-dependent changes of ^{230}Th/^{238}U.

$$\frac{^{230}\mathrm{Th}}{^{238}\mathrm{U}} = \frac{^{238}\mathrm{Th}_0}{^{238}\mathrm{U}_0} e^{-(\lambda_{230}-\lambda_{238})t} + \frac{\lambda_{238}}{\lambda_{230}-\lambda_{238}}\left(1 - e^{-(\lambda_{230}-\lambda_{238})t}\right) \quad (1.22)$$

The first term of the right side for the equation (1.22) indicates the contribution of the initial ^{238}U–^{230}Th disequilibria, and the second term means the input from radioactive decay of ^{238}U. Considering mineral crystallisation from magma in secular equilibrium, ^{230}Th/^{238}U of crystallised minerals can be described as the equation (1.18), and then, the following equation (1.23) and (1.24) is obtained by the substitution of the equation (1.18) into the equation (1.22).

$$\frac{^{230}\mathrm{Th}}{^{238}\mathrm{U}} = \frac{\lambda_{238}}{\lambda_{230}-\lambda_{238}} D_{\mathrm{Th/U}} e^{-(\lambda_{230}-\lambda_{238})t} + \frac{\lambda_{238}}{\lambda_{230}-\lambda_{238}}\left(1 - e^{-(\lambda_{230}-\lambda_{238})t}\right) \quad (1.23)$$

$$\frac{^{230}\mathrm{Th}}{^{238}\mathrm{U}} = \frac{\lambda_{238}}{\lambda_{230}-\lambda_{238}} + \frac{\lambda_{238}}{\lambda_{230}-\lambda_{238}}\left(D_{\mathrm{Th/U}} - 1\right) e^{-(\lambda_{230}-\lambda_{238})t} \quad (1.24)$$

Subsequently, the equation for age calculation is formulised as the following equation

(1.25).

$$t = -\frac{ln\left(\frac{\left(\frac{^{230}\mathrm{Th}}{^{238}\mathrm{U}} - \frac{\lambda_{238}}{\lambda_{230}-\lambda_{238}}\right)}{\frac{\lambda_{238}}{\lambda_{230}-\lambda_{238}}\left(D_{\mathrm{Th/U}}-1\right)}\right)}{(\lambda_{230}-\lambda_{238})} \quad (1.25)$$

The equation (1.25) is known for the equation of model age calculation based on the assumption of crystallisation from magma in secular equilibrium and a known $D_{\mathrm{Th/U}}$. Despite the potential errors derived from the assumptions, by using the equation (1.25), the ^{238}U–^{230}Th age can be calculated from a single ^{230}Th/^{238}U value acquired from a single isotope analysis without using the isochron method. The deduced equations of age calculations (1.21) and (1.25) for the isochron method and model age calculation method based on the ^{238}U–^{230}Th isotope systematics can be applied to age determinations on minerals. To derive the chronological data, U-enriched or Th-enriched minerals are important.

1.4 U-series isotope systematics in zircon and monazite

U-enriched or Th-enriched minerals are key for the ^{238}U–^{230}Th dating method because of the large deviation of the ^{238}U–^{230}Th isotope ratios demonstrated in these minerals from the ^{238}U–^{230}Th isotope ratio in secular equilibrium. As the representative U-enriched and Th-enriched minerals, zircon and monazite are essential.

Zircon is a zirconium silicate with the chemical composition of $ZrSiO_4$, and mainly occurs as an accessory mineral in various rocks, especially felsic rocks with the saturated Zr concentration.[29] Zircon is commonly used for chronological studies based on the U–Pb systems owing to the high compatibility of U, and negligible initially incorporated Pb.[30] Chronological information preserved in zircon crystals is robust against physical and chemical weathering, and as a result, at present, the oldest mineral grain found on the Earth is zircon.[31, 32] The closure temperature of the zircon U–Pb systems is higher than 800°C,[33] and the U–Pb ages of zircon is likely to reflect the timing of zircon crystallisation, even if the zircon samples experienced secondary alteration or metamorphism. This is a critical advantage of zircon for deciphering the geological processes, and, by taking the advantages in the U–Pb systems of zircon, the history of the Earth has been elucidated.

For acquiring chronological data from zircon occurring in young volcanic rocks, instead of the U–Pb systems, the ^{232}Th–^{208}Pb system is advantageous because of the negligible initial disequilibria.[17] Despite the importance of the ^{232}Th–^{208}Pb dating of zircon, the Pb isotope analysis is essentially vulnerable to the non-radiogenic Pb. The alternative approach is the ^{238}U–^{230}Th disequilibrium dating method utilising the chemical features for zircon of the high U content and the ^{230}Th-depleted initial disequilibria.[22] A typical partition coefficient value for U between zircon and melts is 100,[34] and the previously reported ratio of the partition coefficients for U and Th ($D_{\mathrm{Th/U}}$) are ranging from 0.1 to 0.3.[34, 24, 17] The less compatibility of Th into the crystal lattice of zircon is attributed to the larger ionic radius of Th^{4+} compared to U^{4+}.[34], and causes the initial ^{230}Th-depleted disequilibria at the crystallisation times.

The pioneering studies on the zircon ^{238}U–^{230}Th systematics revealed the presence of zircon grains with the older U–Th disequilibrium ages compared to the eruption timings of the host volcanic rocks.[22, 5] Owing to the high closure temperature of the ^{238}U–^{230}Th systematics, the ^{238}U–^{230}Th ages are close to the crystallisation timing of zircon inside the magma reservoirs. The first report of the significant old zircon was made by Fukuoka and Kigoshi based on the radiometric technique for counting of the radiation from ^{230}Th collected from the decomposed bulk fraction of separated zircons.[22] Then, with the development of techniques for high-spatial-resolution isotope analysis, such as secondary ionisation mass spectrometry (SIMS) and laser ablation inductively coupled plasma mass spectrometry (LA-ICP-MS),[5, 35] the age determinations can be conducted with the spatial resolution of single-grain or sub-grain levels. With the improved spatial resolution of the age determinations, the textual observations and visualisation of trace-element distributions including U and Th inside zircon grains are increasingly important for deciphering the chronological sequences of the formation processes and driving reliable chronological information.

Another important mineral is monazite, which is a rare-earth-element phosphate with the chemical composition of (La, Ce, Nd, Th)PO_4. As well as zircon, monazite is a common accessory mineral mainly occurring in felsic rocks,[36] and conventionally the ages of monazite are determined from the U–Pb and Th–Pb systems.[37] The unique feature of monazite is the high Th concentration of a several percent level, and, owing to the abundant radiogenic ^{208}Pb derived from ^{232}Th, the chronological information based on the

^{232}Th–^{208}Pb systems can be acquired from micron-spatial-resolution spot analysis.[38] Monazite has the extremely high $D_{Th/U}$, and the $D_{Th/U}$ values are ranging from 16–24 reported by Skora and Blundy,[39] and 5–30 reported by Stepanov et al..[40] By taking the unique feature of the Th-enrichment, the Y-intercept of ^{238}U–^{230}Th isochrons can be precisely determined from the isotope analysis of monazite, indicated by Niki and the co-authors.[41]

Figure 1.5(a) demonstrates the time-dependent change of ^{230}Th/^{238}U for typical zircon and monazite with the assumption of $D_{Th/U}$ and the source melt in secular equilibrium. Based on the radioactive disequilibria in zircon and monazite, the ^{238}U–^{230}Th dating method can be applied to geological samples with the age range up to ca. 500 ka. Figure 1.5(b) indicates the isochron diagram of the ^{238}U–^{230}Th dating method plotting on the hypothetical ^{238}U–^{230}Th isotope ratios for zircon and monazite. By the combination of zircon and monazite, the large variation of the X-axis on the isochron diagram results in the precise isochron age determination.

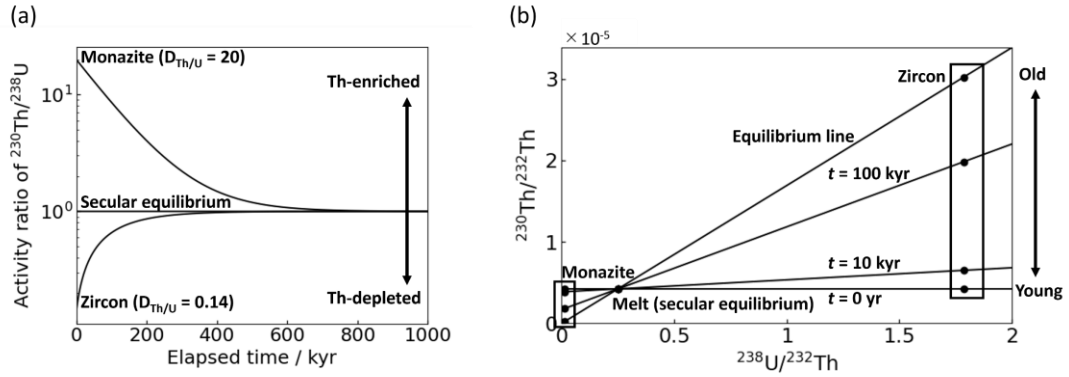

Figure 1.5 Time-dependent changes of the ^{238}U–^{230}Th ratios in zircon and monazite under the assumptions of crystallisation from magma in secular equilibrium and the $D_{Th/U}$ of 0.14 and 20 for zircon and monazite, respectively. (a) The ^{230}Th/^{238}U values of zircon and monazite are indicated. (b) the ^{238}U–^{230}Th ratios are plotted on the isochron diagram.

Chapter 2
Fundamentals of analytical methods for U-series isotopes

Measure what is measurable, and make measurable what is not so.

This was once believed to be a quote by Galileo Galilei. Despite the wide recognition, a recent study reveals that its origin is attributable to 19th-century French scholars to describe Galileo's approach to research.[42] Regardless of this, the phrase succinctly demonstrates that the development of analytical techniques is fundamental to modern science.

2.1 Conventional techniques for U-series isotopic analysis

This chapter describes the historical review of analytical methods for isotope ratios using mass spectrometry and points out the analytical challenges of present techniques for isotope analysis. Classically, U-series isotopes were measured with radiometric techniques based on direct counting of α-particles. In the early age of geochronological studies on volcanic activities based on the ^{238}U–^{230}Th dating method, age determinations were conducted using the radiometric analysis of decomposed rock samples,[27] and then, the application was extended to separated mineral fractions, such as zircon.[22] The radiometric techniques require large sample volumes and long analysis time for precise analysis. The number of ^{230}Th atoms contained in a typical zircon with the volume of 100^3 μm^3 and the uranium concentration of 100 $\mu g\ g^{-1}$ in secular equilibrium is ca. 2×10^7, and the radioactive decay occurs ca. 200 times per year based on the decay constant of 9.1706×10^{-6} yr^{-1}.[28] The analytical uncertainty principally depends on the counting statistics based on the squared root of the total counts, and the yielded low counts using the radiometric technique is critically disadvantageous, especially for separate analysis of individual mineral grains. In fact, the analysed masses used reported in the pioneering research were ranging from 2 to 130 mg obtained from the decomposition of zircon fractions,[22] which corresponds to the number of grains ranging from a few hundreds to a few hundred thousand calculated from a mass of typical zircons with the volume of 100^3 μm^3. Then, a higher-sensitivity and higher-speed analytical method compared to radiometric techniques was desired.

The direct measurements of isotopes are powerful tools instead of the radiometric techniques for improving the signal-to-background ratios (SBR) of analytes. For the direct measurements of isotopes, mass spectrometry (MS) techniques of analysing ions produced by introduction of samples into ion sources are useful. Inside mass spectrometers, ions are separated by magnetic or electric forces depending on the mass-to-charge ratios of ions, and the analysis of separate ions can be made.[43] By mass spectrometric techniques with the ion transmission of i.e., 0.1% through the MS system, for instance, the ion counts of 2×10^4 can be acquired from a single zircon grain containing the number of ^{230}Th atoms of ca. 2×10^7, and the analytical uncertainty accompanied with the $^{230}Th/^{232}Th$ values is much better than the radioactivity ratios of $^{230}Th/^{232}Th$, resulting

in precise age determinations on geological samples. Thus, nowadays, isotope analysis using mass spectrometric techniques is principal choice for ^{238}U–^{230}Th dating with faster analysis with better analytical precision.

Among mass spectrometric techniques, thermal ionisation mass spectrometry (TIMS) is the benchmark method for precise and accurate isotope analysis of solution samples. Owing to the stable ion currents produced through thermal ionisation shown in Fig 2.1(a), the highest precision of isotope measurements can be achieved by TIMS, and the radioisotope dating methods based on TIMS provide the high-resolution chronological data with the analytical precision of better than 0.1%.[44] In spite of the importance, the typical ionisation efficiency of Th using thermal ionisation is less than 0.1% because of the high boiling temperature of Th,[45] and the resulting small ion currents require a long-time analysis for high-precision isotope ratios to minimise the contribution of counting statistics to analytical uncertainty.

Another important technique is secondary ionisation mass spectrometry (SIMS). Secondary ionisation is based on the ionisation of atoms exposed to the sample surfaces using the irradiation of primary ion beams under high vacuum conditions shown in Fig. 2.1(b). In contrast to thermal ionisation, high ionisation efficiency can be achieved for elements demonstrating the refractory nature, such as Th, since the vaporisation process is not involved in the ionisation process. The resulting ionisation efficiency of Th is ca. 1%, especially when monitoring ThO^+.[46] The SIMS technique can be applied to both the bulk analysis and high-spatial-resolution analysis. Although the bulk analysis of $^{230}Th/^{232}Th$ using the SIMS technique can be carried out the irradiation of primary ion beams on carbon soaked with the sample aliquot,[47] the notable thing is that the SIMS techniques paved the way for high-spatial-resolution ^{238}U–^{230}Th age determinations on mineral samples with the careful observation of the internal textures of minerals (i.e., *in situ* ^{238}U-^{230}Th dating).[5] By scanning the focused primary ion beam, the ^{238}U-^{230}Th ages are acquired from small areas due to the advantage of high-sensitivity for Th utilising the SIMS technique. By using the SIMS technique, ^{238}U-^{230}Th ages of zircon from small areas (e.g., 20–30 μm) are acquired, and the resulting age populations of zircon grains and the statistical analysis of them are useful for reconstruction of the history of magmatic activities (e.g., time intervals of eruptions).[48]

Despite the significance of chronological data obtained by the SIMS technique,

the major problems with the SIMS technique are long analysis times (e.g., twenty minutes for one spot analysis)[46] and the necessity of careful correction for non-spectral and mass spectrometric interferences. These problems are because of the low ion density of the irradiated ion beam and incomplete ionisation. The low ionisation capacity of secondary ionisation under high-vacuum conditions with the low sampling rate is a main cause for the necessity of long-time integration of isotope signals. The nature of soft ionisation for secondary ionisation also deteriorates the analytical accuracy of isotope measurements. Through secondary ionisation, the dominant product is neutral particles, and various polyatomic ions are produced as well, in addition to the analyte ions with the yield of ca. 1%.[46] The production rates of neutral particles and many ion species vary depending on elements and sample matrices, and elemental ratios obtained from the ratios of raw signal counts for analytes significantly deviate from the true values. In case of the analysis for Pb/U well-documented in previous studies, the correction law follows a power law, and to define the accurate correction law, the wide variety of matrix-matched references is required in terms of U–Pb ages, U concentration, or crystallinity.[49] Furthermore, to ensure the accuracy of $^{230}Th/^{238}U$ analysis, careful consideration is essential regarding the contribution of mass spectrometric interferences on $^{230}Th^{16}O^{+}$, such as $Zr_2O_4^{+}$, $YbSiO_3^{+}$, or Th_2CO^{2+}, originating from the sample matrices.[46] To minimise the contribution of these interferences, data acquisition should involve a high mass resolving power (e.g., $M/\Delta M$ being more than 4000), and the reduction of the signal tailing from $^{232}Th^{+}$ is also desired. Practically, in case of using Sensitive High Resolution Ion Microprobe (SHRIMP), a complicated correction scheme is used for deriving accurate ^{238}U–^{230}Th ages.[50]

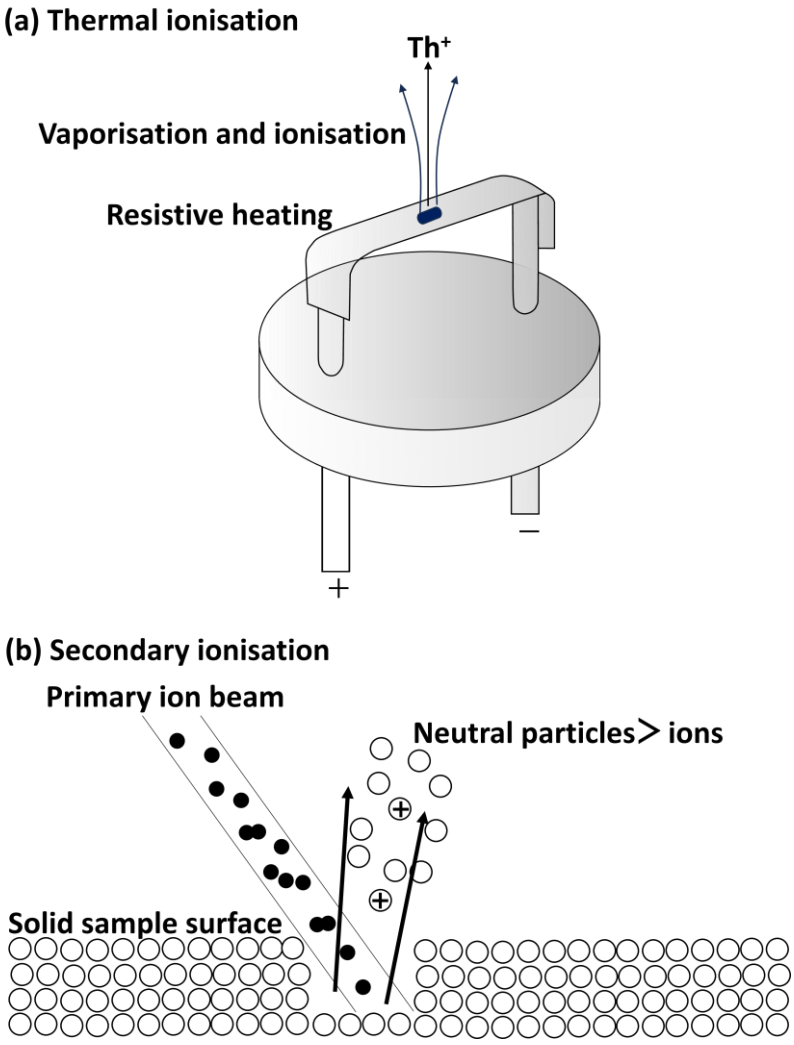

Figure 2.1 Schematic diagram of (a) thermal ionisation and (b) secondary ionisation.

2.2 Inductively coupled plasma mass spectrometry (ICP-MS)

Alternative ion sources commonly used for inorganic mass spectrometry are atmospheric plasma ion sources, especially an Ar-based inductively coupled plasma (ICP) ion source.[51] The plasma ion sources operating under atmospheric conditions have a high density of high-temperature particles involved in ionisation, and this is a critical advantage in a few orders of magnitude of larger ion capacity defined by the number of high-temperature particles comprising the plasma compared to other ion sources including primary ion beams used for secondary ionisation under high-vacuum conditions. A typical Ar-based ICP ion source uses 15 L min^{-1} of Ar under the atmospheric pressure corresponding to the number of Ar atoms nearly equal to the order of magnitude of the Avogadro's number (6.02214076×10^{23}), and that of Ar^+ as ca. 10^{19} based on the assumption of the percentage of the ionised particles 0.04%.[52]

The resulting temperatures of the ICP are important for ionisation efficiency. Sample materials introduced into the ICP are firstly desolvated, molten, vaporised, atomised, and subsequently, ionised shown in Fig. 2.2. The processes of desolvation, melting and vaporisation inside the ICP require the high kinetic temperature exceeding the boiling points of analytes. Due to the high density of the high-energy particles inside the ICP, the reported kinetic temperature of the Ar-based ICP is ranging from 5000–6000 K at a typical gas flow rate,[53] and the temperature is higher than the boiling points of the most elements. For the excitation temperature, which is important for cutting chemical bonds and ionising atoms, ICP has the higher excitation temperature than the kinetic temperature. For the most of elements, especially metallic elements demonstrating the lower first ionisation potential compared to Ar, the ionisation efficiency is more than 50% calculated based on theoretical calculations using statistical mechanics (Fig. 2.3).[52] In consequence of the high ionisation efficiency for many elements, high-sensitivity and accurate analysis of elemental ratios with the reduced elemental fractionation can be achieved using ICP-MS. Another important feature of the high excitation temperature is hard ionisation with suppressed production of polyatomic ions, which can be interfering ions on trace isotopes.[54] A typical production rate of metal oxide ions is less than 1% for Th, and almost all other atoms are ionised in the form of Th^+.[55]

As a results of both the high kinetic temperature and excitation temperature, the

Ar-based ICP has a large ionisation capacity of complete ionisation for particles with the size of more than 1 μm within a few hundred microseconds,[56] resulting in generation of large ion currents with improved SBR. Especially for isotope analysis involved in the ^{238}U–^{230}Th dating method, the ion sources must have the kinetic temperature of higher than 5000 K, which is the boiling point for Th, and the high excitation temperature for reducing the production of interfering ions on $^{230}Th^{+}$ with a minor abundance. Then, the Ar-based ICP ion source is a primary option because of the high kinetic and excitation temperature, while the TIMS technique has a challenge with the low ionisation efficiency of Th due to the difficulty of evaporation, and the SIMS technique with the softer ionisation compared to ICP requires a great care taken for elemental fractionation and polyatomic interfering ions.

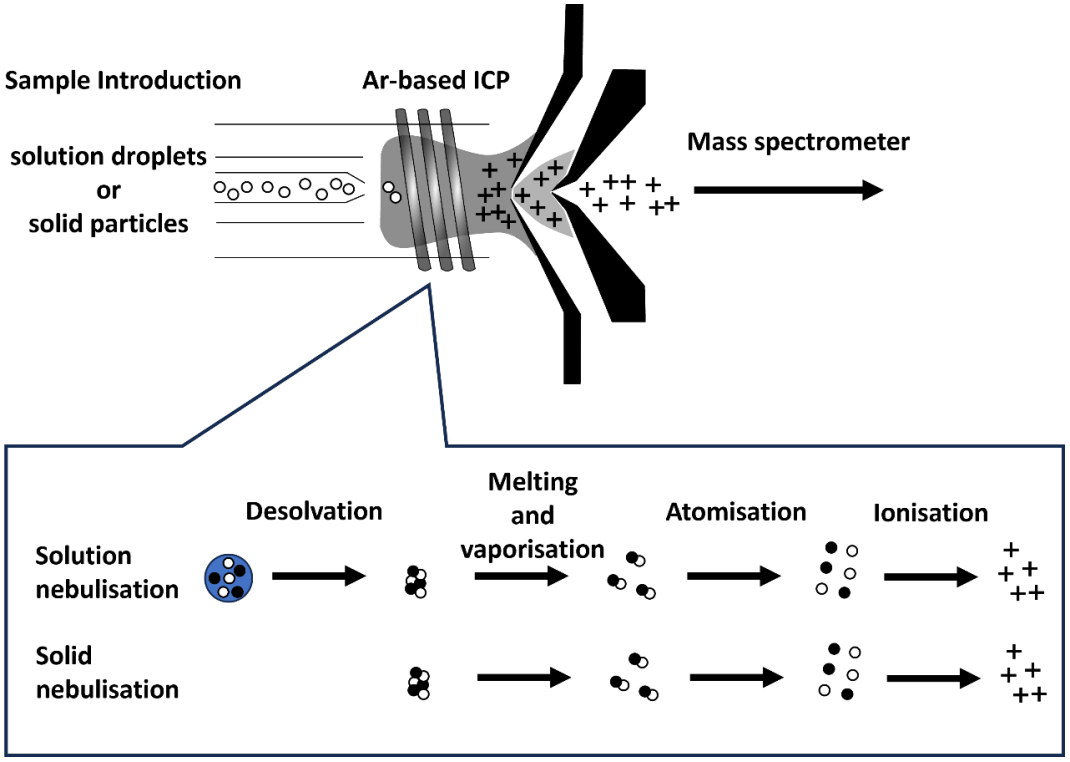

Figure 2.2 Schematic diagram of processes from sample introduction to ionisation in ICP, demonstrating the difference in two sample introduction methods of solution nebulisation and solid nebulisation.

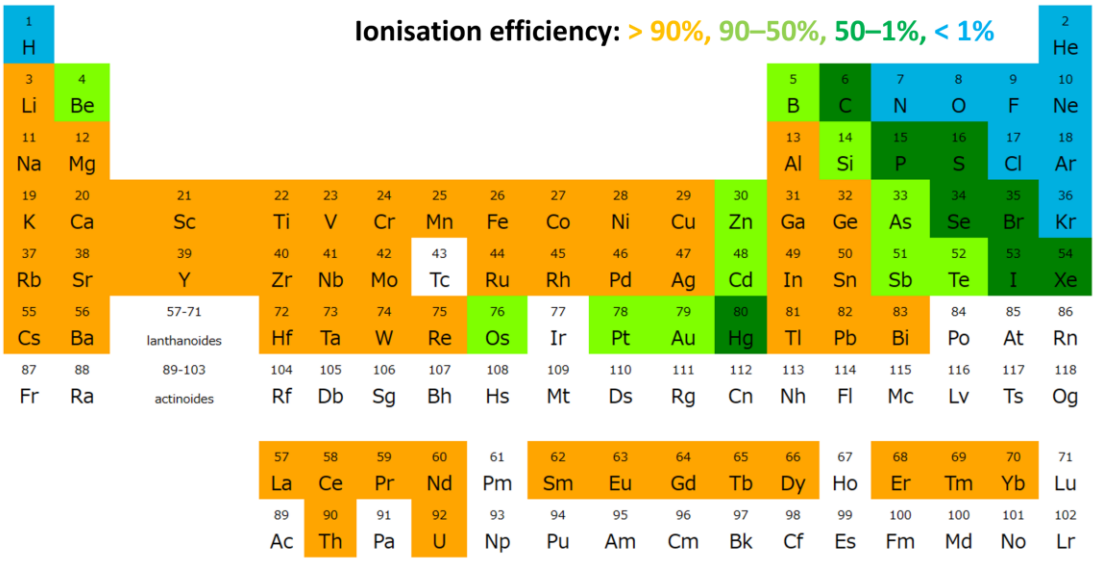

Figure 2.3 Ionisation efficiency for elements plotting on the periodic table modified after Niu and Houk.[51)]

2.3 *In situ* sampling method using laser ablation (LA)

Conventionally, high-sensitivity analysis for trace isotopes using ICP coupled with MS (ICP-MS) is based on sample introduction methods using solution nebulisation. Solution-based analysis using ICP-MS is important for precise isotope analysis owing to the stable signal profiles of analytes. Despite the importance, the solution-based analysis has major analytical problems. Firstly, the solution-based analysis is not suitable for *in-situ* measurements of each growth zoning inside a mineral grain with several tens of micrometres because of the lack in the spatial resolution of sample decomposition procedures. Moreover, especially for Th demonstrating poor solubility, the complicated protocols with a high experimental skill are required for the chemical decomposition of mineral and rock samples without residues containing Th.[57] This is a main cause of low-throughput analysis for the ^{238}U–^{230}Th dating method using ICP-MS. The long analysis time is also derived from the 500 to 1000-times dilution of sample aliquots for minimising non-spectral interferences (i.e., matrix effects). The resulting small ion currents require a long-time integration of isotope signals, and the low SBR make it difficult to conduct Th isotope analysis of a small sample volume, such as a single mineral grain. Moreover, during the solution introduction process, coarse droplets should be removed by using a spray chamber to obtain stable signal profiles, and the resulting transport efficiency to ICP is less than 10%.[58] When droplets are introduced into Ar-based ICP, the droplets are firstly desolvated, and subsequently, the desolvated salts are molten and vaporised, and finally, atomised and ionised (Fig. 2.2). The desolvation process causes the cooling of the gas temperature of ICP, and, the introduction of coarse droplets results in the low ionisation efficiency of refractory elements, such as Th. To acquire stable signal profiles, the removal of coarse droplets is necessary and the more than 90% of the sample volume is lost through the spray chamber, resulting in further low ion currents.

If solid materials are directly introduced into ICP, the high gas temperature is maintained under the dry plasma condition without the desolvating process (Fig. 2.2). The direct introduction of solid materials (i.e., solid nebulisation) without dilution and removal of coarse droplets also enhances the ion currents by more than a thousand times compared to solution nebulisation. This results in the high-throughput isotope analysis. For solid sample introduction coupled to ICP-MS, laser ablation is a foremost selection.[59]

During the LA process, laser is irradiated on a solid material, and the irradiated material is removed from the sample surface through mechanical breakage or melting, vaporising, and the subsequent condensation (Fig. 2.4).[60, 61] By the introduction of the resulting ejecta from the sample surfaces into the ICP-MS system, the direct sample introduction of solid materials is achieved and the elemental and isotopic analysis is conducted with the spatial resolution defined by the size of laser ablation pit.[59] Thus, the combination of the LA and ICP systems (LA-ICP-MS) can be the principal choice for a high-speed *in situ* ^{238}U–^{230}Th dating method (Fig. 2.5).

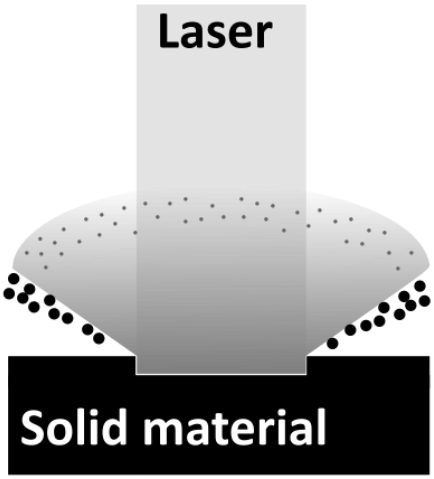

Figure 2.4 Schematic diagram of materials released from sample surfaces during laser ablation.

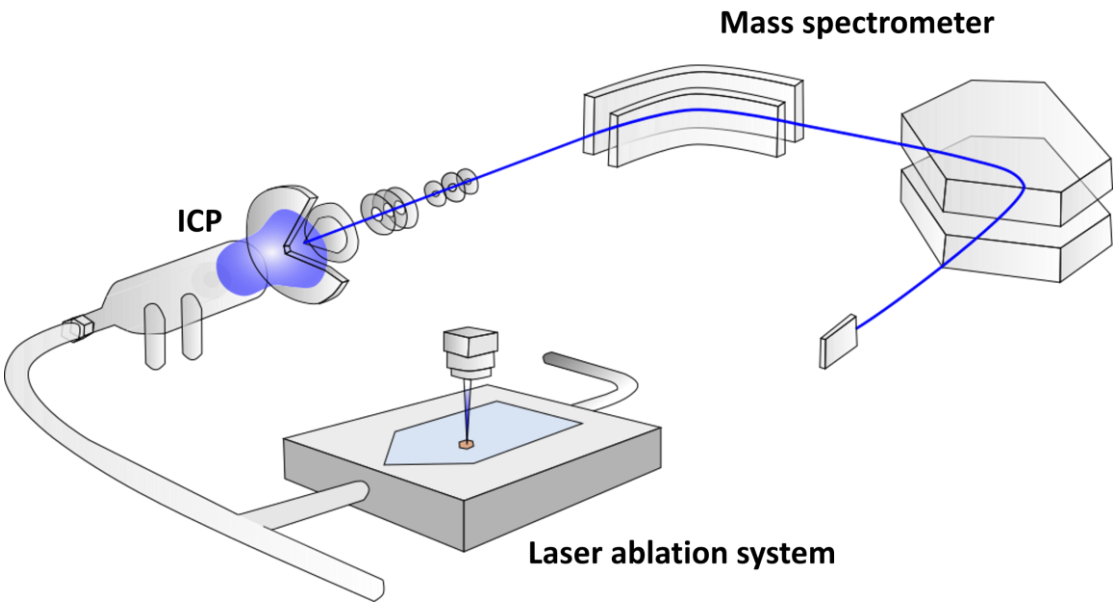

Figure 2.5 Schematic diagram of laser ablation inductively coupled plasma mass spectrometry (LA-ICP-MS) based on a sector-field-based mass spectrometer.

2.4 Analytical challenges

Despite the advantages of analytical methods using LA-ICP-MS, there are three analytical challenges with LA-ICP-MS applied to the ^{238}U–^{230}Th dating method; I. non-spectral interferences (i.e., matrix effect), especially derived from the LA process, II. mass spectrometric interferences due to the direct sample introduction without separation of matrix components, and III. selection of analysis areas for reliable age determinations using LA-ICP-MS. In my thesis, the three challenges are studied.

The first challenge is the matrix effect concerning LA-ICP-MS. The matrix effect is a critical challenge since the early ages of investigation on LA-ICP-MS.[59, 62] Generally, the released particles and gases made by laser ablation, or these ejecta actually transported into ICP have the deviated chemical compositions from the original compositions of samples (i.e., elemental fractionation),[63] and this is a main cause of the non-spectral interference depending on elements and sample matrices (i.e., matrix effect). Practically, the elemental fractionation involved in laser ablation is suppressed by utilising a short-pulse-width (i.e., femtosecond) ultraviolet laser with reduced thermal loading on sample surfaces to suppress the elemental fractionation because of the volatility of elements.[64, 65] The resulting particles generated by femtosecond laser ablation are mainly less than 100 μm,[66] and the improved transport efficiency of the fine particles is effective for reduction of the elemental fractionation. Despite the improvement of LA systems, remaining systematic deviations of elemental ratios, especially ratios of two elements having different volatility (e.g., Zn/Cu), can be a few tens of percents without calibration using matrix-matched references.[66] Despite the practical success based on the matrix-matched calibration, for further improvements in the data quality obtained by LA-ICP-MS, detailed understanding of laser ablation processes within a few microseconds after laser irradiation is desired. During my doctoral study, a new analytical protocol for nanoparticles generated by laser ablation is developed utilising an in-house micron-resolution femtosecond laser ablation system and high-time-resolution multiple-collector ICP-MS, and the behaviour of Th during laser ablation is investigated. Subsequently, in the section 3.2, the mechanism of elemental fractionation during laser ablation elucidated from the direct analysis of the LA-generated nanoparticles is discussed.

The second challenge is the mass spectrometric interference, especially on m/z

230, which deteriorate the accuracy of ^{238}U–^{230}Th ages. Thorium-230 contained in zircon is ca. 0.1–10 ng g^{-1}, and thus, even minor interference ions can be the cause of systematic errors for Th isotope analysis, resulting in erroneous age determinations. Despite the less contribution of interfering ions produced in the ICP compared to secondary ionisation, the significant contribution of zirconium-related polyatomic ions derived from sample matrices is reported, especially when analysing zircon samples.[67, 35] Among the zirconium-related polyatomic ions interfering with $^{230}Th^+$, the abundance of $^{90}Zr^{92}ZrO_3^+$, $^{91}Zr_2O_3^+$ is the highest, and the contribution of them can correspond to the concentration of several ng g^{-1}. Potential polyatomic interfering ions can be also originated from contamination, such as $^{182}W^{16}O_3^+$ emanating from sodium polytungstate used as a heavy liquid for separation of heavy mineral fractions (e.g., zircon). Another important interference is the signal tailing from $^{232}Th^+$ as well as the analysis made by SIMS because of the insufficient abundance sensitivity using sector-field-based mass spectrometry.[67, 35] In previous studies, the complicated correction based on the estimated contribution of the interferences to *m*/*z* 230 is applied for accurate age determinations. Faced with this challenge, a scheme for reducing the contribution of spectral interferences on *m*/*z* 230 using quadrupole-based MS equipped with a collision cell technique is newly developed, and the technique is applied to the high-spatial-resolution ^{238}U–^{230}Th dating method.[41] The detailed description is made in the section 3.3.

The third challenge is involved in imaging techniques, which are essential for selection of analysis spots inside mineral grains. Even if the accuracy of the isotope measurements is ensured, the age determinations can be erroneous when analysing mixed growth zones without observing internal structures of mineral samples. Conventionally, electron-microscopic techniques are used for observations of the internal textures of mineral samples, and cathodoluminescence (CL) is a commonly used for fast and routine mapping analysis prior to radioisotope dating of samples.[68] Despite the importance, the CL images reflect multiplicated factors including concentrations of specific elements, or radiation damages,[69] and the conversion of the CL images to elemental maps is difficult. Thus, the CL image can have less geochemical information compared to the actual elemental maps. As well, a recent study demonstrated that trace-element compositions determined with a sub-micron to micron spatial resolution reflecting the conditions of mineral formation can be useful for discrimination of the ^{238}U–^{230}Th isotope ratios

acquired from zircon potentially having different chronological information.[70] Thus, micron-scaled trace-element mapping is increasingly important. Owing to the high sensitivity of mass spectrometric techniques compared to other elemental imaging techniques, such as electron microscopic techniques, imaging mass spectrometry is a predominant option. Among the mass spectrometric techniques, LA-ICP-MS with both the high sampling rate and large ion capacity is a leading candidate for higher-speed imaging analysis of trace elements.[71] During my doctoral study, the newly developed femtosecond LA system with the focused laser spot size of ca. 2 μm was coupled to a sensitivity-enhanced quadrupole-based ICP-MS, and the mass spectrometric imaging technique was applied to the trace-element imaging analysis of zircon. The details are described in the section 3.4.

Chapter 3
Analytical challenges with LA-ICP-MS

工欲善其事必先利其器.

This is derived from a Chinese proverb stating that a craftsman must first sharpen his tools to do his job well. Dr. Typhoon Lee and his co-authors referenced this proverb to illustrate their philosophy aimed at improving their brilliant analytical techniques for the advances in isotope cosmochemistry.[72] To pave the way for novel studies in isotope geochronology, we must first solve the challenges in analytical chemistry.

3.1 Big lesson for better results

In Chapter 3, we discuss the causes of analytical errors found in LA-ICP-MS. In general, analytical errors of about 10 to 20% is typically acceptable for determining the abundance of trace elements in geochemistry. However, in chronological studies, both higher precision and accuracy of the measurements is desired. Errors of elemental and isotopic ratios (e.g., $^{14}C/^{12}C$, $^{87}Rb/^{88}Sr$, $^{187}Re/^{188}Os$, $^{206}Pb/^{238}U$, $^{208}Pb/^{232}Th$, and $^{230}Th/^{238}U$ etc.) directly correspond to errors in calculated radioisotope ages. Hence, small levels of analytical errors (i.e., even 1% deviation from the true values) can become problematic to understand the chronological sequences of geologic events in the Earth's history, and thus, great care must be given in the potential cause of analytical errors in the elemental analysis associated with LA-ICP-MS.

There are two main sources of analytical errors: the analytical methods based on mass spectrometry, and samples subsidized to geological studies. The analytical errors associated with the mass spectrometry can be divided into two categories: mass spectrometric interference and non-spectral interference (Fig. 3.1). Mass spectrometric interference is the increase of background counts for analytes by the contribution of interfering ions having a similar mass-to-charge ratio to the analytes. Non-spectral interference refers to a term for all other interferences except for mass spectrometric interference. A major factor in non-spectral interference is the difference of sensitivity depending on elements and isotopes for analytes, and the matrix compositions of samples. This is a main cause of the errors in radioisotope age determinations based on the analysis of multiple elements and isotopes. The resulting values suffered from both the mass spectrometric and non-spectral interferences deviate from the true values, as illustrating in Fig. 3.1.

Even if the isotope and elemental ratios obtained by mass spectrometry are accurate with careful consideration on interferences, they do not necessarily correspond accurate ages of geological events. When a geological sample is formed through multiple events, the obtained radioisotope age can be a mixed age value of the multiple events. A potential way to avoid this error is careful observations on internal heterogeneity within geological samples reflecting multiple steps of formation processes. Minerals crystallised in magma reservoirs grow through several stages, and after the eruption to the surface,

they may undergo alteration under the surface environment. These geological events can be recorded inside the internal textures of minerals. When isotope analysis is conducted for each zoning texture preserving chronological information of each event, separate radioisotope ages reflecting the timings of multiple stages can be acquired. Hence, imaging analysis prior to *in situ* age determinations is critical (Fig. 3.2). In the following sections, the analytical causes in the ^{238}U–^{230}Th dating method using LA-ICP-MS are investigated.

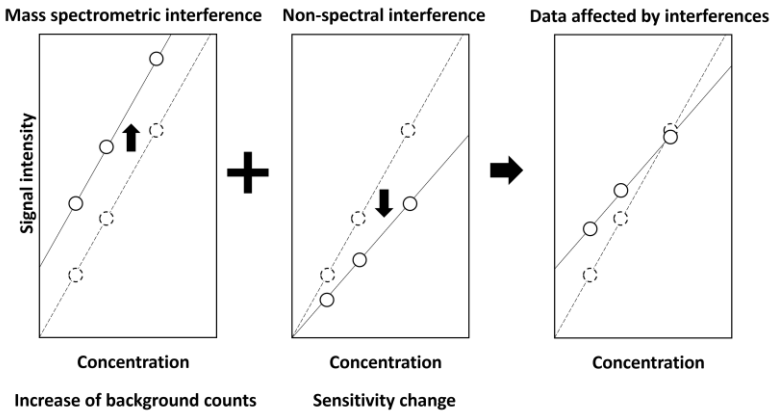

Figure 3.1 Schematic diagram of interferences causing analytical errors.

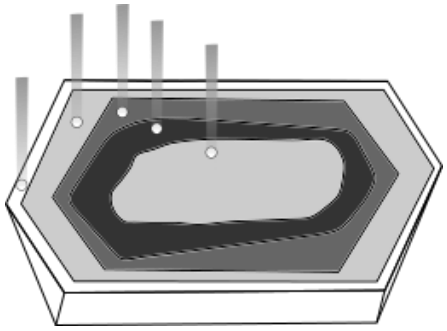

Figure 3.2 Schematic diagram of *in situ* age determinations with observations of zoning textures inside a mineral grain. The outer three zones with the euhedral shape coloured in white, grey, and dark grey demonstrate the areas crystallised during the recent series of igneous or metamorphic events, while inner two zones with the subhedral shape correspond to the inherited core formed during the earliest period of crystal formation. The size of analysis spots shown as the white circles must be smaller than the width of the zoning textures to derive reliable age data for multiple geological processes.

3.2 Non-spectral interference caused by laser ablation

In the section 3.2, the non-spectral interference (i.e., matrix effect) found in the laser ablation (LA) is discussed. To understand the cause of the non-spectral interference on Th, a new analytical protocol for the elemental ratio (Pb/Th) of "individual" sample particles generated by LA is developed. Based on the Pb and Th signal intensities obtained from Th-bearing materials (monazite), the mechanism of particle generation during LA causing the matrix effect is discussed. This is very important to understand the mechanism of the non-spectral interference found in LA-ICP-MS.

3.2.1 Background of non-spectral interference

Laser ablation involves complicated processes in the release of materials from sample surfaces within a short time duration on nano- to micro-second scales (Fig. 3.3).[61] During LA, solid materials are interacting with photon, and the photon energy is absorbed into solid materials. Subsequently, the materials are mechanically broken, or molten and vaporised. The time evolution of the complicated LA processes depends on multiple factors including laser properties and physicochemical properties of sample matrices. Especially, laser wavelength, laser pulse width, and transparency or band gap of sample matrices etc. can influence the contribution of ablation by nonlinear processes including multiphoton absorption.[65] The poor understanding of the complicated processes during LA is posing a challenge for the improvement in accuracy and precision of elemental and isotopic measurements using LA-ICP-MS.

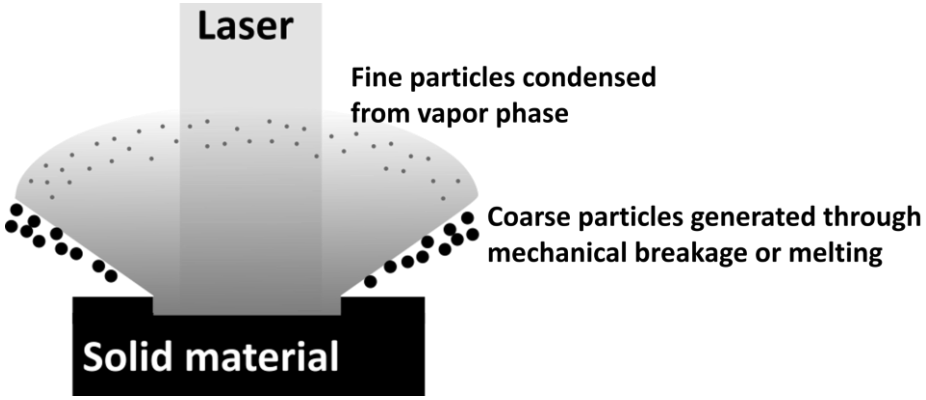

Figure 3.3 Schematic diagram for the generation and release processes of particles from a laser ablation pit.

If the materials in the laser-irradiated area are completely transported into ICP, the non-spectral interference originating from LA is not significant, regardless of variations in the LA processes depending on the different sample matrices and laser properties. Despite this, previous studies reported the difference in the transport efficiency of various elements from ablation pits to ICP, and this can deteriorate data quality of elemental analysis using LA-ICP-MS. This is also true in elemental and isotope ratio measurements, and, especially in the case of elemental ratio measurements for elements having different volatilities, the difference in mass fractions of vapor and solid particles can cause different transport efficiencies to the ICP ion source, resulting in changes of the measured elemental ratios (i.e., elemental fractionation).[62, 63] Furthermore, the differences in transport efficiency for each element also change depending on sample matrices. This is critical in elemental ratio analysis based on reference materials demonstrating a different physicochemical property from analysed samples (i.e., matrix-unmatched calibration). In geochronology, for instance, correction of the elemental fractionation is highly important since accurate measurements of diverse elemental and isotope ratios for various mineral species are required. Despite the demands, preparation of well-characterised calibration standard materials (i.e., age references), whose elemental or isotope ratios involved in a specific decay system are accurately and precisely determined, are limited to several mineral species, such as zircon, or apatite. Hence, the matrix-unmatched calibration of elemental and isotope ratios, such as $^{206}Pb/^{238}U$, $^{207}Pb/^{206}Pb$, and $^{208}Pb/^{232}Th$ based on well-characterised zircon references is desired. Nonetheless, if zircon references are used for the calibration of Pb/U in the case of U–Pb dating of carbonates with different physicochemical properties from zircon (e.g., melting point and band gap), the resulting U–Pb age can be erroneous.

Figure 3.4 illustrates the measured U–Pb isotope data of the WC-1 calcite with zircon-based calibration obtained by LA-ICP-MS. The resulting U–Pb age is 311.9 ± 7.5 Ma, and this is significantly older than the reference U–Pb age of 254.4 ± 6.4 Ma.[73] The elemental fractionation for Pb/U values is about 20%. The large magnitude of the elemental fractionation can be attributed high volatility of Pb and refractory feature of U. To obtain reliable Pb/U values from solid samples, at present, analysis of matrix-matched reference materials of known Pb/U values are practically important.

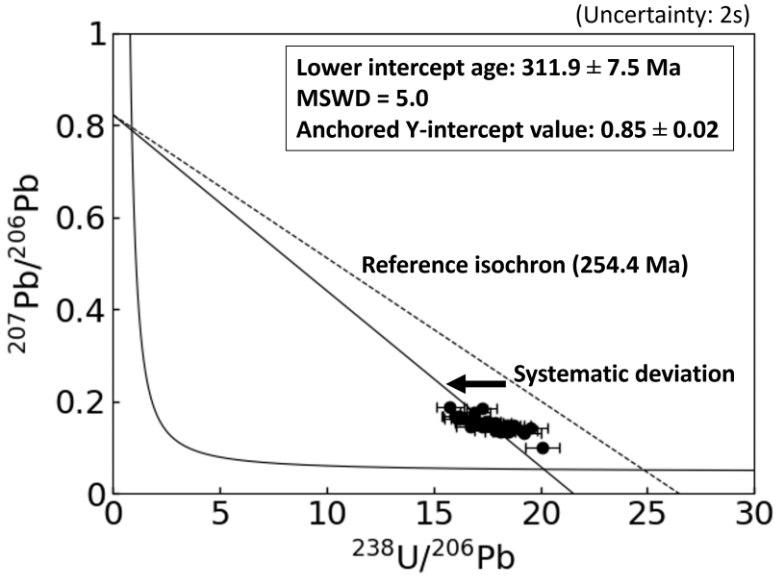

Figure 3.4 The U–Pb isotope ratios of the WC-1 calcite based on the matrix-unmatched calibration for Pb/U using zircon plotting on the Tera-Wasserburg concordia diagram. The resulting age deviates from the reference value of 254.4 Ma. The dashed line indicates the reference isochron of 254.4 Ma, and the isochron of the data points deviates from the reference isochron.

One of the major sources of the elemental fractionation found in LA is thermal loading on laser-irradiated areas and the surrounding areas. Due to the thermal load onto the ablation spots, elements with low boiling points selectively evaporate from laser-irradiated areas and the surrounding areas while refractory elements are incompletely vaporised.[74] This results in the systematic deviation of the measured compositions of the ejecta from the original compositions of materials. As well, the other main source of elemental fractionation is the size-dependent chemical compositions of coarser particles being enriched in refractory elements. The low transport efficiency of the refractory-element-enriched coarse particles are also a cause of the elemental fractionation.[63] The previous study reported the presence of size-dependent chemical compositions of laser-induced sample particles. They also indicated that the particles with the smaller size than 125 nm had a chemical composition depleted in refractory elements, such as Th shown in Fig. 3.5. The redeposition of the coarse particles enriched in refractory elements during the transportation into ICP are attributed to the elemental fractionation.[63] The

introduction of the larger-sized particles into ICP is also problematic because of the incomplete vaporisation and ionisation of the coarse particles in ICP, resulting in the elemental fractionation.[75)]

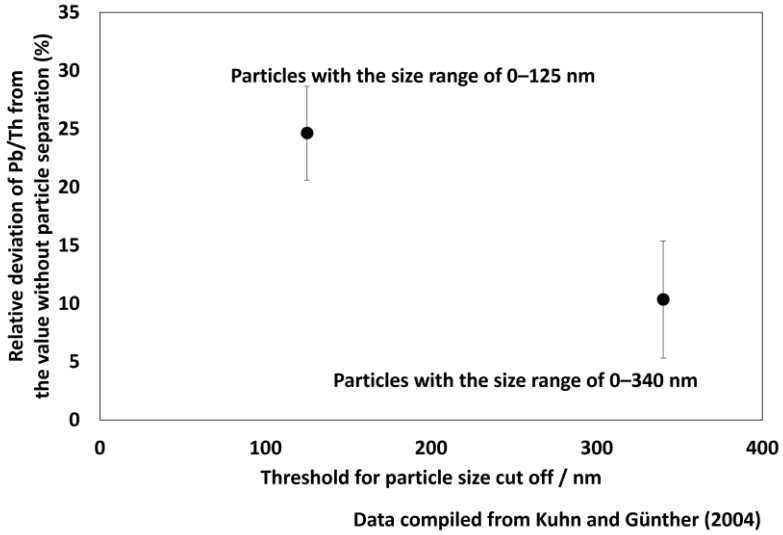

Figure 3.5 Elemental fractionation observed in the analysis using LA-ICP-MS due to size-dependent chemical compositions of LA-generated particles. The threshold for particle size cut off is plotted on the x-axis, and the relative deviation of the Pb/Th values from Pb/Th without the size separation. The plotted data points are compiled from the published article reported by Kuhn and Günther.[62)]

The release of coarse particles (i.e., > 1μm) from ablation pits is enhanced by the increased heat load during LA. Pioneering research suggests a potential mechanism of coarse-particle generation for condensation or aggregation occurring during cooling within the LA-induced plume.[60)] Despite the importance of the study, the direct observation of the LA processes with a high-speed camera elucidated that particles are emitted from the laser ablation pit at a low angle without passing through the plume.[61)] This observation contradicts to the hypothesis of condensational generation of particles within the LA-induced plume, in which most particles are released vertically. The two LA models are summarised in Fig 3.3. In either case, the generation of coarse particles can cause significant elemental fractionation owing to the low transport efficiency of

coarse particles during the transportation to ICP due to the redeposition of the particles, and incomplete ionisation of large particles.

To supress the production of coarse particles, helium atmospheric gas is practically utilised instead of argon gas. Helium gas has the higher thermal conductivity than argon gas, and the generation of coarse particles within the LA-induced plumes is practically supressed through fast cooling based on the condensation-growth model.[60] The suppressed production of the large particles enhances the transport and ionisation efficiency (Fig. 3.6), and this results in better precision and accuracy of measurements using LA-ICP-MS.

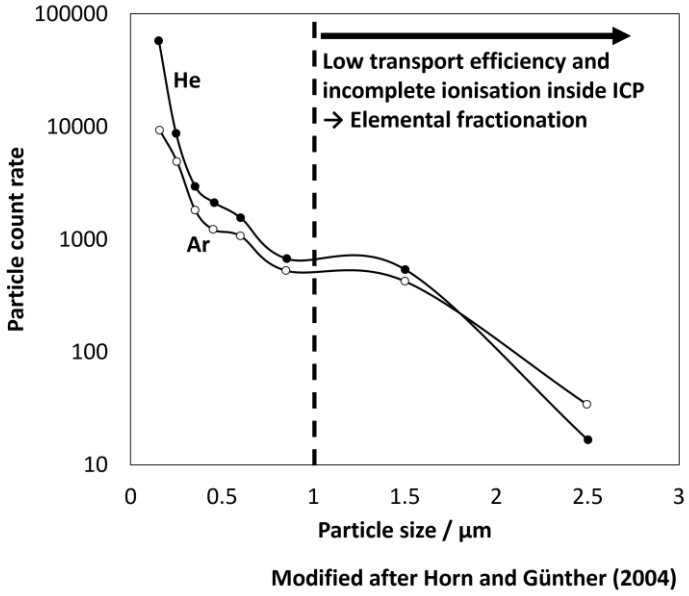

Figure 3.6 The size distribution of particles generated by nanosecond laser ablation under Ar and He atmospheric gases. Coarse particles produced through nanosecond laser ablation can cause the elemental fractionation, and the finer particles are produced under He compared to Ar, potentially resulting in the reduced elemental fractionation. The graph is modified after Horn and Günther.[59]

Another important approach to suppress the elemental fractionation is to use the femtosecond laser ablation (fsLA) with the reduced thermal loading on the ablated areas. The fsLA processes depends upon multi-photon excitation rather than thermal processes in contrast to conventional nanosecond LA systems, resulting in the efficient absorption of femtosecond laser energy within the ablated areas prior to the diffusion of heat to the surrounding areas, and the elemental fractionation reflecting differences of volatility induced by the heat load can be reduced.[65] Moreover, the production of coarse particles is suppressed by fsLA, and this improves the transport efficiency of the generated particles into ICP, and reduces the elemental fractionation. Despite the suppression of the thermal loading using the He atmospheric gas and fsLA, however, significant elemental fractionation with the relative deviation of a several tens of percent was still reported from the analysis of ratios for elements having different volatility, such as Pb/Cu and Zn/Cu (Fig. 3.7).[66] Even when using fsLA, both the experimental results and theoretical calculations suggest that the fsLA process involves the evaporation of the outermost surface and melting of the sub-surface layers within the ablated regions.[76] This can be another cause for elemental fractionation because of the different volatility. Figure 3.7 also demonstrates the significant elemental fractionation between Zn and Pb, although both the elements are volatile. Thus, there remains a possibility for another cause of the elemental fractionation in addition to the volatility.

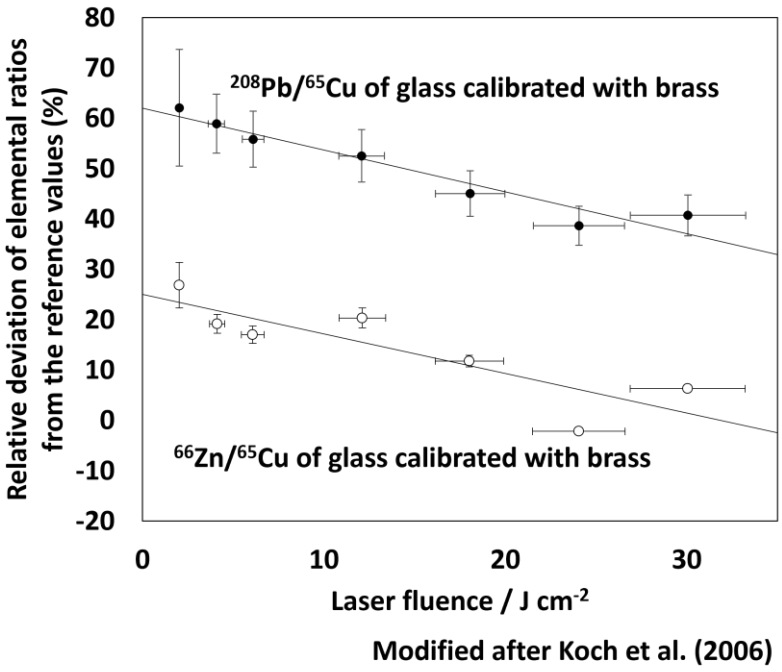

Figure 3.7 The elemental fractionation observed in $^{66}Zn/^{65}Cu$ and $^{208}Pb/^{65}Cu$ of NIST SRM 610 owing to the matrix-unmatched calibration based on brass analysed using fsLA-ICP-MS. The graph is modified after Koch and the co-authors.[65)]

In this study, to elucidate the fundamental aspects of the elemental fractionation during the fsLA as particle generation processes, analysis of elemental ratios for individual fsLA-generated particles was conducted while previous studies depend on bulk analysis of collected particles. For the elemental ratio analysis of individual fsLA-generated particles, direct online analysis coupled with a fsLA system is desired for high-throughput analysis of all fsLA-generated particles released from an ablation pit, and an ICP-MS system is a primary option. For single-particle analysis using ICP-MS, the short dwell time of isotope data acquisition is required to resolve each signal event derived from particle introduction into ICP. The time duration of isotope signals derived from the particle events is about several hundreds of microseconds, and the time resolution of the detection system better than one hundred microseconds is desired.[77)] The direct analysis of LA-generated particles using a single-collector sector-field ICP-MS was previously reported by Donard et al.,[78)] and the size distributions of particles generated by LA on cupper were estimated from the obtained signal profiles of ^{65}Cu using a mathematical

treatment. Despite the importance of the pioneering research, the signal peaks of detected particles were partly overlapped due to a high introduction rate of particles generated by LA, and this can result in erroneous measurements. Thus, for the measurements of individual particles generated by fsLA, the reduction of the number of introduced particles into ICP is necessary. Faced with this challenge, in this study, ablated volumes were minimised by developing an in-house micron-resolution femtosecond laser ablation system (Tandem; Fab Instruments, Tokyo, Japan). The micron-resolution femtosecond laser ablation system is composed of femtosecond laser with the wavelength of 260 nm, the pulse width of 290 fs and the beam diameter of 4.2 mm before focusing, and an objective lens with the focal length of 10 mm. By using the ten-times shorter-focal-length objective lens compared to conventional LA systems, the laser spot diameter is minimised to ca. 2 μm. Compared to the pioneering study for the single-particle ICP-MS analysis of LA-generated particles with the laser spot size of 20 μm, the ablated volumes can be reduced by two to three orders of magnitude, resulting in the decreased introduction rate of LA-generated particles into ICP.

The single-collector ICP-MS used in the previous study is also problematic in terms of elemental- and isotopic-ratio analysis. With the single-collector system, mass scanning is intrinsically necessary for monitoring multiple isotopes, and for isotope signals of particles with the short time duration, the accurate analysis of elemental and isotopic ratios is practically impossible. To overcome this, multiple-collector ICP-MS (MC-ICP-MS) equipped with six high-time-resolution (HTR) ion counters is utilised for multiple-isotope analysis of individual particles (HTR-MC-ICP-MS).[79, 80)]

With the combination of the micron-resolution fsLA system and the HTR-MC-ICP-MS system, the ratios of elements demonstrating the difference in the volatilities were acquired from individual particles generated by fsLA. The elements measured in this study are Th as a representative of refractory elements and Pb as a volatile element. Moreover, $^{208}Pb/^{232}Th$ is important to derive chronological information of geological samples based on the ^{232}Th–^{208}Pb isotope systematics, especially useful for age determinations of young samples without achieving a radioactive equilibrium.[26)] Analysed materials in this study were the age references of monazite. Monazite is phosphate mineral containing both rare-earth-element and Th with the concentration of up to several percent. The monazite is commonly used for the Th–Pb dating method. Well-

characterised monazite references have known bulk values of $^{208}Pb/^{232}Th$ calculated from the ages of the references, and thus, monazite is an appropriate material for studying elemental fractionation during fsLA based on the determination of $^{208}Pb/^{232}Th$ values for individual particles generated from fsLA on monazite references.

3.2.2 Experimental

3.2.2.1 Instrumentation

The laser ablation systems utilised in this study were the in-house micron-resolution fsLA system. The fsLA system is made of a Yb: KGW laser medium with the laser wavelength of 260 nm and the pulse width of 290 fs. Since the number of particles released from ablated areas decreases with the reduction of sampling volume, one-shot laser ablation with the laser spot size of 2 μm was conducted in this study. The optical images of laser ablation pits are shown in Fig. 3.8. To suppress the particle introduction rate, a signal smoothing device was inserted in the way of the transportation tube.[81] Helium or argon was used for the atmospheric gas inside the sample chamber of the fsLA system to compare the contribution of different thermal conductivity to particle generation processes, and the gas flow rate was 0.8 L min^{-1} for He and 1.0 L min^{-1} for Ar. To ensure consistent plasma gas conditions in both the experiments when using He or Ar atmospheric gas, the make-up gas of Ar or He was added outside the sample chamber, and the resulting total carrier gas was composed of He and Ar with the flow rate of 0.8 L min^{-1}, and 1.0 L min^{-1}, respectively.

In this study, HTR-MC-ICP-MS was utilised for a detection system of ablated particles. Since the isotopic signals derived from introduction one nanoparticle into ICP-MS have a time duration of a few hundred microseconds, the dwell time of the signal output was set at 20 μs. For isotopic and elemental analysis of LA-generated particles derived from monazite samples, a multiple-collector ICP-MS (Nu plasma II, Nu instruments, U.K.) equipped with high-time-resolution ion counters (HTR-MC-ICP-MS)[79, 80] is utilised. For the acquisition of isotopic compositions of ablated particles, the isotopic signals of $^{232}Th^+$, $^{208}Pb^+$, $^{206}Pb^+$, and $^{204}Pb^+$ were detected. $^{232}Th^+$ and $^{208}Pb^+$ were measured by Daly detectors (D5 for ^{232}Th and D2 for ^{208}Pb), and $^{206}Pb^+$ and $^{204}Pb^+$ were measured with the secondary electron multipliers of IC3, and IC4. The signal count rates

were corrected for counting loss due to the dead time of the detectors based on the non-paralysed model. The applied dead times were 20.0 ns, 10.8 ns, 14.7 ns, and 15.4 ns for D5, D2, IC3, and IC4, respectively. The schematic diagram of the detection array is demonstrated in Fig. 3.9. The experimental conditions of the fsLA and HTR-MS systems are summarised in Table 3.1.

The analysed monazites in this study are 16-F-6 monazite, Namaqualand monazite, and 44069 monazite. These monazites are common references used for high-spatial-resolution U–Pb and Th–Pb dating methods based on LA-ICP-MS, secondary ionisation mass spectrometry and electron probe microanalysis (EPMA). The 16-F-6 monazite contains Th with the concentration of ca. 24000 μg g^{-1}, and the U–Pb age of 2842.9 ± 0.3 Ma was determined from isotope dilution-thermal ionisation mass spectrometry (ID-TIMS).[82] The 16-F-6 monazite was analysed for elucidation of particle generation processes based on the comparison of the LA-generated particles under the He and Ar atmospheric gases.

The other two monazites were measured for the evaluation of analytical accuracy for calibrated $^{208}Pb/^{232}Th$ values based on the analysis results of the 16-F-6 monazite as a primary reference. The calibration factor of $^{208}Pb/^{232}Th$ was reckoned from the normalisation of the measured $^{208}Pb/^{232}Th$ for the 16-F-6 monazite being the reference value of 0.15102 calculated from the reported U–Pb age of 2842.9 Ma and the decay constant of ^{232}Th (4.9475×10^{-11} yr^{-1})[83] under the assumption of the concordance for U–Pb and Th–Pb isotope systems. The 44069 monazite has the Th concentration ranging from 10000 to 50000 μg g^{-1}, and the reported U–Pb age value of 424.9 ± 0.4 Ma measured with ID-TIMS.[84] The Namaqualand monazite has the relatively higher Th content of ca. 80000 μg g^{-1} compared to other two monazites, and the reported U–Pb age is ca. 1033 Ma based on isotope analysis using sensitive high resolution ion microprobe.[85] The Namaqualand monazite is commonly used for a secondary reference of the chemical Th-U-total Pb isochron method using EPMA, and the resulting reported age in a previous study was 1020 ± 41 Ma.[86] The age calculations were conducted using the equation (1.9) under the assumption of both the reference monazites containing negligible levels of non-radiogenic Pb considering from the good concordance of $^{238}U–^{206}Pb$ and $^{235}U–^{207}Pb$ systems.

Table. 3.1 Instrumentation and operational settings for the fsLA and HTR-MC-ICP-MS systems

(a) ICP-MS	
MC-ICP -MS instrument	Nu plasma II HTR-MC-ICP-MS (Nu Instruments, U.K.)
Sample introduction	Laser ablation
RF power	1300 W
Coolant gas flow	15.0 L min^{-1}
Auxiliary gas	0.8 L min^{-1}
Detection system	Mixed Faraday-multiple ion counting array
Monitored mass-to-charge ratio	204, 206, 208, and 232 Da
Detectors	Two Daly detectors (D), and two full size multipliers (IC) D2 for ^{208}Pb, IC3 for ^{206}Pb, IC4 for ^{204}(Hg + Pb), and D5 for ^{232}Th
IC dead time / ns	IC2 (Daly) 10.8 ns, IC3 (EM) 14.7 ns, IC4 (EM) 15.4 ns, IC5 (Daly) 20 ns
Integration time	20 μs
Oxide production rate (ThO^+/Th^+)	0.5%

(b) Laser Ablation	
Laser ablation system	Tandem (Fab Instruments, Tokyo, Japan)
Laser medium	Yb:KGW
Laser wavelength	260 nm (4th Harmonic Generation)
Pulse width	290 fs
Fluence	ca. 4 J cm^{-2}
Repetition rate	1,000 Hz
He gas flow	0.8 L min^{-1}
Ar gas flow	1.0 L min^{-1}
Spot diameter	ca. 2 μm
The number of laser shots	1 shot

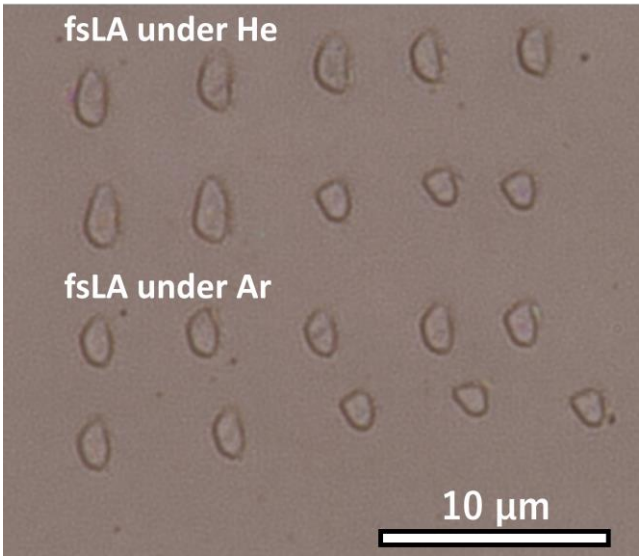

Figure 3.8 Optical microscopic image of the ablation pit on the 16-F-6 monazite using the micron-resolution fsLA system. The ten analysis spots on the upper half and the lower half were made by fsLA under the He and Ar atmospheric gases, respectively.

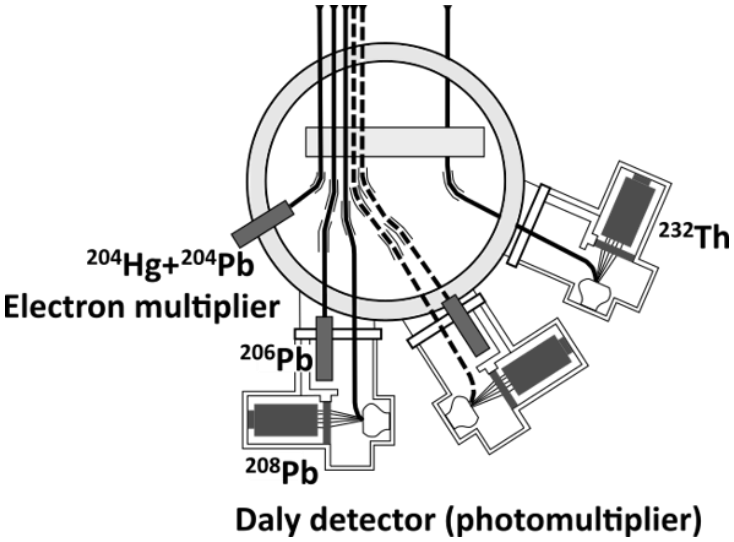

Figure 3.9 Schematic diagram of the multiple-collection array used in this study. Two Daly detectors are utilised for monitoring the signal of ^{232}Th and ^{208}Pb, and two ion counters using electron multipliers are used for measuring the signal of ^{206}Pb, and ^{204}Pb+^{204}Hg.

3.2.2.2 Scheme for data reduction of time-resolved isotope signals

The discrimination of transient isotope signals derived from particles was conducted for the time-resolved isotope signal profiles obtained from single-shot fsLA. The primary peak detection was made for each time slice outputted every 20 μs. The signal intensities of each time slice for ^{208}Pb and ^{232}Th are combined. Subsequently, time slices where the summation of the signal intensities exceeds a threshold calculated from the gas-blank signal profiles and is larger than that of adjacent time slices are regarded as potential peaks derived from particle introduction event. The different thresholds are set at 6 counts and 8 counts for fsLA under the He and Ar atmospheric gas, respectively, as the frequency of transient signals with the signal counts of more than the thresholds during thirty-second gas blank signal profiles is less than a single time. Then, to reject overlapped particle-derived signals and mistakenly detected peaks of fluctuated signals from a single-particle introduction event, the peaks are excluded when there is another signal greater than the peak value within the signal width, which is set as the full width of one two-hundredth of the peak intensity values. Finally, the signal counts for remaining particle signals after the discrimination scheme above are calculated by the summation of the range between the time slices just including the peak width.

The calculation scheme of particle sizes (diameter) is described in the following equations of (3.1) and (3.2) under the assumption of LA-generated particles containing a constant original matrix composition of monazite.

$$V = \frac{I_{\mathrm{Th}}}{f} \times \frac{m_{\mathrm{Th}}}{N_{\mathrm{A}} C_{\mathrm{Th}} \rho} \tag{3.1}$$

$$d = \sqrt[3]{\frac{3V}{4\pi}} \times 2 \tag{3.2}$$

where V: reduced volume of a single particle, I_{Th}: Signal counts of ^{232}Th for a single particle, f: ion transmission of ICP-MS, m_{Th}: molar mass of Th (232.0385 g mol^{-1}), N_A: Avogadro constant (6.02×10^{23} mol^{-1}), C_{Th}: thorium concentration (16-F-6 monazite; 24000 μg g^{-1}), ρ: density of monazite (ca. 5 g cm^{-3}), and d: reduced diameter.

The ion transmission of ICP-MS (f) was approximated by the useful yield of the LA-HTR-MC-ICP-MS system determined from the analysis of NIST SRM 610 by LA-HTR-MC-ICP-MS using the He atmospheric gas and Ar make-up gas. The useful yield

of ^{232}Th was calculated from the ratio of the detected number of ^{232}Th and the number of ^{232}Th atoms contained in ablated volumes. The loss of particles can be supressed by using femtosecond laser and He atmospheric gas, and thus, the useful yield is good approximation of the ion transmission. The actual value of the useful yield was 0.065% calculated from the signal counts of 7.05×10^6 for ^{232}Th, the ablated volume of 50×50×1.5 μm^3, the Th concentration of NIST SRM 610 as 457.2 $\mu g\ g^{-1}$,[87] and the density of 2.43 g cm^{-3} for NIST SRM 610.[88] For the case of the Ar atmospheric gas and the He make-up gas, the same useful yield was applied to the ion transmission because of the same plasma gas conditions as the case of the He atmospheric gas and the Ar make-up gas resulting in the same ion transmission.

3.2.3 Results and discussion

3.2.3.1 Multiple isotope signal profiles of single-shot laser ablation with high-time-resolution analysis

The signal profiles of ^{232}Th, ^{208}Pb, ^{206}Pb, ^{204}Pb after single-shot fsLA on the 16-F-6 monazite under the He atmospheric gas are shown in Fig. 3.10(a). Each spiking signal in Fig 3.10(a) corresponds to isotope signals derived from each particle introduction event. The enlarged time-scale version of the time-resolved signals is shown in Fig. 3.10(b). Figure 3.10(b) demonstrates that the separate analysis of individual particles was made without overlapped signals, and Pb-bearing signals and Th signals without Pb are observed from the time-resolved multiple-isotope signals.

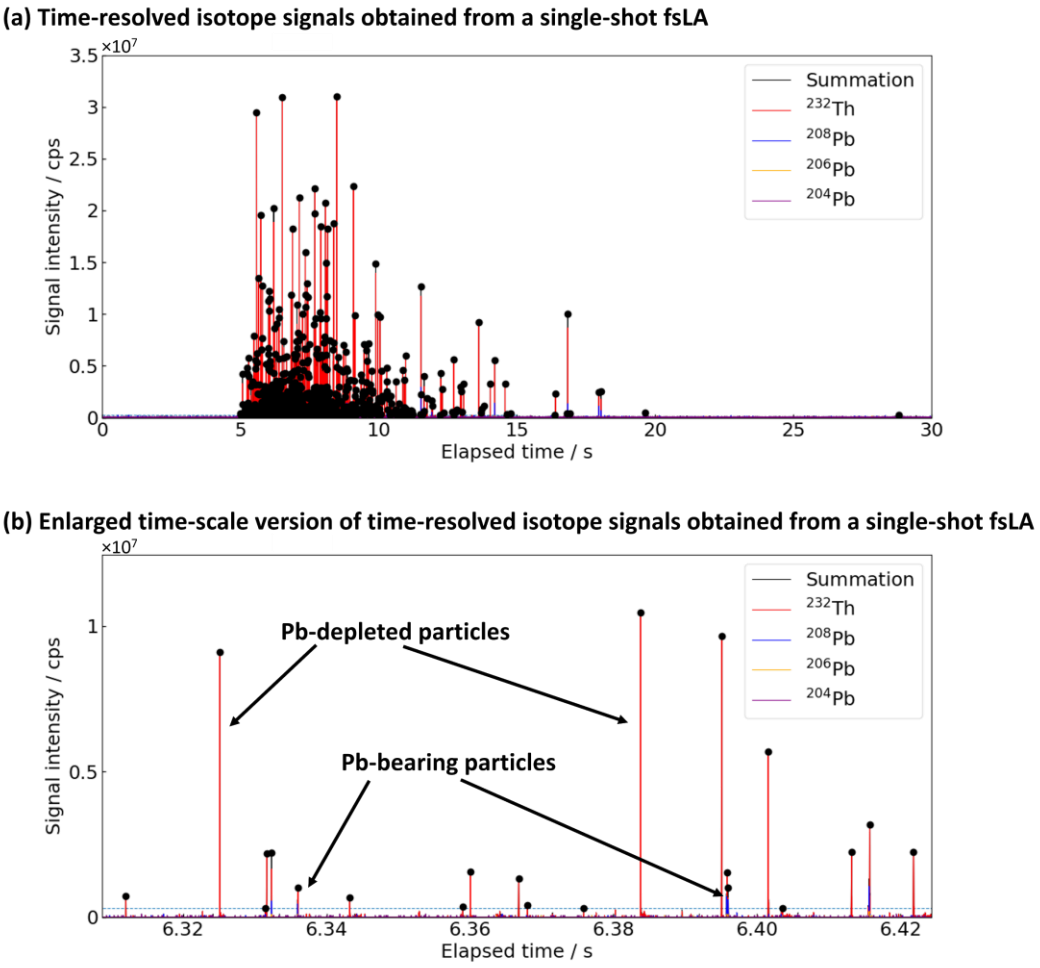

Figure 3.10 Time-resolve multiple-isotope signal profiles of a single-shot fsLA on the 16-F-6 monazite monitoring by using the HTR-MC-ICP-MS system. (a) The whole signal profiles are shown. (b) The enlarged time-scale version of the signal profiles is demonstrated.

Figure 3.11 demonstrates the signal counts of ^{208}Pb and ^{232}Th for each particle detected from the ten-spot analyses of the 16-F-6 monazite conducted by fsLA under the He and Ar atmospheric gases. The signal counts of ^{232}Th are plotted on the X-axis and the signal counts of ^{208}Pb are plotted on the Y-axis. The fsLA-generated particles have two decoupled $^{208}Pb/^{232}Th$ values; Pb-depleted particles and Pb-bearing particles as well as found in the time-resolved signal profile. In this study, the threshold for Pb-depleted and Pb-bearing particles is set as being less or greater than one-tenth of the original $^{208}Pb/^{232}Th$ values calculated from the reported U–Pb ages of the monazite references. The two decoupled components indicate that Pb-depleted and Pb-bearing particles are generated through the different processes during LA reflecting the difference in the physicochemical properties, especially volatility, of Th and Pb. For Th, the nearest-neighbour atoms are oxygen within the crystal lattice of monazite, and this is also applied to Pb based on the recent study of X-ray photoelectron spectroscopy, suggesting that the chemical state of radiogenic Pb inside monazite is Pb^{2+} substituting the site of lanthanide cations.[89] Hence, the volatility of Th and Pb within monazite should be discussed based on the oxide states of ThO_2 and PbO. The melting point and boiling point of PbO are 890 ℃ and 1480 ℃, respectively, while those of ThO_2 are 3400 ℃ and 4400 ℃. The notable thing is that the boiling point of PbO is less than the melting point of ThO_2, and the case is also applied to the monazite matrix having the melting temperature of 1900–2100 ℃.[90] The disparity in volatility indicates that Th can remain in the liquid or solid phase while Pb evaporates.

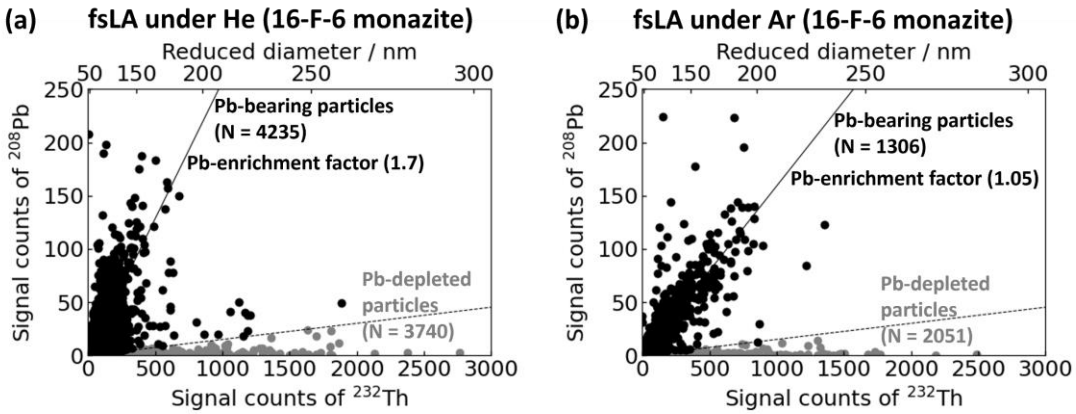

Figure 3.11 Signal counts of ^{232}Th and ^{208}Pb of each signal derived from particle introduction. Detected particles by HTR-MC-ICP-MS are represented in (a) and (b) corresponding to the atmospheric gas of He and Ar, respectively. The dashed lines represent the set threshold for Pb-bearing and Pb-depleted particles. The solid straight lines demonstrate the Pb-enrichment factors of the Pb-bearing particles.

Figure 3.12 demonstrates the size distribution of Pb-bearing and Pb-depleted particles calculated from the signal counts of ^{232}Th for each particle signal event. The reduced diameters of the detected particles are less than 300 nm, and the number of particles decreases as the size becomes smaller. For Pb-bearing particles, when using He atmospheric gas, the larger number of finer particles than 150 nm is detected, and the reduced number of larger-sized particles is detected compared to the Ar atmospheric gas. The obtained results that coarse particles are more likely to be formed when LA performed under Ar atmosphere are consistent with the previous study.[60] Based on the condensation model within the LA-induced plume, coarser particles are generated via condensation and agglomeration within the long-lived enlarged plume made by LA under Ar with the higher viscosity and lower thermal conductivity compared to He. However, the volume of the LA-induced plume under Ar must be smaller than under He due the higher viscosity and lower thermal conductivity causing the suppression of diffusion for gaseous phases and heat. In spite of the contradiction, the generation of coarser particles under Ar than He is attributable to the higher density of evaporated phases within the smaller plume, resulting in the higher number concentration of atoms surrounding the condensation nuclei.

In Fig. 3.11(a) and (b), the slopes of solid lines indicate the Pb-enrichment factors

of the Pb-bearing particles calculated from the ratios of the $^{208}Pb/^{232}Th$ values reckoned by summation for the signal counts of all Pb-bearing particles, and the reference $^{208}Pb/^{232}Th$ value of 0.15102. The lower Pb-enrichment factor of the case in fsLA under Ar compared to He is also attributable to the higher proportion of evaporated Th within the higher-temperature plume with the smaller size under Ar than He.

For the Pb-depleted particles, the size distributions of both the He and Ar atmospheric gases are similar. The similarity strongly indicates that the generation of the Pb-depleted particles does not involve in the condensational process from vapor, which is a cause for the difference in particle sizes depending on the atmospheric gases. In addition, the fractional condensation from vapor phases can produce particles with the intermediate composition of the Pb-depleted and Pb-bearing particles, and the clear decoupling of the Pb/Th compositions suggests the absence of the fractional condensation process. This fractional condensation process can also create a dependency of Pb/Th on the particle size. When particles are generated via the fractional condensation from vapor phases, the Pb-depleted particles condense early. Then, the Pb-depleted particles act as growth nuclei, and the Pb-bearing particles formed later tend to be larger. In spite of the expected tendency for the size distribution, the size range of the Pb-bearing and Pb-depleted particles is similar, and the number fraction of coarser particles (>200 nm) for the Pb-depleted particles is larger than that for the Pb-bearing particles. This strongly suggests that the Pb-depleted particles are not produced through the fractional condensation process.

Hence, the Pb-depleted particles are directly released matters from the ablation pit. The released matters can originate from the molten sub-surface layer where the temperature exceeds the melting point of monazite ranging from 1900℃ to 2100℃. Since the melting point of monazite is higher than the boiling point of Pb, the almost complete evaporation of Pb can be achieved within the molten layer, resulting in the ejecta from the molten layer having the Pb-depleted compositions. The schematic diagram of the particle generation process through fsLA is summarised in Fig 3.13. The proportion of the molten and vaporised areas during laser ablation can change depending on the melting and boiling points of matrix components, and this results in complex matrix effects during LA, especially in the analysis of refractory elements.

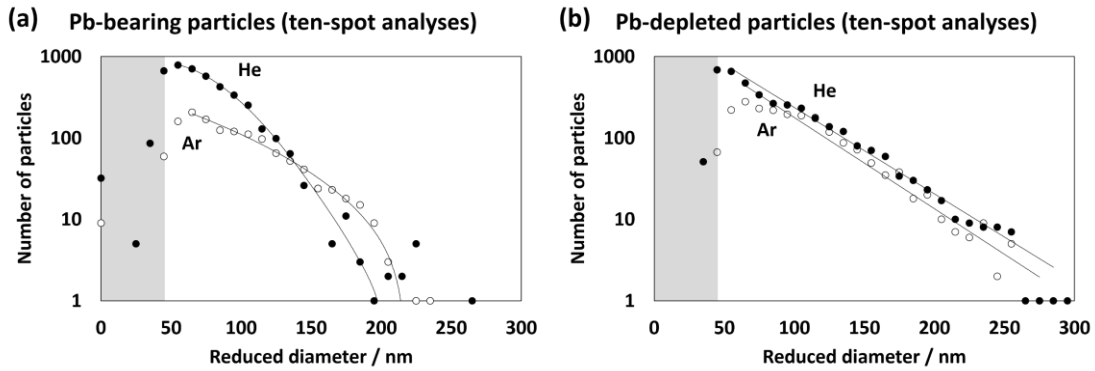

Figure 3.12 Reduced particle-size distribution calculated from the signal counts of ^{232}Th for (a) Pb-bearing particles and (b) Pb-depleted particles. Owing to the threshold for particle identification, the grey-coloured areas can be erroneous results.

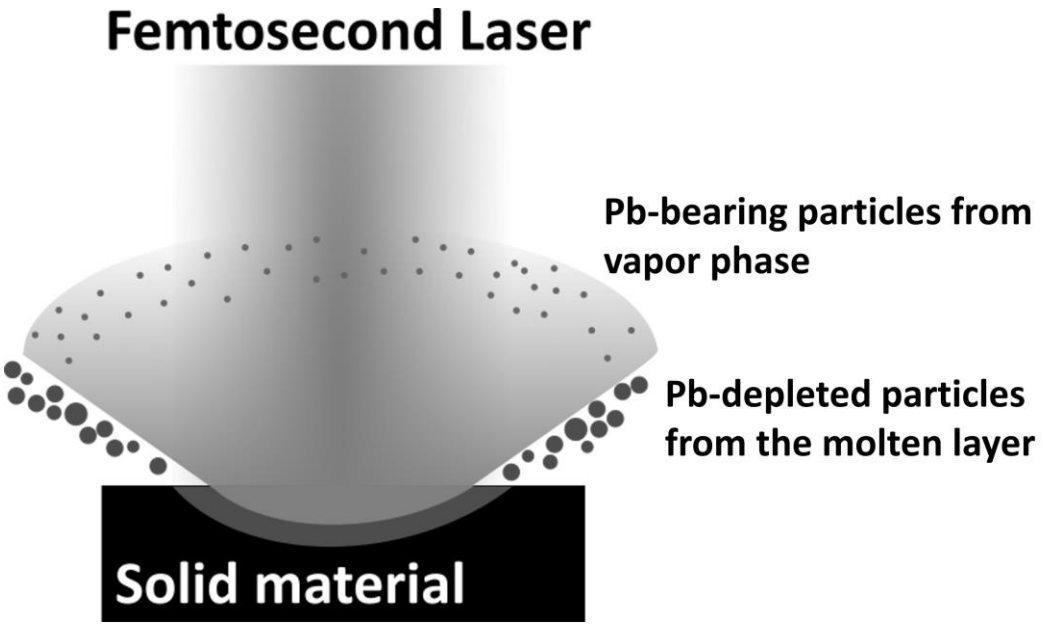

Figure 3.13 Schematic diagram for the generation and release processes of particles during femtosecond laser ablation. Pb-bearing particles are generated through condensation from the vapor phase, and Pb-depleted particles are released from the molten layer.

3.2.3.2 Fractionation of $^{208}Pb/^{232}Th$ through melting and evaporation/recondensation processes

Despite the decoupled $^{208}Pb/^{232}Th$ values in terms of the individual LA-generated particles, the $^{208}Pb/^{232}Th$ values calculated from the integration of all particle signals should be accurately measured by calibrating based on a matrix-matched reference. Then, the signal counts of all detected particles were integrated for each spot analysis. The correction factor for $^{208}Pb/^{232}Th$ is calculated by normalising the measured $^{208}Pb/^{232}Th$ value of the 16-F-6 monazite to 0.15102. The uncertainty of each spot analysis is reckoned based on the counting statistics of ^{208}Pb and ^{232}Th, and the relative standard deviation of $^{208}Pb/^{232}Th$ for the ten-spot analyses of the 16-F-6 monazite. The ^{232}Th–^{208}Pb ages were calculated under the assumptions of the negligible contents of non-radiogenic Pb and the closed Th–Pb isotope system after the crystallisation. Figure 3.14 shows the resulting ^{232}Th–^{208}Pb ages for two monazites. The weighted average of the ^{232}Th–^{208}Pb ages for the Namaqualand monazite is 1161 ± 120 Ma (95% confidence level) with the mean squared weighted deviation (MSWD) of 7.2. The obtained age is slightly older than the reported age. In contrast, the weighted average of the ^{232}Th–^{208}Pb ages for the 44069 monazite is calculated as 265 ± 23 Ma (95% confidence level) with the MSWD of 2.4, which is significantly younger than the reported age of 424.9 Ma.

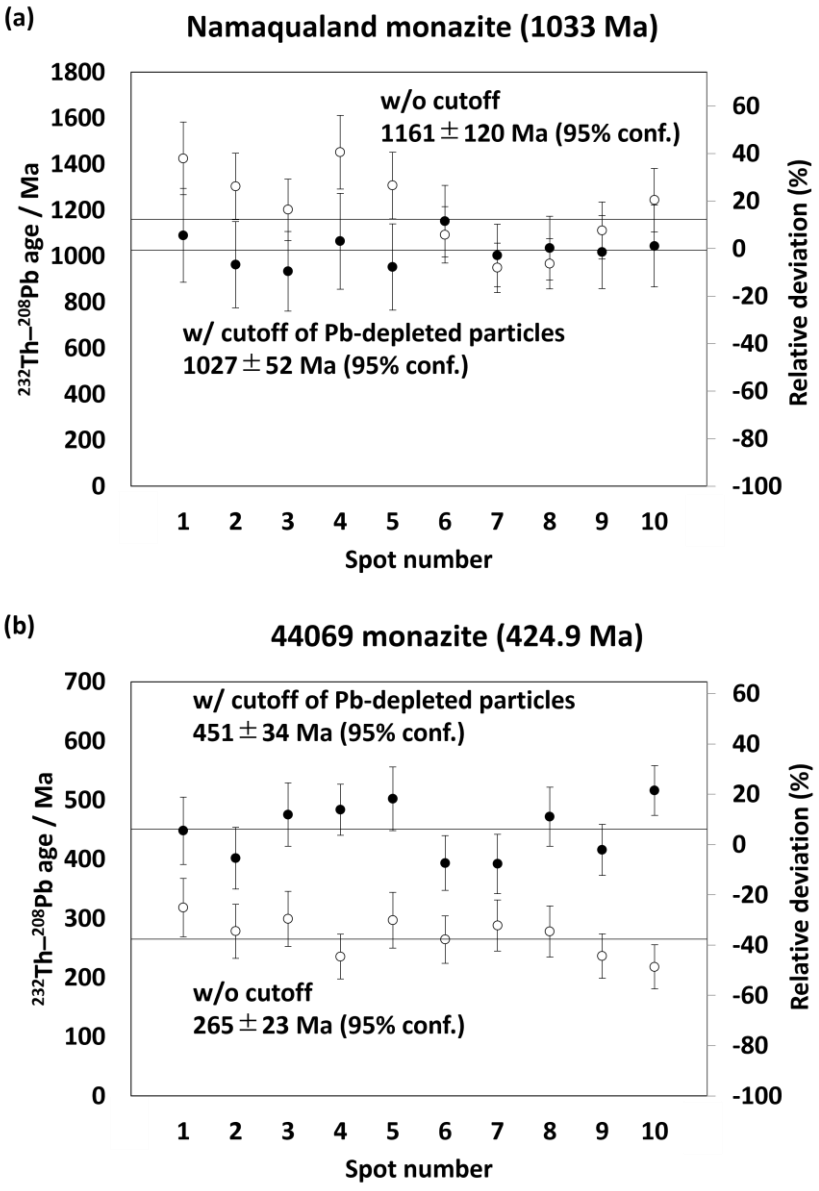

Figure 3.14 The resulting ^{232}Th–^{208}Pb ages for (a) the Namaqualand monazite and (b) the 44069 monazite. The open circles indicate the data without the cutoff, and the closed circles demonstrate the data with the cutoff of the Pb-depleted particles. The straight lines represent the averaged age values. The uncertainty shown as the error bars is 2s ranges. The right Y-axis represents the relative deviation (%) from the reference values.

The observed systematic deviation of the ^{232}Th–^{208}Pb ages is attributed to the different Th contents, and the contribution of the counting loss for high-intensity signals of ^{232}Th analysed with the pulse-counting system varies depending on the Th concentration. Figure 3.15 is a signal profile when detecting a large Pb-depleted particle with the signal count rate of more than 3×10^7 counts-per-second (cps) during the analysis of the Namaqualand monazite. The decreased signal count between the two peaks indicates the counting loss owing to the paralysation of the D5 detector based on a pulse-counting ion detection mode monitoring the ^{232}Th signal. The dead-time correction scheme applied in this study assumes the non-paralysable characteristics of the Daly detector, and the paralysed signal counts cannot be accurately corrected. The magnitude of the counting loss is more significant for samples with a higher-Th content yielding paralysed ^{232}Th signals more frequently. As a result, the $^{208}Pb/^{232}Th$ values can be overestimated, particularly in the case of the Namaqualand monazite with the highest Th content among three monazite references. The cause of this systematic deviation means that matrix-matched calibrations of elemental or isotope ratios require matrix-matched references with equivalent concentrations of analytes, especially when analysing the ratios of major and trace elements. The systematic deviation due to the paralysation of ion counters can be also appeared in the pioneering research using fsLA-ICP-MS reporting the fractionation on Pb/Cu and Zn/Cu based on the matrix-unmatched calibration with brass (Fig. 3.7).[66] The brass used in the previous study contained Cu as the most abundant component (ca. 80%), and the introduction of Cu-bearing coarse particles into ICP can cause the similar counting loss of ^{65}Cu. In this context, the concentration of analytes is important in terms of matrix-matching.

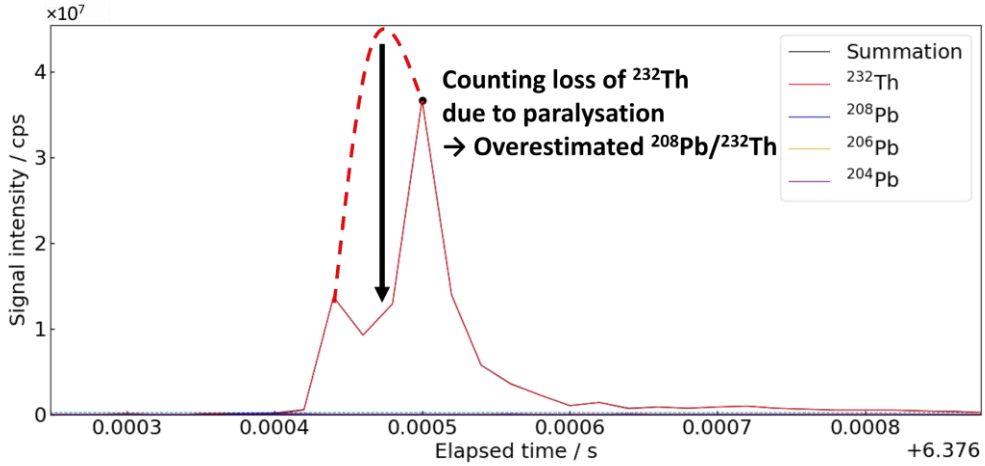

Figure 3.15 Time-resolved isotope signal profiles of a large Pb-depleted particle acquired from a single-shot LA on the Namaqualand monazite, demonstrating the counting loss of ^{232}Th owing to the paralysation of the Daly detector.

Hence, the inaccurate calibration of ^{208}Pb/^{232}Th is due to the integration of signal counts from the coarse Pb-depleted particles, which is potentially affected by the counting loss of ^{232}Th. Then, the ^{208}Pb/^{232}Th values are reckoned from the summation of the Pb-bearing particles without the Pb-depleted particles. The correction factor for ^{208}Pb/^{232}Th calculated from the ten-spot analyses was 1.72 ± 0.12 (1SD). The factor is regarded as the Pb-enrichment factor in the LA-induced plume compared to the original composition. The resulting ^{232}Th–^{208}Pb ages for the Namaqualand monazite and the 44069 monazite are 1027 ± 52 Ma (95% confidence level) with the MSWD of 0.61 and 451 ± 34 Ma (95% confidence level) with the MSWD of 3.9, respectively, shown in Figure 3.14. These acquired ages are in good agreement with the previously reported ages of 1033 Ma for the Namaqualand monazite and 424.9 Ma for the 44069 monazite. The better accuracy of the ^{232}Th–^{208}Pb dating method with the discrimination of the Pb-bearing particles based on the HTR-MC-ICP-MS is demonstrated compared to that based on the integrated counts of all detected particles. In conclusion, the ^{232}Th–^{208}Pb dating of monazite with the spot size of ca. 2 μm is achieved with the separate analyses of the LA-generated particles, allowing for the discrimination of the Pb-bearing particles by utilising LA-HTR-MC-ICP-MS.

3.2.4 Conclusion

This study firstly reports the elemental/isotopic ratios of nanoparticles generated by fsLA based on the direct analysis utilising HTR-MC-ICP-MS. The notable thing is that Th demonstrating the refractory feature is present in two types of particles, and this is a critical cause for the necessity of matrix-matching references for elemental and isotopic analysis. This section concludes with the following three conclusive remarks.

1. The analysed particles derived from fsLA on monazite demonstrate two decoupled Pb/Th compositions of Pb-bearing particles and Pb-depleted particles. The Pb-depleted particles can be emanating from the molten sub-surface layer, and the Pb-bearing particles are condensed from the gaseous phases. The ratio of molten and vaporised masses during laser ablation can vary based on the physicochemical properties of matrix components, and the variation leads to the matrix effect during LA.

2. For ^{232}Th–^{208}Pb dating of monazite, the Pb-depleted coarse particles are the main cause for the counting loss of ^{232}Th. The systematic error is derived from the paralysation of the ion counter where the signal intensity exceeds 3×10^7 cps by the introduction of the coarse particles, and the deviation cannot be corrected by a conventional correction method based on the non-paralysable model. This results in the inaccurate correction of $^{208}Pb/^{232}Th$ due to the matrix-unmatched calibration in terms of the Th concentrations.

3. This matrix-unmatched calibration is avoided using only Pb-bearing particles for calculating $^{208}Pb/^{232}Th$ without using potentially inaccurate data of Pb-depleted particles, and the obtained ^{232}Th–^{208}Pb ages with the laser spot size of ca. 2 μm for the Namaqualand monazite and the 44069 monazite are in good agreement with the reported values. The analytical accuracy of the ^{232}Th–^{208}Pb dating method of monazite based on the fsLA-HTR-MC-ICPMS protocol is demonstrated.

3.3 Mass spectrometric interference

Deviations in isotopic ratios resulting from mass spectrometric interferences translate directly into errors in radioisotope age determinations. Hence, mass spectrometry used for radioisotope dating methods demands a low production rate of interfering ions and a high capacity for removal of interferences.

Mass spectrometric interferences are particularly problematic for *in situ* isotope analysis conducted to derive reliable chronological information from mineral crystals. For *in situ* isotope analysis without sample decomposition and subsequent separation of analytes from matrix elements, the contribution of interferences derived from sample matrices is inevitable. Hence, hard ionisation is desired for suppressing the production of interferences including polyatomic ions, and Ar-based ICP with the high temperature of more than 5000 K is a primary option among ion sources used in inorganic mass spectrometry.[54] For Quaternary geochronology based on the ^{238}U-series isotope systematics, however, accurate measurements of trace isotopes involved in age determinations are required, and a minimal contribution of interferences corresponding to the concentration level on the order of ng g^{-1} is necessary.

Faced with the problem, a novel analytical protocol for removal of interferences on *m*/*z* 230 is developed based on collision cell technique equipped with quadrupole-based ICP-MS, and the contribution of interfering ions is reduced to negligible levels for ^{238}U–^{230}Th dating of Quaternary minerals by the present technique. The contents of the section 3.3 include the published article by Niki and the co-author entitled with "Development of an *in situ* U-Th disequilibrium dating method utilising multiple-spot femtosecond laser ablation-CRC-ICP-MS".[41]

3.3.1 Introduction

3.3.1.1 Mass spectrometric interferences on *m*/*z* 230

The first report of the ^{238}U–^{230}Th dating method using LA-ICP-MS applied to zircon was made by Ito (2014).[91] The ICP-MS system used in the previous study was sector field-based ICP-MS (ICP-SF-MS) operating with a low mass resolution ($M/\Delta M$ = 300). Based on the system setup without the resolving power, the obtained age data were susceptible to mass spectrometric interferences. The interferences deteriorate the signal-

to-background ratio at *m*/*z* 230 where background counts include signal counts observed without sample introduction into MS, signal counts from polyatomic ions derived from sample matrices, and tailing signal counts from adjacent peaks. In fact, contribution of interferences on *m*/*z* 230 derived from the zircon matrix were significant.[67] The major interference is zirconium-related polyatomic ions, such as $^{90}Zr^{92}Zr^{16}O_3^+$, and $^{91}Zr_2{}^{16}O_3^+$. When using N_2 make-up gas for sensitivity enhancement, $^{90}Zr^{96}Zr^{14}N_2{}^{16}O^+$ and $^{92}Zr^{94}Zr^{14}N_2{}^{16}O^+$ are also observed.[92] Another important interference is signal tailing from adjacent peaks, such as $^{232}Th^+$. A typical abundance sensitivity of ICP-SF-MS is 2–3 ppm, and the contribution of the tailing to the signal intensity of ^{230}Th is more than a few percent.[67] To resolve the tailing, higher abundance sensitivity is required.

To reduce the contribution of interferences, separation of analytes and interferences with medium- or high-mass resolution is a basic option. Despite the complete separation, the lowering of ion transmission through MS with a medium mass resolution results in poor precision of ^{238}U-^{230}Th isotope ratios. Then, another method using correction for the interferences was proposed by Guillong and the co-authors.[35] Based on the correction protocol, the signal intensity of polyatomic interferences at *m*/*z* 230 is estimated through monitoring the signal intensity at *m*/*z* 228 under the assumption that the polyatomic interference is only come from $Zr_2O_3^+$, and other polyatomic ions can be ignored. Subsequently, the contribution of the estimated signal intensity for polyatomic interferences on *m*/*z* 230 and the tailing of $^{232}Th^+$ determined from the abundance sensitivity is subtracted from the total signal intensity at *m*/*z* 230. This analytical protocol is performed with a low mass resolution, and reduction of sensitivity is avoided. Although the correction method appears to be effective, achieving the low production rates of polyatomic interferences while monitoring oxide ion production rates is key to minimising systematic and random errors associated with the correction, and the correction scheme is vulnerable to unidentified interferences.

With the contribution of possible interferences, determination of isotope ratios is erroneous. Reduction of the interfering ions can be conducted using collision cell technique (CCT) equipped with quadrupole-based MS. Through the collision cell inside a mass spectrometer, interference ions can be eliminated through the collision with gases, such as He, H_2, O_2, or NH_3, and the CCT is important for reducing the contribution of polyatomic ions derived from matrix components.[93]

In this study, for improvement in the SBR, the kinetic energy discrimination (KED) of the CCT utilising He collision gas was firstly applied to the *in situ* ^{238}U–^{230}Th dating method using LA-ICP-MS.[41] The KED mode is effective for reducing the signal intensities of polyatomic ions including $Zr_2O_3^+$ through the collisional loss of the kinetic energy. Inside the collision cell, the kinetic energy of polyatomic ions decreases significantly compared to the energy loss of $^{230}Th^+$ since the frequency of collision with He is greater for polyatomic ions because of the larger collisional cross section (Fig. 3.16).[94, 93] This causes the difference in the kinetic energy among polyatomic ions and $^{230}Th^+$, and then, by setting an appropriate bias energy barrier between the collision cell and the subsequent quadrupole mass filter, polyatomic interference ions can be eliminated whereas $^{230}Th^+$ is preferentially introduced into the mass filter (i.e., energy discrimination). In addition to the reduction of polyatomic interferences, thermalisation of ion beams through the collision cell is important for improvement of the abundance sensitivity.[95] Among several gas species, He as the lightest inert element is promising because of the absence of byproducts generated inside the collision cell and a suppressed collision-induced scattering effect resulting in keeping the ion transmission of $^{230}Th^+$ through the collision cell.

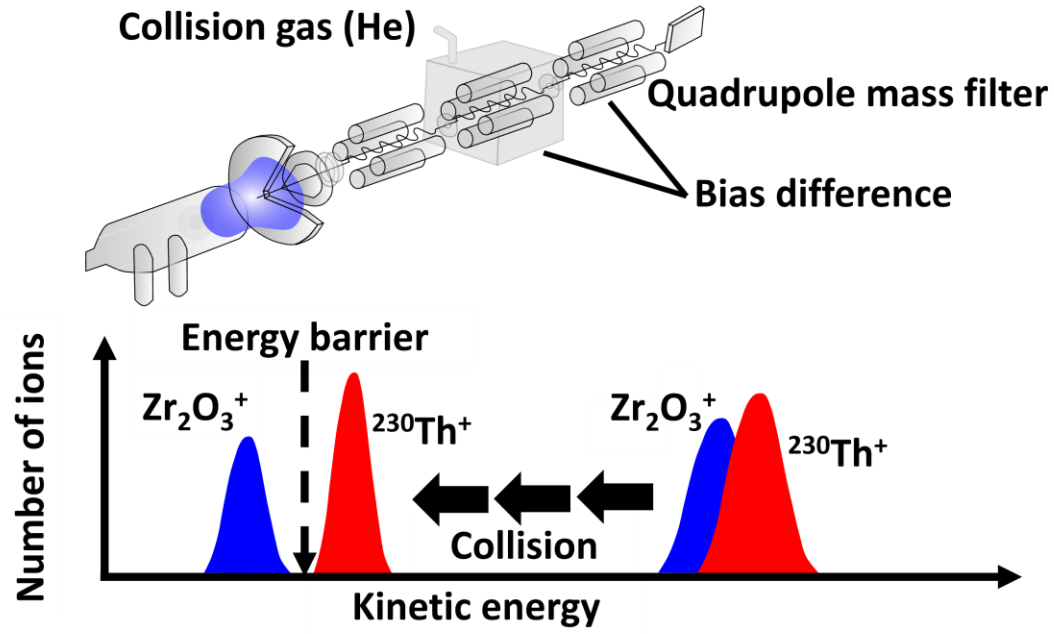

Figure 3.16 Schematic diagram of kinetic energy discrimination (KED) using collision cell technique.

3.3.1.2 Enhancement of SBR

Despite the importance of capability for reducing the interferences based on the KED mode, a major drawback is about one order of magnitude less elemental sensitivity for quadrupole-based MS with CCT compared to sector-field-based MS. The difference in the ion transmission through MS mainly depends on the kinetic energy, and the kinetic energy of ions inside the quadrupole-based MS is less than 100 eV, and this is significantly lower than that for sector-field-based MS ranging from 6 to 10 keV. The acceleration voltage of less than 100 V of the quadrupole-based MS results in the lower extraction efficiency and ion transmission through MS. Hence, as well as the reduction of background counts using the KED mode, the enhancement of the signal intensity obtained through LA-ICP-MS is important to detect the minor abundance of ^{230}Th with the improved SBR (Fig. 3.17).

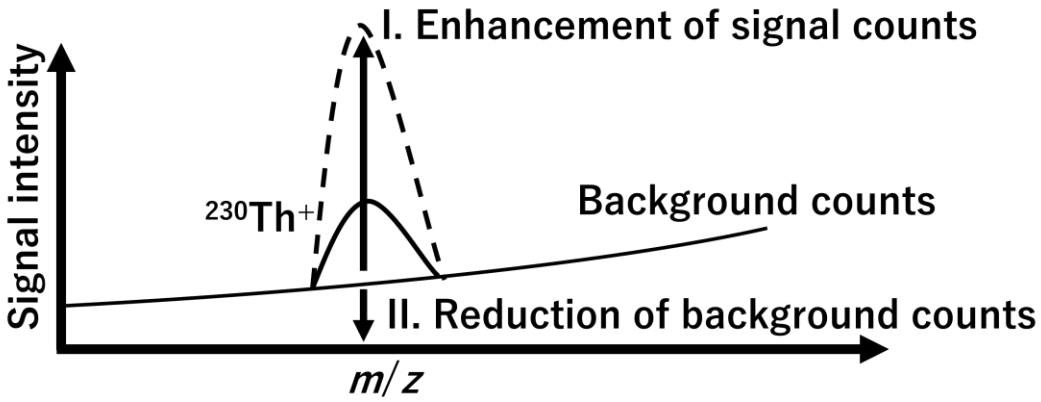

Figure 3.17 Two strategy for improvement in the signal-to-background ratio of $^{230}Th^{+}$.

To acquire the high signal intensity of ^{230}Th, two approaches are adopted in this study: (a) enhancement of the elemental sensitivity through the improvement in the ion transmission, and (b) increase of SBR by sample introduction within a short time duration. Toward the first strategy, the elemental sensitivity can be enhanced through the improvement in the vacuum interface region. The critical drawback of the ICP-MS system is that the low ion transmission through the vacuum interface. By using a sensitivity-enhanced dry sampling cone,[96] the expansion of the ion beams is supressed, and the ion transmission increases nearly threefold for heavy elements including lanthanides, Th and U.[97] The resulting useful yield of the LA-ICP-MS system is ca. 0.1%. This sensitivity is almost a half of that achieved by LA-ICP-SF-MS in the previous study.

The second scheme of fast sample introduction is achieved by utilising the high-repetition-rate LA with the Galvanometric optics (i.e. multiple-spot LA).[98] The multiple-spot LA is carried out within a short duration utilising the combined system of a high-repetition-rate laser (i.e., 1 kHz) and high-speed scanning mirrors. Using the multiple-spot LA system enables ablation pits with the size of ca. 10 μm to move at the velocity exceeding 20 m s^{-1}. This rapid movement is facilitated by changing the angles of two rotating mirrors. Based on the technique, large areas of up to 1 mm^2 are ablated within a few seconds, and subsequently, the LA-generated particles are introduced into ICP. With the 1 kHz LA, the resulting count rate at *m*/*z* 230 is more than an order of magnitude enhanced compared to conventional low-repetition-rate LA (i.e., 10 Hz). This high-count

rate enables to analyse ^{230}Th with the improved SBR and the high throughput. Then, the multiple-spot LA-ICP-MS system with CCT is a suitable choice for the *in situ* ^{238}U–^{230}Th dating method (Fig. 3.18).

In this study, the instrumental setup was firstly optimised based on the analysis of reference materials, and then, the reliability of the present technique was demonstrated through the ^{238}U-^{230}Th isotopic data of zircon references. Finally, acquired age data by the present technique is shown for four Quaternary samples collected from volcanic products, whose eruption times were previously determined from other chronological techniques including the fission-track (FT) dating method and radiocarbon dating method.

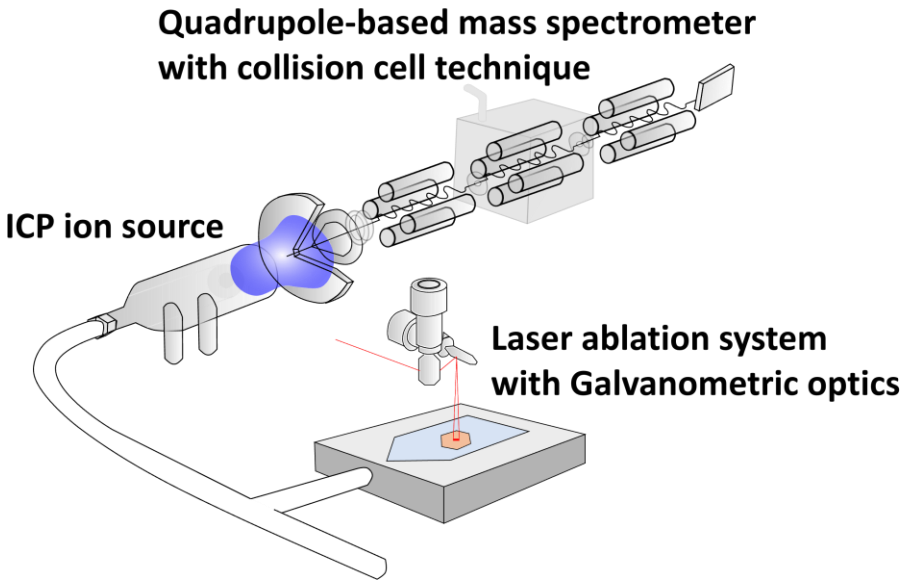

Figure 3.18 Schematic diagram of multiple-spot LA-ICP-MS with collision cell technique.

3.3.2 EXPERIMENTAL

3.3.2.1 Optimisation of instrumental conditions

The quadrupole-based ICP-MS equipped with CCT utilised in this study was an iCAP TQ (Thermo Fisher Scientific, Bremen, Germany). For the enhanced sensitivity, the dry sampler cone (part number 319-646; Nu Instruments, Wrexham) was attached. The LA system employed in this study was a Jupiter Solid Nebulizer (ST Japan, Japan)

equipped with a Yb:KGW femtosecond laser and the Galvanometric optics. The operating conditions of ICP-MS including gas flow rates and ion lens settings were optimised through the raster scan analysis of a glass reference (NIST SRM 610) with a laser pit size of 10 μm, fluence of 7 J cm^{-2}, repetition rate of 10 Hz, and laser raster speed of 2 μm s^{-1} to maximise the signal intensity of ^{238}U while the production rate of ThO^+/Th^+ was less than 1%. Although sensitivity can be further enhanced with higher Ar and He gas flow rates under the increased ThO^+/Th^+, Th/U measurements can be erroneous due to the cooling of ICP. Subsequently, the operational setting of the KED mode was optimised. The optimised parameter was the KED bias difference between the collision cell and the subsequent quadrupole mass filter. As the KED bias difference increases, the capability of eliminating polyatomic ions is improved, and the ion transmission decreases, and tuning of the appropriate KED bias difference is required.

To evaluate the capability of reducing polyatomic interferences at *m*/*z* 230, especially derived from zircon, a natural zircon reference (Nancy 91500)[99] and a synthetic zircon were analysed. The synthetic zircon provided by Dr. Isamu Shinno was crystallised based on the method of Chase and Osmer (1966) at 1250–900 ºC.[100] The synthesised zircon has negligible concentrations of U and Th being less than 0.1 μg g^{-1}, and the signal counts obtained from the synthetic zircon at *m*/*z* 230 are regarded as zircon-matrix-related polyatomic ions while the signal counts from the natural zircon reference containing the U concentration of 81.2 μg g^{-1} are the summation of $^{230}Th^+$, polyatomic interferences, and the tailing from $^{232}Th^+$.

Figure 3.19(a) demonstrates the signal counts at *m*/*z* 230 acquired through the analyses of the zircons by LA-ICP-MS based on the LA conditions of a sampling volume of 50×50×6 $μm^3$, a repetition rate of 1,000 Hz, and fluence of 3 J cm^{-2}. In this study, the collision cell bias was fixed at -21 V and the quadrupole bias was optimised to obtain minimum interferences on ^{230}Th while enhancing the SBR defined by the ratios of the signal counts from the Nancy 91500 zircon and those from the synthetic zircon. Figure 3.19(a) indicates that the higher KED bias difference causes both the ion transmission and polyatomic interfering ions. The notable thing is that the reduction of signal counts from polyatomic ions is more significant compared to the signal counts from the Nancy 91500 zircon. At the low KED bias voltage, significant deviations from the $^{230}Th/^{238}U$ value in secular equilibrium are observed, and, as the KED bias difference increases, it approaches

the value in secular equilibrium shown in Fig. 3.19(b). Then, the SBR shown in Fig. 3.19 (b) is maximised at the KED bias difference of 5 V. The ion transmission decreases 13% with the increase of the KED bias difference by 1 V within the range of 3–7 V. Considering from both the capability of removing polyatomic ions and the ion transmission based on the SBR, the optimised KED bias difference is 5 V. The resulting operation conditions of multiple-spot LA-ICP-MS with CCT are summarised in Table 3.2.

The abundance sensitivity is also important for resolving the tailing from $^{232}Th^{+}$. The obtained mass spectrum based on the analysis of NIST SRM 610 with the Th concentration of ca. 460 μg g^{-1} shown in Fig 3.19(c). The resulting background counts at *m*/*z* 230.5 are below the detection limit, and the resulting contribution of the tailing from $^{232}Th^{+}$ to $^{230}Th^{+}$ (i.e., abundance sensitivity) is better than 0.01 ppm. The abundance sensitivity is improved by two orders of magnitude compared to the conventional ICP-SF-MS system.[67] Therefore, the contribution of the background counts at *m*/*z* 230 is less than 0.1% for zircon, and less than 1% even for monazite enriched in Th.

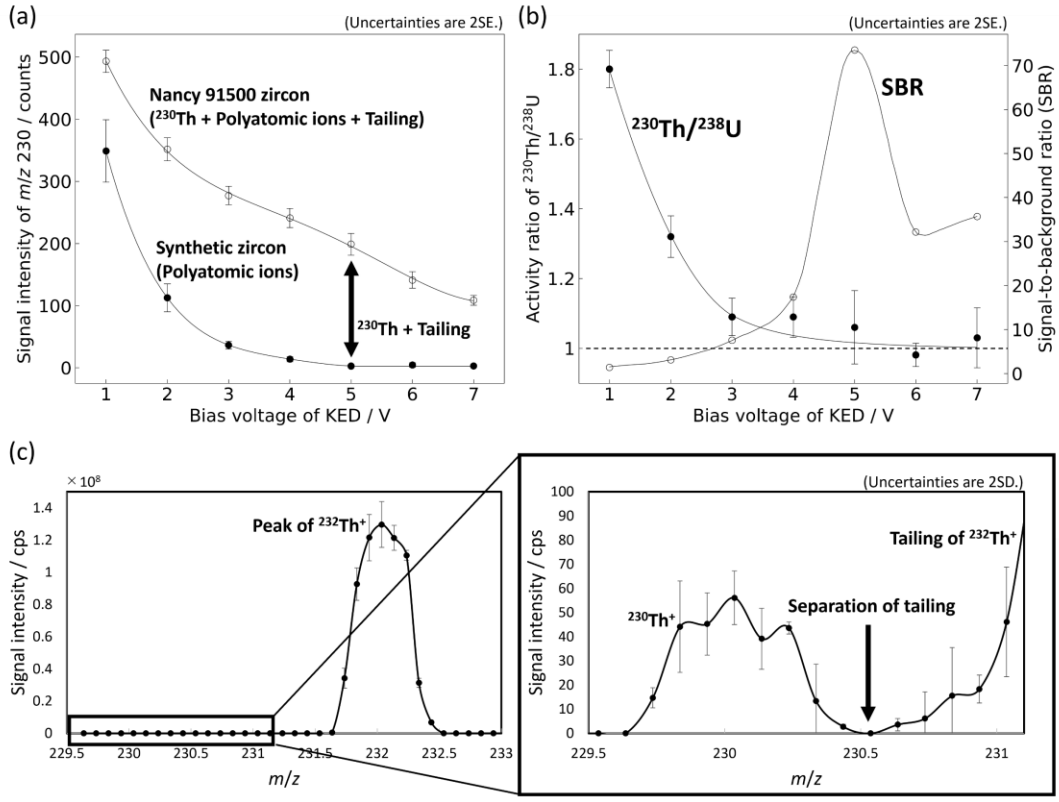

Figure 3.19 Effect of the KED bias difference on the signals of interference ions and ^{238}U–^{230}Th isotope signals. (a) Signal intensities at *m/z* 230 acquired for a synthetic zircon (closed circle) and the Nancy 91500 zircon (open circle). (b) $^{230}Th/^{238}U$ activity ratios for the Nancy 91500 zircon plotted against the KED bias difference (closed circle). The open circles demonstrate the SBR of ^{230}Th, suggesting that a KED bias difference of 5 V provides the highest SBR. (c) Mass spectrum obtained from the analysis of NIST SRM 610 to evaluate the contribution of the background counts from $^{232}Th^{+}$.

With the KED setting, the measured loss of the ion transmission of ^{230}Th through the enhanced KED was only about 30% compared to a usual condition. This is significantly smaller than the decrease in the ion transmission by a factor of ten operating at a high- or mid-mass-resolution mode. The resulting sensitivity of the multiple-spot LA-ICP-MS with CCT employed with the sensitivity-enhanced dry sampler cone is about one-third to half compared to the previously reported sensitivity of LA-ICP-SF-MS for the ^{238}U–^{230}Th dating method, and the present technique is now a viable option for the *in situ* ^{238}U–^{230}Th dating method. The critical advantage of the present technique is that no correction of background counts is necessary to obtain accurate ^{238}U–^{230}Th ages.

Moreover, with the multiple-spot LA technique using the high-repetition-rate laser ablation, time duration required for spot analysis is reduced to about a second, and

the SBR and the analysis throughput is improved. In this study, a multiple-spot LA sampling volume of 35×35×8 μm^3 for ^{238}U–^{230}Th dating of mineral samples was used, and the resulting sensitivity was more than 30 cps/ppb (Fig. 3.20). The sampling volume was nearly equivalent to previous studies using the LA-ICP-SF-MS.[35)]

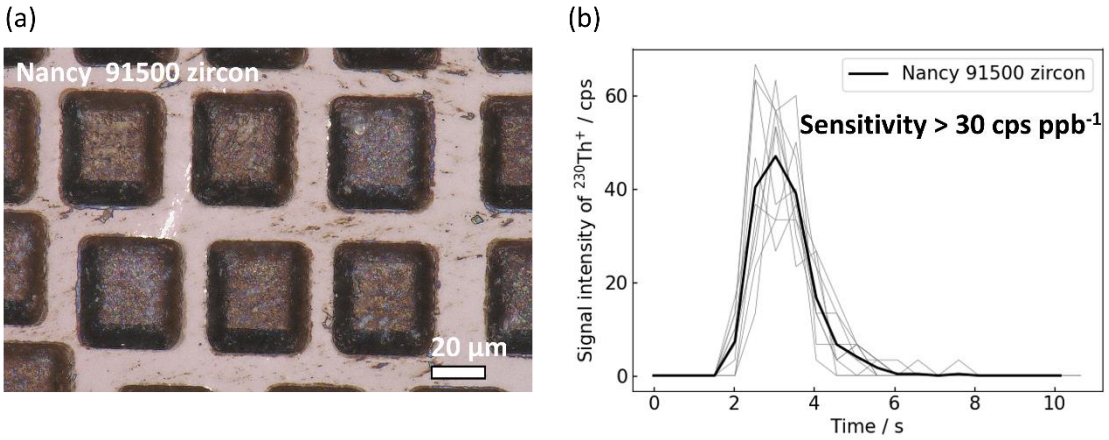

Figure. 3.20 Photographic image of laser ablation areas and the resulting signal intensity profile of ^{230}Th. (a) Ablation areas of Nancy 91500 zircon with a sampling volume of 35×35×8 μm^3. (b) Signal intensity profiles of ^{230}Th obtained from ten-times repeated analyses for the Nancy 91500 zircon using high-speed multiple spot laser ablation. The black line represents the averaged signal intensity profiles (N = 10).

3.3.2.2 Reference materials and Quaternary samples

In this study, four zircon reference materials (Nancy 91500, Plešovice, GJ-1, and OD-3)[99, 101, 102, 103] were analysed to evaluate the data quality (accuracy and precision) obtained by the present LA-ICP-MS technique. All the reference materials subsidised to the isotope analysis are old enough to achieve the secular equilibrium, indicating that the $^{230}Th/^{238}U$ values are regarded as 1.692×10^{-5}, defined based on the decay constants for ^{238}U (1.55125×10^{-10} yr^{-1})[104] and ^{230}Th (9.1706×10^{-6} yr^{-1}).[28] In contrast, for the OD-3 zircon, it is widely recognised that the measured $^{230}Th/^{238}U$ value was slightly deviated from the value in secular equilibrium where the activity ratio of $^{230}Th/^{238}U$ being 1.06 ± 0.03.[35]

In this study, four Quaternary samples (Toya, Sambe Kisuki, Hikageyama, Susaki Pumice) produced through the volcanic activities of different ages were subsidised to evaluate the data quality of the present technique.

(1) **Toya**: Heavy mineral fractions were collected from a pumice-rich layer of the unit 5b belonging to a Toya tephra in Hokkaido prefecture, Japan. The sample locality was separately described in previous study by Goto et al. (2018).[105] The heavy mineral fractions contain zircon and monazite, and twenty-seven grains for zircon and two grains for monazite were analysed. The eruption timing of the tephra from the Toya caldera is ranging from 106 to 113 ka based on the oxygen isotope stratigraphy.[106, 107] In the previous study, the reported zircon U–Pb age is 106 ± 13 ka, and the ^{238}U–^{230}Th isochron age is 132 ± 29 ka (95% confidence level) based on LA-ICP-SF-MS with a low mass resolution.[91] Despite the large uncertainty, the ^{238}U–^{230}Th isochron age can be erroneous without considering the mass spectrometric interferences.[67]

(2) **Sambe Kisuki (SK)**: The zircon grains were separated from the Sambe Kisuki (SK) tephra erupted from the Sambe volcano in Shimane prefecture, Japan. The sampling locality of the SK tephra is described in Kimura et al. (1999).[108] In the relevant area, magmatic activity started at about 100 ka and the SK tephra was found in the lowest part from the tephra sequences of the Sambe volcano. The eruption age was estimated as ca. 110 ka from the tephra stratigraphy constrained by the Ata tephra (ca. 105 ka)[109] and the Toya tephra (106–113 ka).[107] Among the volcanic products from the Sambe volcano, the SK is a known widespread tephra for linking the

Quaternary tephra stratigraphy in western and eastern Japan.[109] The previously reported radiometric age for zircon separated from the SK tephra was 100 ± 20 ka based on the zircon FT dating method.[108]

(3) **Hikageyama (HKG)**: The zircon grains were collected from the Hikgaeyama dacite lava, also located in the Sambe volcano. The sampling locality was the northeast area of Mt. Hikageyama (35°07'28"N 132°38'27"E).[110] Although the Hikageyama lava is classified into the lowest deposit at Stage IV of the Sambe volcano activity,[111] geochronological information including the eruption age of the Hikageyama lava is poorly studied. The Hikageyama lava is stratigraphically identified between the Hatasedani pyroclastic flow deposit at Stage IV (ca. 16 ka; Fukuoka and Matsui 2002) and the Sambe Ikeda tephra at Stage III (ca. 50 ka; Machida and Arai 2011, 46295 ± 418 cal BP; Maruyama et al. 2019).[109, 112] The eruption age was estimated by K–Ar dating, but it should be noted that the resulting eruption age of the Hikageyama lava by K–Ar dating was erroneous due to large contribution of air contamination.[113]

(4) **Susaki Pumice (SP)**: The zircon grains were collected from the Susaki Pumice in Shinjima island, Kagoshima, Japan. Shinjima island is located at the centre of the Aira caldera and was exhumed through the Anei eruption (A.D. 1779–1780). The sampling locality of the Susaki Pumice was separately reported in a previous publication.[114] The eruption age of the Susaki Pumice was older than 15 ka based on the ^{14}C dating for the Moejima formation (14620 ± 40 years before present).[114] The FT age was 16 ± 4 ka (95% confidence level) obtained from total 945 grains of the SP zircon (Kameyama et al. 2005).[114]

3.3.2.3 Calculation Procedures

The U–Pb isotopic analysis begins with the analysis of gas blank signals. Signal intensities of ions with m/z being 29, 230, 232, 235, and 238 were acquired for ten seconds, and the averaged signal intensity data were used for blank corrections for each isotope. The analysis of the blank intensity was followed by the data acquisition of ^{29}Si, ^{230}Th, ^{232}Th, ^{235}U, and ^{238}U of calibration standards for the correction of the mass bias and elemental fractionation on $^{232}Th/^{238}U$ and the mass discrimination on the $^{230}Th/^{232}Th$. To improve the signal-to-background ratios of the monitored isotopes, laser ablation was

carried out with a short-time duration using the high-repetition laser ablation (i.e., 1 kHz). Instrumentation and operating conditions are summarised in Table 3.2.

Table. 3.2 Instrumentation and operational settings

(a) ICP-MS	
ICP-MS instrument	iCAP TQ ICP-MS (Thermo Fisher Scientific, Bremen, Germany)
Sample introduction	Laser ablation
RF power	1550 W
Detection system	Secondary electron multiplier
Monitored mass-to-charge ratio	29, 230, 232, 235, 238
Integration time	0.3 s for *m*/*z* 230
	0.05 s for *m*/*z* 29, 232, 235, 238
Collision/reaction mode	KED mode using He
Collision gas flow (He)	4.0 ml min^{-1}
Oxide production rate (ThO^+/Th^+)	0.76%
(b) Laser Ablation	
Laser ablation system	Jupiter Solid Nebulizer (ST Japan Inc., Tokyo, Japan)
Laser medium	Yb:KGW
Laser wavelength	260 nm (4th Harmonic Generation)
Pulse width	290 fs
Fluence	ca. 3 J cm^{-2}
Repetition rate	1,000 Hz
He carrier gas	0.6 L min^{-1}
Ar make-up gas flow	1.0L min^{-1}
Sampling area and depth	50x50x6 μm^3 for optimisation of the KED conditions
	35x35x8 μm^3 for U–Th age determinations
He carrier gas flow	0.6 L min^{-1}
Time Duration of the laser ablation	ca. 1 s

The resulting signal profile of ^{230}Th is shown in Fig. 3.20(b). Intensity values for the analytes were calculated by integration of ion counts for 10 seconds. After the subtraction of the blank intensity, the resulting intensity values were used for further calculations. The mass bias and elemental fractionation effects on $^{230}Th/^{232}Th$ and $^{238}U/^{232}Th$ were externally corrected by normalising the ratios for the Nancy 91500 zircon. Hence, the $^{232}Th/^{238}U$ values calculated from $^{232}Th/^{235}U/137.88$ of the Nancy 91500 zircon were acquired for five times before and after the sample analysis, and averaged $^{232}Th/^{238}U$ (= $^{232}Th/^{235}U/137.88$) values obtained from total ten separated analysis spots were then used for the correction of mass bias effect on the $^{232}Th/^{238}U$ by normalising the measured ratios being 0.361 calculated based on the abundances of ^{232}Th (28.61 $\mu g\ g^{-1}$) and ^{238}U (81.2 $\mu g\ g^{-1}$).[99] The mass bias factor on $^{235}U/^{238}U$ was defined by normalising the measured ratios for the Nancy 91500 zircon being 0.0072527 calculated based on the natural $^{235}U/^{238}U$.[83] The mass bias factor on the $^{230}Th/^{232}Th$ were estimated by the measured $^{235}U/^{238}U$ values using the exponential law. Likely with the correction of the mass bias factor on $^{232}Th/^{238}U$, the mass bias effect on $^{230}Th/^{232}Th$ was corrected based on a sample-standard bracketing technique. The typical measured bias factors on

$^{232}Th/^{238}U$ and $^{235}U/^{238}U$ were 1.28 and 1.02, respectively. The variations in the correction factors during the analysis session were 1.8% for the $^{232}Th/^{238}U$, and 1.4% for the $^{235}U/^{238}U$.

Uncertainties of the measured $^{230}Th/^{232}Th$ and $^{232}Th/^{238}U$ were calculated based on equations (3.3) and (3.4), which were defined based on error propagation for both the counting statistics of the ^{230}Th, ^{232}Th, and ^{235}U signals and analysis repeatability calculated by ten-times repeated analyses of $^{235}U/^{238}U$ and $^{232}Th/^{235}U$ for the Nancy 91500 zircon. Typical ion counts of ^{230}Th obtained from samples with low-U contents were about 50 counts, suggesting that the uncertainties of the resulting age data were mainly controlled by the counting statistics of the ^{230}Th signals, rather than analysis repeatability estimated from the analyses of the reference material (Nancy 91500).

$$s\left(\frac{^{230}\mathrm{Th}}{^{232}\mathrm{Th}}\right) = \sqrt{\left(\frac{\sqrt{N_{230}}}{N_{230}}\right)^2 + \left(\frac{\sqrt{N_{232}}}{N_{232}}\right)^2 + \left(s\left(\frac{^{235}\mathrm{U}}{^{238}\mathrm{U}}\right)_{91500\ \mathrm{zircon}}\right)^2} \tag{3.3}$$

$$s\left(\frac{^{232}\mathrm{Th}}{^{238}\mathrm{U}}\right) = \sqrt{\left(\frac{\sqrt{N_{232}}}{N_{232}}\right)^2 + \left(\frac{\sqrt{N_{235}}}{N_{235}}\right)^2 + \left(s\left(\frac{^{232}\mathrm{Th}}{^{235}\mathrm{U}}\right)_{91500\ \mathrm{zircon}}\right)^2} \tag{3.4}.$$

where s, N_{232}, and N_{235} represent the relative standard deviation, ion counts of ^{230}Th, and ion counts of ^{235}U, respectively.

From the corrected $^{232}Th/^{238}U$ and $^{230}Th/^{232}Th$ values, the ^{238}U–^{230}Th isochron ages are firstly calculated, and then the ^{238}U-^{230}Th model ages are calculated based on the equation (3.5) using the ratio of partition coefficients (D_{Th}/D_U) between zircon and source melts.

$$\mathrm{t} = -\frac{\ln\left(\frac{\left(\frac{^{230}\mathrm{Th}}{^{238}\mathrm{U}} - \frac{\lambda_{238}}{\lambda_{230}-\lambda_{238}}\right)}{\frac{\lambda_{238}}{\lambda_{230}-\lambda_{238}}(\mathrm{D_{Th/U}}-1)}\right)}{(\lambda_{230}-\lambda_{238})} \tag{3.5}$$

where $\frac{^{230}\mathrm{Th}}{^{238}\mathrm{U}}$, λ_{230}, and λ_{238} denote the measured $\frac{^{230}\mathrm{Th}}{^{238}\mathrm{U}}$ values, decay constant of ^{230}Th, and decay constant of ^{238}U, respectively. It should be noted that this equation was defined under the assumption that radioactive equilibrium was achieved in the source melts.

The D_{Th}/D_U value of 0.14 ± 0.02 (coverage factor: k = 2) reported by Boehnke et al. was employed in this study.[24] In terms of the ^{238}U–^{230}Th model age, uncertainty in

the reported D_{Th}/D_U value can cause the systematic errors of about 3 kyr (coverage factor: $k = 2$). Regression lines and the weighted averages were calculated based on the modified York method using the Isoplot 4.15.[115, 116, 117)]

3.3.3 Results and discussion

3.3.3.1 Evaluation of Data Quality

The averaged $^{230}Th/^{232}Th$ activity ratio calculated from 110-spot analysis on Nancy 91500 zircon was 8.67 ± 0.24 (95% confidence level) with MSWD (mean squared weighted deviation) = 0.94 and the measured value is consistent with the reference value in secular equilibrium reconciled from the $^{238}U/^{232}Th$ value of 8.68. The $^{230}Th/^{232}Th$ activity ratios obtained from total data points of 65-spot analyses for the three zircon references (Plešovice, GJ-1 and OD-3) were plotted against the measured $^{238}U/^{232}Th$ values in Fig. 3.21. The slope of the regression line was close to unity (1.00 ± 0.01; 95% confidence level), and the value is in good agreement with the value in secular equilibrium. This strongly indicate the accuracy of the present technique.

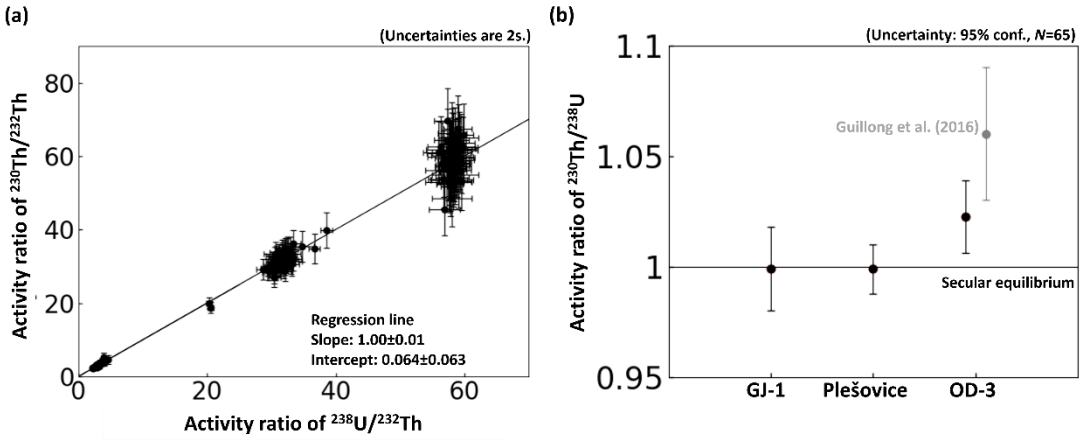

Figure. 3.21 The resulting $^{230}Th/^{238}U$ activity ratios for three reference materials. (a) The measured $^{230}Th/^{232}Th$ activity ratios are plotted against the $^{238}U/^{232}Th$ activity ratios (^{238}U–^{230}Th isochron diagram). Uncertainty indicates 2s. (b) Weighted averages of the $^{230}Th/^{238}U$ activity ratios for three zircon reference materials. Uncertainty (95% confidence levels) is provided for each reference material. The grey data point represents the previously reported value for the OD-3 zircon.

The weighted averages of the measured $^{230}Th/^{238}U$ activity ratios were 1.002 ± 0.019 (95% confidence level) with MSWD = 1.13, 1.023 ± 0.017 (95% confidence level) with MSWD = 0.94, 1.000 ± 0.011 (95% confidence level) with MSWD = 1.03 for the Plešovice zircon (Fig. 3.21(b)). The $^{230}Th/^{232}Th$ activity ratio for Nancy 91500 zircon and the $^{230}Th/^{238}U$ activity ratios for GJ-1 zircon and Plešovice zircon show excellent agreement with the value in secular equilibrium of the ^{238}U-^{230}Th system.

For the OD-3 zircon, the measured activity ratio of $^{230}Th/^{238}U$ deviates slightly from the secular equilibrium. It is noteworthy that a similar deviation was also reported by Guillong et al. ($^{230}Th/^{238}U$ activity ratio being 1.06 ± 0.03).[35] One may consider that the obvious discrepancy in the $^{230}Th/^{238}U$ activity ratio for the OD-3 zircon can be explained by possible mass spectrometric interferences on ^{230}Th. However, this is not the case because no clear differences in the chemical composition of OD-3 zircons over other zircons could be found. Moreover, possible mass spectrometric interferences on ^{230}Th were effectively reduced by the KED protocol employed in this study. This is also true for the contribution of the tailing from $^{232}Th^{+}$. Based on the present system setup and operational conditions, a level of contribution of signal tails on ^{230}Th from ^{232}Th is negligibly small (Fig. 3.19). Nevertheless this, the correction scheme for interferences was adopted by the pioneering studies by Guillong et al. (2016),[35] and thus, the similar level of discrepancies (i.e., 2%) found in the OD-3 zircon cannot be attributed to the contribution of mass spectrometric interferences. Another possibility is that erroneous correction of mass bias effect on $^{230}Th/^{238}U$ for the OD-3 zircon. However, the zircon crystals analysed in this study did not show clear differences in both chemical composition and crystallinity. Additionally, the deviation of $^{230}Th/^{238}U$ can be attributed to the ^{238}U–^{234}U radioactive disequilibrium. Despite the negligible magnitude of the ^{238}U–^{234}U radioactive disequilibrium in most igneous systems, one previously reported value of $^{234}U/^{238}U$ among thirteen spot analyses for the OD-3 zircon is higher compared to the equilibrium value.[118] Although the specific geological processes causing the disequilibrium remain unidentified, the higher $^{234}U/^{238}U$ reported for the OD-3 zircon is consistent with the observed higher $^{230}Th/^{238}U$. A potential solution for the future could be to incorporate ^{234}U as an additional isotope alongside those monitored in this study, in spite of the current single-collector system resulting in greater analytical uncertainty. At a moment we do not have any clear explanation for the discrepancy in the measured

$^{230}Th/^{238}U$ activity from the secular equilibrium, so this must remain a possibility. Despite this, the linear correlation in the $^{230}Th/^{238}U$ and $^{238}U/^{232}Th$ data for the zircon references demonstrate that the present technique can be a powerful tool applied for the *in situ* ^{238}U–^{230}Th dating method.

3.3.3.2 ^{238}U-^{230}Th ages of Quaternary samples

(1) Toya: The calculated U–Th isochron age of the Toya zircon for twenty-seven spot analyses was 111^{+24}_{-20} ka (95% confidence level) with a MSWD value of 1.04 (Fig. 3.22(a)). The MSWD value was nearly unity and no older grains, for instance data plotting on the equilibrium line, were found. The Toya sample contained two monazite grains and the combination of the data points of zircon and monazite yielded the isochron age of $113.5^{+5.4}_{-5.2}$ ka (95% confidence level) with the MSWD of 1.15 (Fig. 3.22(b)). The isochron age obtained with the combination of zircon and monazite demonstrates higher precision compared to the zircon isochron due to the wide variation of data points in the X-axis. The weighted average of the model age was $109.9^{+6.8}_{-6.4}$ ka (95% confidence level) with the MSWD of 1.19. These ages for the Toya sample are well consistent with the reported eruption age of the Toya tephra.[107)]

(2) Sambe Kisuki (SK): The resulting U-Th isotopic data obtained from 37 spots define the U–Th isochron age of $107.6^{+10.3}_{-9.5}$ ka with a MSWD value of 2.2 (Fig. 3.22(c)). The two data points were plotted on the equilibrium line (i.e., equiline), indicating that these two grains were crystallised prior to the eruption. This suggests that the some of the grains were potentially derived from the pre-Sambe volcano at about 1 Ma prior to the formation of the caldera or country-rock contamination. Except for two old grains plotted on the equiline, the calculated isochron age was $105.1^{+6.4}_{-6.1}$ ka (95% confidence level) with a MSWD value of 1.05 (Fig. 3.22(d)). The weighted average of the model ages was $111.4^{+9.5}_{-8.7}$ ka (95% confidence level) with a MSWD of 3.3. With the rejection of the two old grains, the weighted average of the model ages was $109.6^{+8.4}_{-7.8}$ ka (95% confidence level) with a MSWD of 3.0. These calculated ages, especially the two-point-rejected isochron age of $105.1^{+6.4}_{-6.1}$ ka, are consistent with the eruption age of ca. 110 ka and the zircon FT age of 100 ± 20 ka.[108,109)]

(3) Hikageyama (HKG): The resulting isochron age for the 30-spot analyses of the HKG

zircon was 20^{+26}_{-21} ka (95% confidence level) with the MSWD of 1.7 (Fig. 3.22(e)). Because of large contribution of the counting statistics on ^{230}Th ions and small variation of U/Th among zircons, the resulting isochron age was not precise enough to define the timing of the eruption between previously constrained 16 ka to 50 ka. To overcome this, the model ages were calculated from data points except for one spot demonstrating the secular equilibrium value within the 2s range. The weighted average of the specific model ages was now $55.2^{+7.7}_{-7.2}$ ka (95% confidence level) with the MSWD of 1.8 (Fig. 3.23(a)). This model age agreed with the eruption age of the Sambe Ikeda tephra (ca. 50 ka) within analytical uncertainties.[109)] As shown in Fig. 3.22(e) and Fig. 3.23(a), the one grain was plotting on the equiline and the model ages for two grains were significantly older than the average age defined as 2s ranges, suggesting that the ages of these grains can reflect the timing of the SK tephra, the pre-Sambe eruption or country-rock contaminants in the relevant area. Although crystallisation ages of zircon are not always corresponding to the eruption and crystallisation ages of zircons, our results of the U–Th model age were rather close to the eruption age of the Sambe Ikeda tephra. The resulting U-Th model age for the Hikageyama lave defined here is likely to be classified into Stage III. This is clearly inconsistent with the previous classification (i.e., classified into Stage IV by Fukuoka and Matsui 2002).[111)] The discrepancy in the classification can be attributed to the stratigraphic uncertainties for the volcanic stage for the Hikageyama lava. In fact, other pyroclastic deposits classified into Stage IV were identified from chemical or mineralogical compositions (e.g., cummingtonite contents).[111)] Despite the importance of lithology, this lithological classification was not applied to the Hikageyama lava. The classification of the eruption stage for the Hikageyama lava is severely dependent on the paraconformity of the Hikageyama lava and other pyroclastic deposits of Stage IV. The absence of direct observations for the stratigraphic relationships between the Hikageyama lava and the Sambe Ikeda pumice only indicates that the Hikageyama lava must postdate the deposition of the Sambe Ikeda pumice. Based on our results, a revised staratigraphy is proposed for the Hikageyama lava and this could affect the estimation of the time interval for stages of the Sambe volcano, which presumably reflected the restoring time for the magma chamber.

(4) Susaki Pumice (SP): The isochron age defined from fifteen-analysis spots was 18^{+15}_{-13} ka (95% confidence level) with a MSWD value of 1.5 (Fig. 3.22(f)). Because of the limited variations of the $^{238}U/^{232}Th$ values (X-axis in the Fig. 3.22(f)), resulting uncertainties in the ages are greater than other zircons. Despite the poor precision of the age data, the weighted average of the model ages ($16^{+4.2}_{-4.1}$ at 95% confidence level with MSWD = 1.7; Fig. 3.23(b)) shows a good agreement with both the ^{14}C age (14,620 ± 40 yrBP) and the FT age of zircon (16 ± 4 ka).[114] For more accurate and precise determination of the U–Th age, analysis for materials of both low- and high-U/Th values including volcanic glasses or phosphates are highly desired. To do this, of course, U–Th isotopic analysis with higher-elemental sensitivity is required.

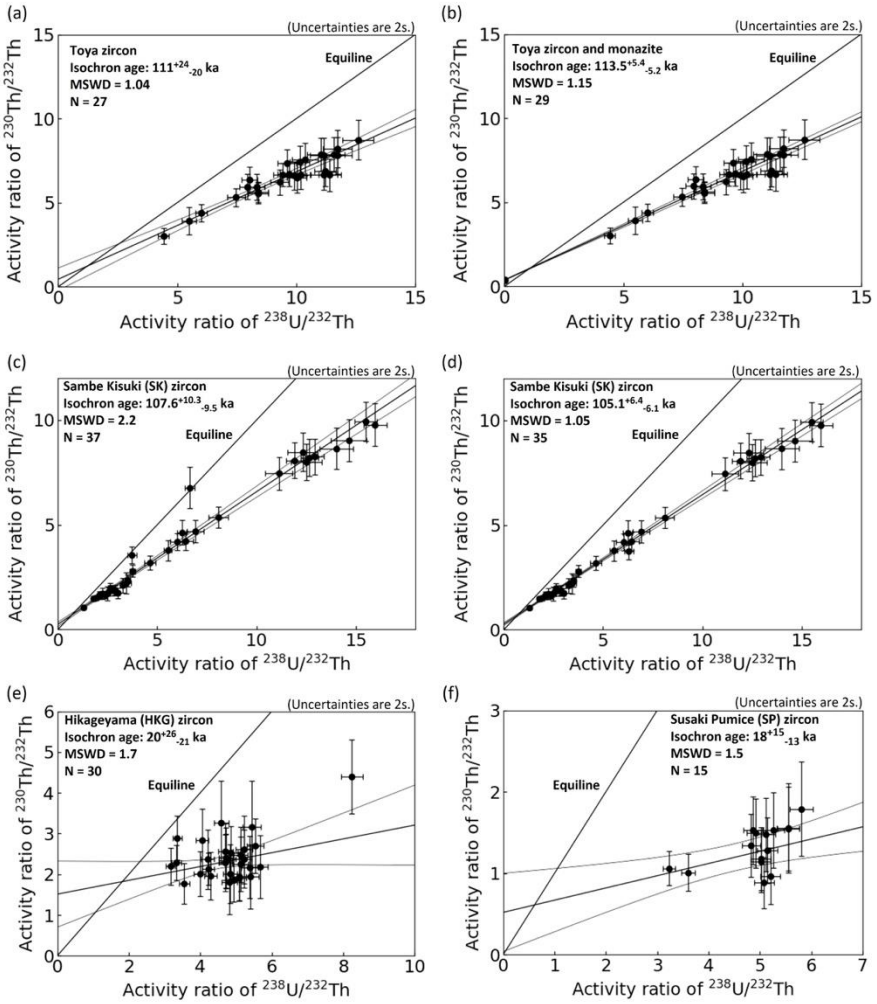

Figure. 3.22 The resulting ^{238}U–^{230}Th isochrons for Quaternary zircon and monazite samples analysed in this study. The measured $^{230}Th/^{232}Th$ activity ratios were plotted against $^{238}U/^{232}Th$ activity ratios for zircon from Toya (a), zircon and monazite from Toya (b), zircon from Sambe Kisuki (c), younger zircon from Sambe Kisuki (d), zircon from Hikageyama (e), and zircon from Susaki Pumice (f).

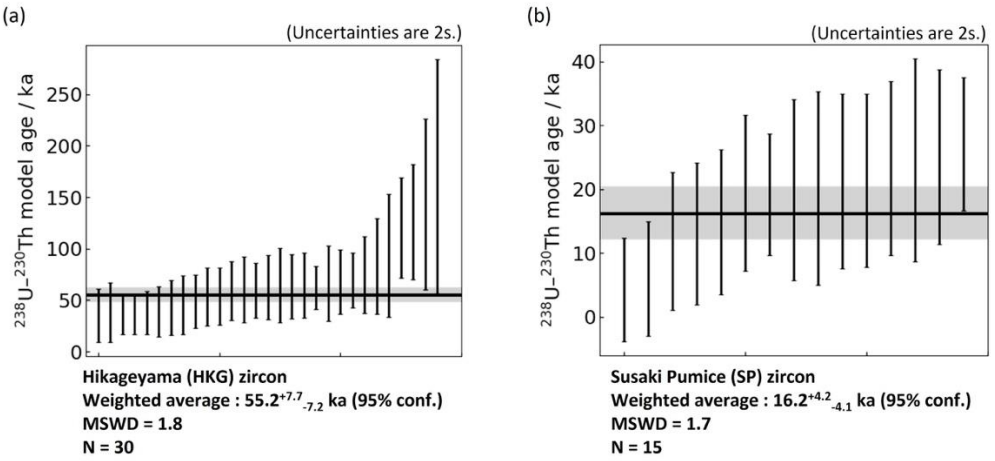

Figure. 3.23 The resulting ^{238}U–^{230}Th model ages obtained from individual analysis spot from zircons from Hikageyama (HKG) and Susaki Pumice (SP). Uncertainty for each spot analysis indicate 2s. The black horizontal lines represent the weighted averages of ^{238}U–^{230}Th model ages for HKG zircon (a) and SP zircon (b). Uncertainties of the weighted averages were given in the grey areas (confidence level of 95%).

3.2.4 Conclusive remarks

The basic conclusion obtained here demonstrates clearly that the kinetic energy discrimination (KED) mode employed in the ICP-MS system is an effective method for reducing various mass spectrometric interferences found in zircon matrices at *m*/*z* 230 with minimum loss of the ion transmission (30%) than the ICP-sector magnetic field-MS (ICP-SF-MS) operating under medium-mass-resolution mode. To conduct high-precision *in situ* ^{238}U–^{230}Th dating, the sensitivity-enhanced dry plasma cone was applied for further improvement of the transmission. Moreover, in this study, laser ablation from wide areas (e.g., 35x35 μm) was conducted within short time durations utilising a multiple spot-laser ablation protocol (msLA) to improve the signal-to-background ratio (SBR). The resulting sensitivity for ^{230}Th was more than 30 cps/ppb (ng/g) for solid materials analyzed in this study. Hence, sufficiently high sensitivity for the detection of ^{230}Th was achieved by the combination of a high-repetition-rate laser (1 kHz) and fast scanning Galvanometric optics. The resulting analysis throughput achieved by the msLA-CCT-ICP-MS was at least two times higher than that achieved by the LA-ICP-SF-MS,[35] suggesting that the technique can become a principal choice for the rapid *in situ* ^{238}U-^{230}Th dating method.

The measured $^{230}Th/^{238}U$ values for two reference zircons (GJ-1 zircon; PSV zircon) show good agreement with the secular equilibrium value within their analytical uncertainties, demonstrating that the technique is precise and accurate enough for the age determinations. The averaged $^{230}Th/^{238}U$ value of OD-3 zircon is significantly higher than $^{230}Th/^{238}U$ in secular equilibrium while the similar deviation was also reported in Guillong et al. using LA-ICP-SF-MS.[35] Hence this deviation cannot be attributed to the contribution of the mass spectrometric interferences.

To evaluate the reliability of the Quaternary age data, ^{238}U–^{230}Th age determinations by the present technique were conducted on Japanese Quaternary zircon samples from 110 ka to 16 ka (Toya, Sambe Kisuki, Hikageyama, and Susaki Pumice). The resulting ^{238}U–^{230}Th ages of the Quaternary zircon samples were in good agreement with the reported values based on traditional tephra chronologies. The data obtained here demonstrated clearly that the technique developed in this study has a potential to become a rapid and precise analytical tool for the *in situ* analysis of ^{238}U–^{230}Th ages for U–bearing minerals such as zircon.

3.4 High-spatial-resolution elemental imaging technique

In the previous sections, potential sources of analytical errors originating from laser ablation and ionisation processes were rigorously investigated. This is very important to understand why matrix matched-calibration references and reduction of mass spectrometric interference is required to improve the data quality through the LA-ICP-MS analysis. Another important challenge for better analytical results is to minimise the contribution of secondary phases or inclusions and textures with different growth stages. In fact, it is widely recognised that various inclusions containing non-radiogenic Pb are ubiquitously present in zircon, apatite, or titanite samples, and the laser ablation of these secondary minerals/phases can cause systematic error in the measured ages. This can be also true in the case with the U–Th dating method. When analysed areas contain several growth zoning textures, the resulting age is also erroneous. Hence, both the careful positionings of the laser ablation spots and improvement in the spatial resolution of the laser ablation are highly desired. In this section, the advancement of high-spatial-resolution elemental imaging analysis using LA-ICP-MS for obtaining reliable chronological information from mineral samples is discussed.

3.4.1 Introduction

Internal structures of solid materials revealed by spatial distributions of chemical components provide key information of the formation processes among structures (Fig. 3.24). Spatial distributions of chemical components are derived from imaging analysis using *in situ* analytical techniques, and they play an important role in diverse research areas, such as geochemical, environmental, material, and medical sciences.[71, 119)] In the research field of geosciences, elemental imaging analysis of geological samples, such as rocks and minerals, have been essential to visualise internal zoning structures for deciphering the formation processes of the zoning textures in terms of geochemical contexts. Abundance values for some elements are critical to identify difference in chemical compositions of source melts, or transitions of crystallisation temperature and pressure, suggesting that the differences in elemental concentrations and elemental ratios among the zoning textures can indicate the multiple growth stages of mineral formation at different crystallisation conditions and times.[70)] Thus, the imaging data can become a

principal analysis prior to chronological studies based on radiometric dating of minerals to obtain reliable age data with distinct analyses of different zones.

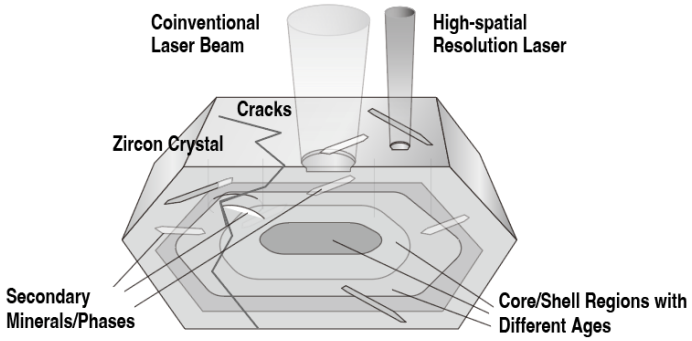

Fig. 3.24 Importance of high-spatial-resolution analysis for geochronology.

Elemental images are generally acquired by electron microscopy (e.g., SEM, or EPMA) or mass spectrometric techniques (e.g., SIMS). In the electron microscope technique, imaging analysis for mineral samples can be conducted with micron to sub-micron spatial resolution by measuring electrons, light, and X-rays, such as secondary electrons, backscattered electrons, and characteristic X-rays emitted from the sample surface scanned by an electron beam.[69, 120)] For the elemental imaging using the SEM technique, elemental analysis is conducted by detecting characteristic X-rays, such as, energy-dispersive X-ray spectroscopy (EDS) and wavelength-dispersive X-ray spectroscopy (WDS). The SEM-WDS analysis is a more sensitive analytical method than SEM-EDS, and the typical values of the detection limits are 10 to 100 μg g^{-1}.[121)] However, a long analysis time is required for acquiring elemental analysis using SEM-WDS (i.e., 10 s for signal integration from one spot analysis), and the imaging analysis using SEM-WDS is practically restricted to line scan analysis rather than two-dimensional analysis.

Another approach for the imaging is based on mass spectrometry coupled with *in situ* sampling techniques. Among *in situ* sampling techniques, laser ablation (LA) is a preferable method for solid materials owing to the high sampling efficiency and high analysis throughput required for high-sensitivity imaging analysis. During the LA process, laser is irradiated on solid materials, and the constituent elements were released from sample surfaces, as described in the section 3.2. An ion source coupled with LA sampling technique requires a large ionisation capacity, and the high-temperature ICP ion source is

a primary option. By taking the advantages in high sampling efficiency and large ionisation capacity, LA-ICP-MS has been utilised for high-throughput and high-sensitivity elemental imaging analysis.[122)]

In isotope geochronology, especially, prior to the age determinations, the cathodoluminescence (CL) imaging has been used for identifying the internal structures of mineral samples. Since the CL intensity depends on various factors, such as accumulation of radiation damage, or concentrations of specific elements,[69)] the difference of the CL intensity provides textual information, which can reflect the distinct zones crystallised at different growth stages, and thus, reliable chronological data can be derived through the CL imaging. Despite the obvious success in identifying the suitable spots for *in situ* age determination using the routinely acquired CL images, understanding the CL images in terms of geochemical contexts for deciphering the detailed formation processes requires the trace-element maps.

Size ranges of the internal structures found in natural zircon crystals are not greater than 10 μm, which is slightly smaller than typical ablation pit sizes achieved by conventional LA-ICP-MS,[71)] suggesting that further high spatial resolution is desired to take a full advantage of the CL analysis. This is one of the fatal drawbacks for LA-ICP-MS against the electron-microscopic technique. Although small ablation pit sizes (e.g., 1μm or smaller) can be produced by an objective lens with the focal length of 10 mm, which is 10-time shorter than the conventional system, the narrowed laser beam is susceptible to laser defocusing due to the short depth of focus (i.e., smaller focusing tolerance), and the defocusing can deteriorate the analytical accuracy, precision and the resulting spatial resolution of imaging analysis. This challenge can be partly solved by the Galvanometric optics. The Galvanometric optics has two rotating mirrors and horizontal and vertical movements of ablation spots are controlled by changing the angle of two mirrors.[123)] This mechanism of laser probing without moving a sample stage eliminates vibrations caused by the stage movement. Since the vibrations can cause defocusing of the 2-micron laser optics with a shallow depth of field (i.e., 1 μm) and this can result in fluctuations in laser sampling efficiency, and the Galvanometric optics without necessity of stage movements is suitable for microanalysis made by laser ablation.

Another challenge is the sensitivity achieved by the LA-ICP-MS. When laser ablation is conducted with smaller ablation pit sizes, amount of sample materials released

from sample surface can become smaller, and thus, higher transmission efficiency from sampling to the mass spectrometer is essential to derive reliable imaging data from trace elements. To overcome this, laser ablation with shorter pulse duration is important. Conventionally, laser ablation systems coupled to ICP-MS systems are based on nanosecond laser, such as Nd:YAG laser and ArF excimer laser. With the nanosecond LA systems, laser induced sample particles being greater than 1 μm are released from the sample surface.[66] The low transmission efficiency of coarse particles from a sample chamber to ICP causes lowering of the useful yield of LA-ICP-MS systems, which is calculated based on the number of ions detected by mass spectrometry per the number of atoms originally containing in sampling volumes. Moreover, insufficient ionisation of coarse particles greater than the critical size of an ICP ion source (e.g., > 1 μm) can also cause of deterioration of both the sensitivity and accuracy of measurements. To avoid this, laser ablation using shorter pulse duration (e.g., femtosecond laser ablation: fsLA) is effective. With the fsLA, effective vaporisation of elements with minimal thermal load onto the sample can be made,[65] resulting in suppression of production of coarse particles being greater than 500 nm,[66] also as shown in Fig. 3.12. The smaller size distribution of the laser-induced sample particles can improve the transport efficiency of the sample particles to the ICP ion source.[66] More importantly, with the smaller size distribution, the elemental fractionation caused by incomplete ionisation of coarse particles can be minimised, while conventional systems can be affected.[75]

In this study, we have developed the in-house two-micron femtosecond laser ablation system with a Galvanometric optics as already described in the section 3.2. The fsLA system is coupled with the sensitivity-enhanced quadrupole-based ICP-MS, which is also used in the section 3.3,[97, 41] for the high-spatial-resolution (i.e., 2 μm) elemental imaging analysis of a mineral sample. The analytical capability of the laser ablation system will be discussed through elemental imaging analysis of zircon, which is the most common mineral used for geochronological studies.

3.4.2 Experimental

3.4.2.1 Instrumentations and system setup

The ICP-MS used in this study was a quadrupole-based ICP-MS (ICP-Q-MS)

equipped with collision cell technology (CCT) (iCAP TQ, Thermo Fisher Scientific, Bremen, Germany). The ICP-Q-MS can monitor a wider mass range with a high-speed mass scanning than sector-field-based ICP-MS (ICP-SF-MS). The limited mass ranges of ICP-SF-MS monitored in a short time period (i.e. 1 s) make it difficult to analyse multiple elements, such as lanthanides, Th, and U, especially useful for clarifying internal chemical zonings of mineral samples to understand the formation history.[70)]

Another advantage of the ICP-Q-MS system is higher compatibility of the collision cell technology. This is because of the lower ion energy employed in the ICP-Q-MS. The ion energy (i.e., ion acceleration voltages) employed in the ICP-SF-MS is > 6 keV, which is much higher than the chemical bindings (e.g., about 10 eV for C–H and N–H bonds), and thus, deceleration of ions is essential to achieve effective collision/reactions within the cell. In contrast, the ion energy adopted in the ICP-Q-MS is about 10 eV which is almost comparable to ion energy for the collision/reactions. In this study, a kinetic energy discrimination (KED) using helium as a collision gas is utilised for removing polyatomic interference ions and thermalisation of ion beams.[94)]

Further improvements of the sensitivity through the ICP-MS system are important for detecting trace elements with the laser ablation using smaller laser pit sizes. In fact, typical sampling volume achieved by the 2 μm pit sizes is almost x1/25 smaller than that obtained by conventional laser ablation. In this study, the threefold-higher ion transmission through the vacuum interface region was achieved by adopting the sensitivity-enhanced dry plasma cone compared to a conventional sampling cone.[97)] The resulting overall useful yield of the LA-ICP-MS system was ca. 0.1% for ^{238}U as well as the system setup used in the section 3.3.

The high-magnification objective lens coupled to a Yb:KGW femtosecond laser and the Galvanometric scanner for raster scanning of ablated spots enabled us the laser ablation with 2 μm pit sizes.[123, 98)] To compare the improvement in spatial resolution achieved by the present technique to a conventional system setup, imaging analysis using a conventional 12-micron-spot femtosecond LA (fsLA) system (Jupiter Solid Nebulizer; ST Japan, Tokyo, Japan) was also conducted.

At the present time, the combination of the 2-micron fsLA system and the ICP-Q-MS system is optimal for elemental imaging analysis. Table 3.3 summarises the analytical conditions of the fsLA systems, and the ICP-Q-MS system used for this study.

The laser ablation chamber was a single-volume cell and laser sampling was conducted inside the chamber under helium gas with the gas flow rate of 0.6 L min^{-1}. The ablated aerosols were transported to the ICP by the helium gas flow and the argon make-up gas flow with the flow rate of 1.0 L min^{-1} added outside the sample chamber. These gas flow rates were tuned to maximise the resulting sensitivity while supressing the production rate of ThO^+/Th^+ to less than 1%.

In this study, data quality of elemental imaging analysis utilising the in-house 2 micron-resolution femtosecond laser ablation (fsLA) system coupled to an ICP-MS system was evaluated through the measurements of a reference zircon (Nancy 91500 zircon)[99] and a zircon sample (Ashizuri zircon) demonstrating complex internal structures reflecting the formation process of an A-type granitoid occurring in the relevant area potentially derived from a source melt produced through partial melting events.[124]

For the imaging analysis using the ablation pit size of 2 μm, the in-house micron-resolution femtosecond laser ablation system (Fab Instruments, Tokyo, Japan) was used. Figure 3.25 illustrates the schematic diagram of the micron-resolution fsLA system. The Galvanometric optics is used for laser ablation of wider sampling are without movements of sample stages, resulting in smaller risk of laser defocusing. The ablated spots moved at 1 μm s^{-1} in the X-axis for a width of 80 μm and 85 μm, and the line spacing for the Y-axis was 2 μm and 12 μm, in the case of the 2-micron fsLA system and the 12-micron LA system, respectively. The repletion rate was 5 Hz, and the averaged fluence was about 4 J cm^{-2} for both the systems. The schematic diagram for the principles of imaging analysis based on LA-ICP-MS is shown in Fig. 3.26.

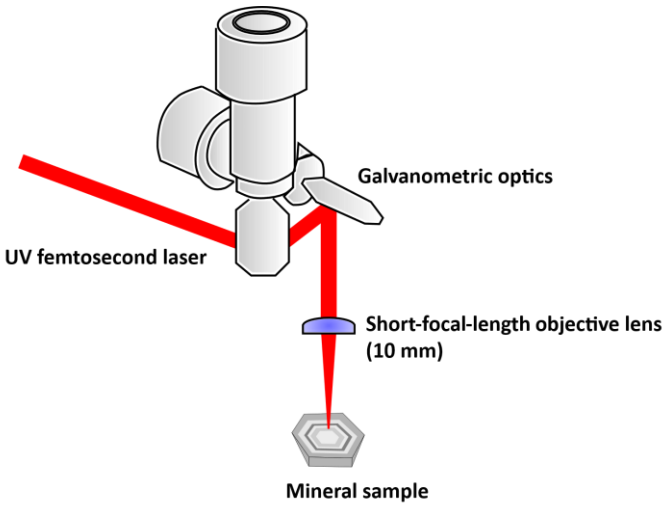

Figure 3.25 Schematic diagram of the developed micron-resolution femtosecond laser ablation system.

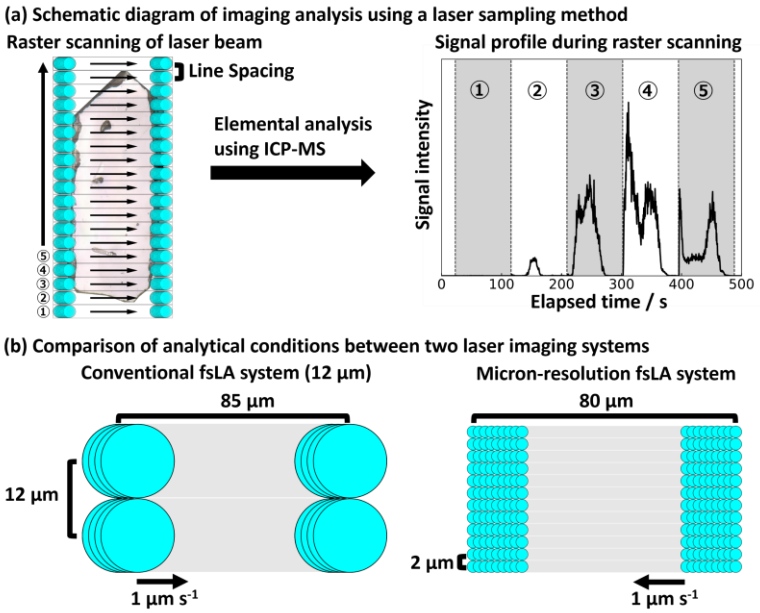

Figure 3.26 Schematic diagrams of imaging analysis using laser sampling technique. Principle of imaging analysis using a laser sampling technique is shown in (a). The analytical conditions of the femtosecond laser ablation system are compared to those of the conventional femtosecond laser ablation system shown in (b).

Table. 3.3 Instrumentation and operational settings of imaging analysis using laser systems (a, b) and ICP-MS system (c).

(a) Micron-resolution fsLA system	
Laser ablation system	In-house 2-micron fsLA system (Fab Instruments, Tokyo, Japan)
Laser spot size	2 μm
Fluence	ca. 4 J cm^{-2}
Repetition rate	5 Hz
He carrier gas	0.6 L min^{-1}
Ar make-up gas flow	1.0 L min^{-1}
Scan speed	1 μm s^{-1}
Sampling area	80 μm×200 $μm^2$
Line spacing	2 μm
Number of scan lines	Total 91 lines (36, 26, and 29 lines were separately analysed)
Required time for imaging analysis	ca. 3 h
(b) Conventional fsLA system	
Laser ablation system	Jupiter Solid Nebulizer (ST Japan Inc., Tokyo, Japan)
Laser spot size	12 μm
Fluence	ca. 4 J cm^{-2}
Repetition rate	5 Hz
He carrier gas	0.6 L min^{-1}
Ar make-up gas flow	1.0 L min^{-1}
Sampling area	85×200 $μm^2$
Scan speed	1 μm s^{-1}
Line spacing	12 μm
Required time for imaging analysis	ca. 30 min

(c) Quadrupole-based ICP-MS	
Instrument	iCAP TQ ICP-MS (Thermo Fisher Scientific, Bremen, Germany)
Sample introduction	Ablated aerosol
RF power	1550 W
Coolant gas flow	14 L min^{-1}
Auxiliary gas flow	0.8 L min^{-1}
Detection system	Secondary electron multiplier
Monitored isotope	^{90}Zr, ^{139}La, ^{146}Nd, ^{157}Gd, ^{172}Yb, ^{178}Hf, ^{232}Th, and ^{238}U for (a) ^{96}Zr, ^{139}La, ^{146}Nd, ^{157}Gd, ^{172}Yb, ^{178}Hf, ^{232}Th, and ^{238}U for (b)
Dwell time	0.05 s for each analyte
Collision/reaction cell mode	KED mode using He
Collision gas flow (He)	4.0 ml min^{-1}

Due to the limitation of analysed areas observed by an optical microscope equipped with the 2-micron fsLA system, imaging analysis was conducted on three separated areas of the single Ashizuri zircon (Fig. 3.27). The elemental mapping data were acquired by repeated line profiling analysis using the rastering rate of 1 μm s^{-1}. Number of analysis lines are 36 for first block, 26 for second block, and 29 for third block. Total analysis time for imaging analysis was about 3 hours.

The monitored isotopes were ^{90}Zr, ^{139}La, ^{146}Nd, ^{157}Gd, ^{172}Yb, ^{178}Hf, ^{232}Th, and ^{238}U. In the case of the 12-micron LA system, ^{96}Zr was analysed instead of ^{90}Zr to avoid

a potential systematic error derived from cross-calibration of analogue and pulse-counting modes in the secondary electron multiplier (SEM) and damage on the SEM since the signal intensity of ^{90}Zr was higher than 10^7 counts per second (cps) during imaging analysis of zircon with the 12-micron resolution.

3.4.2.2 Reference materials and the measured zircon sample

Reference materials measured in this study was a glass reference standard (NIST SRM 610)[87] and the Nancy 91500 reference zircon characterised by Wiedenbeck and their co-workers.[99, 125] NIST SRM 610 was used as a reference used for calibration of elemental concentrations and the Nancy 91500 zircon was used as secondary reference for evaluation of analytical accuracy and precision of quantitative elemental imaging analysis using LA-ICP-MS.

The zircon sample measured in this study was a zircon grain separated from heavy mineral sand occurring in Ashizuri, Kochi prefecture, Japan. The heavy mineral sand contains ilmenite, magnetite, quartz, zircon and a minor amount of uranothorite.[126] Zircon and uranothorite are also observed from the A-type granitoid occurring in the relevant area,[124, 127] and thus, these minerals in the heavy mineral sand originates the granitoid.

The optical microscopic images before and after the elemental imaging analysis using the 2-micron fsLA system are shown in Fig. 3.27. The three-separate analysed areas are also shown in Fig 3.27(b). After the 2-micron imaging analysis, the sample surface was polished, and then, imaging analysis using the 12-micron fsLA system was conducted. Subsequently, electron-microscopic analysis was conducted for the analysed Ashizuri zircon sample. From the SEM-EDS analysis, apatite was observed as an inclusion mineral inside the zircon sample.

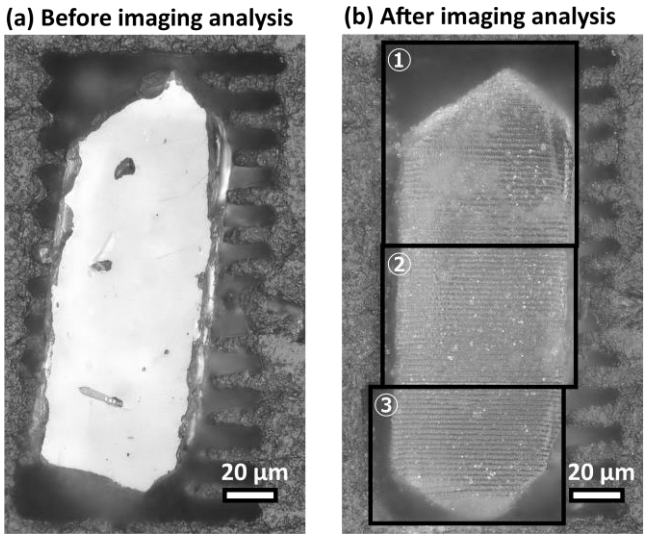

Figure 3.27 Optical images of the analysed zircon sample. (a) and (b) represent the photographs taken before and after the imaging analysis, respectively.

3.4.2.3 Data reductions

Visualisation of the time-resolved data obtained from imaging analysis of zircon was conducted using a data processing software of iQuant2+.[128] With the iQuant2+ software, the time-resolved data was separated for each scanned line, and the segmented data was reconstructed into false-colour elemental mapping images on the *X*-*Y* plane. Then, since the imaging analysis by the 2-micron fsLA system was carried out for approximately one-third of the whole Ashizuri zircon grain per one-time measurement, three separate images were obtained. These images were aligned and joined together by using an image shape correction module included in the iQuant2+ software.

For the calibration of elemental concentration, firstly, averaged gas blank signal intensity of each isotope for 5 second measurements before analysis were subtracted from the signal intensity during laser ablation. After the blank subtraction, the signal intensity of ^{139}La, ^{146}Nd, ^{157}Gd, ^{172}Yb, ^{178}Hf, ^{232}Th, and ^{238}U was normalised by the signal intensity of ^{90}Zr as an internal standard element. Then, based on the equation (3.4), the calibration factors of each element were calculated by dividing the reference value of elemental concentration by the normalised signal intensity of the NIST SRM 610. Finally, the

elemental concentration of the sample was calculated by the multiplication of the obtained correction factor, the normalised signal intensity of each analyte, and the Zr concentration of zircon based on the equation (3.5). In this study, Zr concentration of zircon is assumed to be the constant value of 4.98×10^5 μg g^{-1} reckoned by the atomic mass of Zr and stoichiometry of $ZrSiO_4$.

$$F_i = \frac{\left(\frac{C_i^{\text{NIST SRM 610}}}{C_{\text{Zr}}^{\text{NIST SRM 610}}}\right)}{\left(\frac{I_i^{\text{NIST SRM 610}}}{I_{\text{Zr}}^{\text{NIST SRM 610}}}\right)} \tag{3.6}$$

$$C_i^{\text{Zircon}} = \frac{I_i^{\text{Zircon}}}{I_{\text{Zr}}^{\text{Zircon}}} \times F_i \times C_{\text{Zr}}^{\text{Zircon}} \tag{3.7}$$

where $C_i^{\text{NIST SRM 610}}$ is the concentration of an element (i = La, Nd, Gd, Yb, Hf, Th and U) in NIST SRM 610, $C_{\text{Zr}}^{\text{NIST SRM 610}}$ is the concentration of Zr in NIST SRM 610, $I_i^{\text{NIST SRM 610}}$ is the signal intensity of an element (i = La, Nd, Gd, Yb, Hf, Th and U) for NIST SRM 610, and $I_{\text{Zr}}^{\text{NIST SRM 610}}$ is the signal intensity of Zr for NIST SRM 610, C_i^{Zircon} is the concentration of an element (i = La, Nd, Gd, Yb, Hf, Th and U) in zircon, $C_{\text{Zr}}^{\text{Zircon}}$ is the concentration of Zr in zircon, I_i^{Zircon} is the signal intensity of an element (i = La, Nd, Gd, Yb, Hf, Th and U) for zircon, and $I_{\text{Zr}}^{\text{Zircon}}$ is the signal intensity of Zr for zircon, and F_i is the correction factor of i.

The elemental concentration of NIST SRM 610 used in this study was the preferred value reported in Jochum et al.[87] and the Zr concentration of zircon ($C_{\text{Zr}}^{\text{Zircon}}$) used this study is 4.98×10^5 μg g^{-1}. The correction of the elemental concentration based on the normalisation of the signal intensity by Zr was carried out on the analysed area with the higher signal intensity than the laser blank signal intensity during laser ablation of the resin. Then, the elemental concentration map was also visualised by using the iQuant 2+ software.

3.4.3 Results and discussion

3.4.3.1 Analytical capability of the micron-resolution LA system

The resulting elemental sensitivity achieved by the present LA system developed here was about 8 cps/μg g^{-1} calculated from the U signal intensity of NIST SRM 610

during raster scanning with the rate of 1 μm s^{-1}. For the accurate analysis of trace elements, high signal-to-background ratios of analytes are required, and a gas blank level without sample introduction should be suppressed to zero. The gas blank is mainly composed of Ar-based polyatomic ions (e.g., ArO^+) derived from the Ar-ICP ion source, and therefore, in terms of reducing the gas blank, collision cell techniques are important. In this study, analytes are lanthanides, Th, and U, and the gas blank of them is low (i.e., 0–15 cps) due to reduced contamination of these elements in the fsLA-ICP-MS system and small contributions of Ar-based polyatomic ions in the relevant mass range. This is important to quantitatively measure a trave level of them with concentration of 1–10 μg g^{-1}.

The averaged abundance values of the Nancy 91500 zircon were calculated from the four analyses before and after three-time imaging analysis of the Ashizuri zircon sample. The resulting concentration values for the analytes except for La are plotting against the reference values in Fig. 3.28. Due to exceptionally low content of La, (0.006 μg g^{-1}),[125)] ^{139}La could not be detected by the present technique, and thus, data point for La is not plotted on Fig. 3.28.

For Yb, Hf, Th, and U whose concentrations are higher than 10 μg g^{-1}, the obtained values in this study deviate from the reference values by 10–30% beyond the range of uncertainty. This systematic error is partly derived from the heterogeneity of the Nancy 91500 zircon depending on provided fractions. The relative standard deviation (2RSD) accompanied with the reference values of elemental concentrations ranges from 10% to 30%, and this is comparative to the difference between the obtained values and the reference values. Another cause of the systematic error originates the calibration of elemental concentrations using the non-matrix-matched reference (the NIST SRM 610 glass). Generally, a systematic error (i.e., 10%) can be derived from the non-matrix-matched calibration for elemental analysis using LA-ICP-MS as mentioned in the section 3.2. For further improvement in analytical accuracy, another well-characterised matrix-matched reference material is necessary.

For the minor elements containing in the Nancy 91500 zircon (Gd and Nd), the poor analytical accuracy and precision were demonstrated. Although the obtained Gd concentration agreed well with the reference value within analytical uncertainty, the uncertainty expressed as two RSD exceeds 100%. The Nd concentration significantly deviates from the reference value. Due to the reduction of sampling volumes utilising the

2-micron LA system, the averaged signal intensities of ^{157}Gd and ^{146}Nd during the analysis of the Nancy 91500 zircon were about 10 counts per second (cps) and about 1 cps, respectively, and thus, the resulting low signal-to-background ratios can deteriorate the analytical accuracy and precision. Additionally, since the sampling depth by the present technique is only a few μm, measurements of minor elements can easily be affected by surface contamination. To improve the data quality of trace-element analysis, imaging analysis should be conducted by further-enhanced sensitivity ICP-MS system. Moreover, removal of surface contamination through a one-shot cleaning protocol would be effective to derive reliable abundance values for trace-elements. [129].

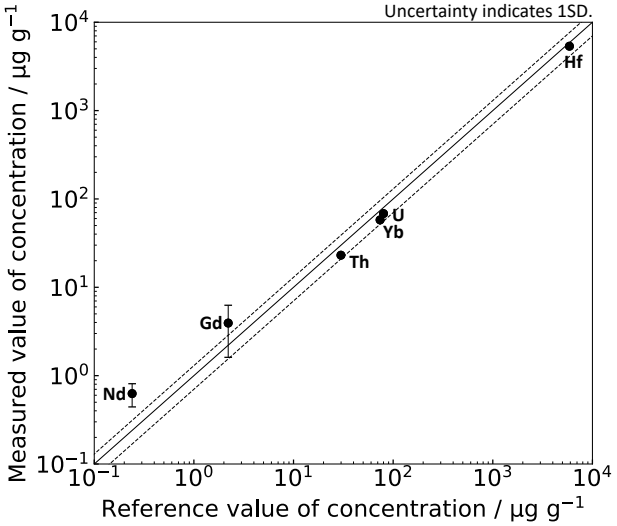

Figure 3.28 Abundances for Nd, Gd, Yb, Hf and U defined in the present micron-resolution fsLA-ICP-MS method plotted against the literature values reported by Wiedenbeck et al. (1995). Data points for six elements fall close to a 1:1 straight line. Dashed lines represent ±30% deviation from the literature values.

3.4.3.2 Visualisation of data obtained from imaging analysis of the Ashizuri zircon

The obtained time-resolved data was converted to the elemental maps by using the iQuant2+ software. Fig. 3.29(a) and (b) are the resulting elemental map based on the signal intensity of each analyte made by the 12-micron LA system and the 2-micron fsLA system, respectively. These figures clearly demonstrate the improvement in spatial resolution of elemental imaging analysis utilising the 2-micron fsLA system. Owing to

the finer line spacing with the 2-micron fsLA system, the spatial resolution of the Y-axis was improved, and this high-resolution imaging allows for obtaining the clear image of the external shape, which is similar to the original shape of the hexagonal zircon.

Despite the same scan speed of 1 μm s^{-1} on the X-axis for the both systems, the magnitude of overlap of the ablation spots exceeded 90% for the conventional 12-micron LA system overlap about 90% with the adjacent ablated spots displaced by 1 μm s^{-1}. Due to the mixing of the adjacent spots, the obtained elemental map was blurred when the conventional LA system with 12-micron pit sizes was employed. Compared to the 12-micron LA system, by using the 2-micron fsLA system, the low mixing ratio of the adjacent ablated spots results in enough high spatial resolution to distinguish the internal zoning of the zircon sample. Based on the variation of Th concentration shown in Fig. 3.30(a), the internal structure of the analysed Ashizuri zircon is distinguished into four zones of (I–IV), while the boundaries among these zones are unclear in the case with the conventional LA system shown in Fig. 3.29(a).

For the zircon grains, various secondary mineral or inclusions can found by the optical microscope observations. Presence of these inclusions or minerals can be visualised by the elemental mapping as the areas with low Zr and Hf contents and high La and Nd signal contents. These light-lanthanide-element-rich inclusions should be phosphates, while zircon has a poor light-lanthanide concentration. One of the major inclusion minerals would be apatite as reflected the high-La and Nd contents. Moreover, presence of the secondary inclusions will be identified by the isotopic signature of Pb. Since the U is compatible to zircon, the most of old zircons contain high radiogenic Pb (^{206}Pb), whereas the monazite which exhibiting high-Th can contain ^{208}Pb, and thus, both the elemental and isotopic mapping can become important chemical information for the identification of secondary inclusions. For the precise isotopic mapping, however, imaging analysis using the multiple-collector mass spectrometer is essential.

Based on the elemental map of Zr and Hf converted from the raw signal count rates of analytes, the shading of the elemental concentration was observed, especially at the boundary of three separate maps. Since the zircon should have the homogenous Zr content, this spatial heterogeneity observed by the 2-micron fsLA imaging should be an analytical artifact. This artifact is potentially due to the different sampling efficiency depending on the ablated spots. Because of the narrow Rayleigh length, the sampling

efficiency by laser irradiation varies depending on the difference in depth of focus, the smoothness and flatness of the sample surface, and a potential instrumental drift causing the defocusing of the laser beam.

With the measured ion counts for analytes, abundance values for the analytes can be calculated. For the calibration of elemental abundances, the signal intensities of analytes were basically normalised by the signal intensity of Zr, and this calculation can correct the difference in sampling efficiency depending on the ablated spots. The quantified elemental concentration map is shown in Fig. 3.29(c). The calibration to concentrations was performed on the areas with higher signal intensity of ^{90}Zr than the laser blank during laser irradiation on the sample-embedded resin.

Although Hf concentration has a smaller difference within the sample than concentrations of other elements, and the internal zonation of Hf should be vague without the correction of ablation volumes. After normalising the signal intensity based on the signal intensity of ^{90}Zr, the core–rim structure with low Hf concentration in the core and high Hf concentration in the rim is more clearly observed.

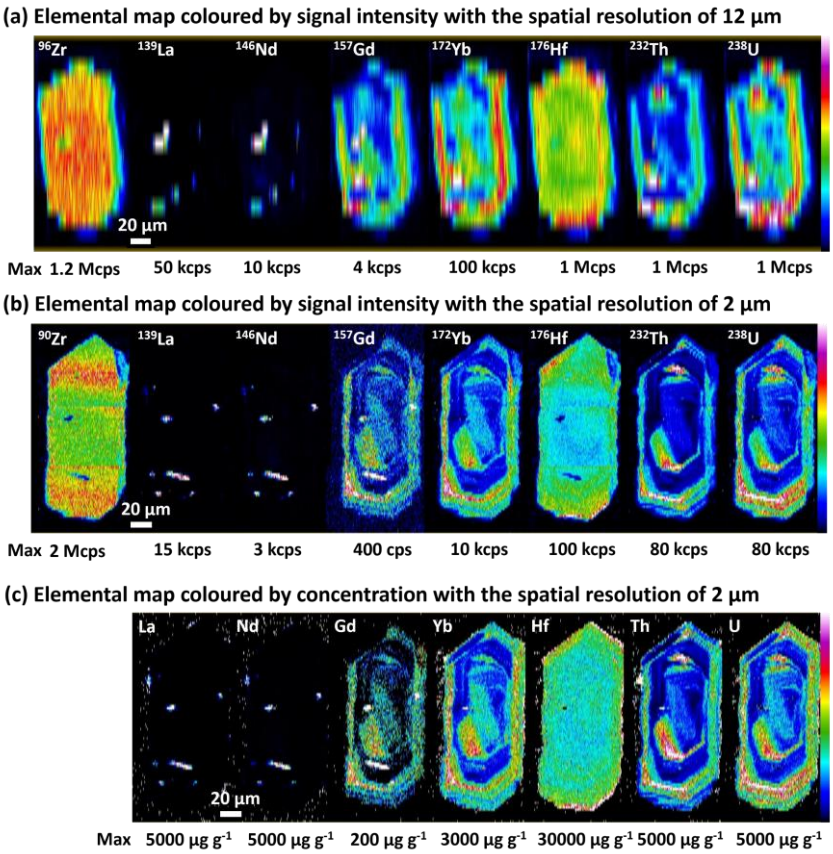

Figure 3.29 Elemental maps obtained from imaging analysis of the Ashizuri zircon. (a) Elemental map obtained with the conventional 12-micron fsLA system is coloured by elemental signal intensity. (b, c) Elemental maps obtained with the micron-resolution fsLA system are coloured by elemental signal intensity and elemental concentration, respectively. The maximum values denoted in the elemental maps correspond to the upper end of the colour bars for each element. The lower ends of the colour bars are zero. Each scale bar indicates 20 µm.

3.4.3.3 Correlation analysis of elemental abundances

Concentration ratios among specific elements, such as lanthanides (Ln), U, and Th, can reflect the chemical compositions of source melts and mineral paragenesis at the timing of crystallisation. Especially for the felsic rocks, Ln, U, and Th budgets are basically controlled by heavy minerals, such as apatite, monazite, and zircon. Hence, the crystallisation of these minerals from source melts can change the elemental ratios of source melts, and the distribution coefficients of these elements also vary depending on the presence or absence of the heavy minerals as co-existing phases.[130, 131, 70)]

In this study, the correlation between U and Th is utilised for distinguishing the internal chemical structure. Although both the U and Th are compatible elements of zircon, zircon has a higher distribution coefficient ratio values (i.e., U/Th being almost 5),[132)] and thus, fractional crystallisation of zircon can result in lowering of the U/Th values of the source melt. In contrast, phosphates, including apatite and monazite, have a smaller partition coefficient ratio (i.e., U/Th being lower than unity),[40, 133)] and thus, U/Th of zircon with coexisting phosphates during melt differentiation can increase owing to the removal of Th from the source melt by fractional crystallisation of Th-enriched phosphates or increase of the partition coefficient ratio of U/Th between zircon and the source melt under the coexistence of phosphates.

In Fig. 3.30(b), the U concentration of each data point from four zones (I–IV) is plotted on the Y-axis against the X-axis of the Th concentration. From zone (I) to zone (II), and from zone (III) to zone (IV), U and Th concentration are higher at the outer portion potentially due to enrichment of incompatible elements including U and Th with the melt differentiation. Based on the clear correlation between U and Th concentrations, these zones can be classified into two groups as low-U/Th core for (I) and (II), and high-U/Th rim for (III) and (IV). This is attributable to crystallisation of the zircon rim under the coexistence of phosphates, such as apatite and monazite. Apatite was observed as inclusion minerals in the zones (III) and (IV), and the presence of apatite in the rim is consistent with the higher U/Th of the rim than that of the core. To conclude the formation history, phosphate saturation in the source melt occurred after the core growth, and the subsequent rim formation proceeded in the presence of phosphate minerals with the high U/Th of the zircon rim.

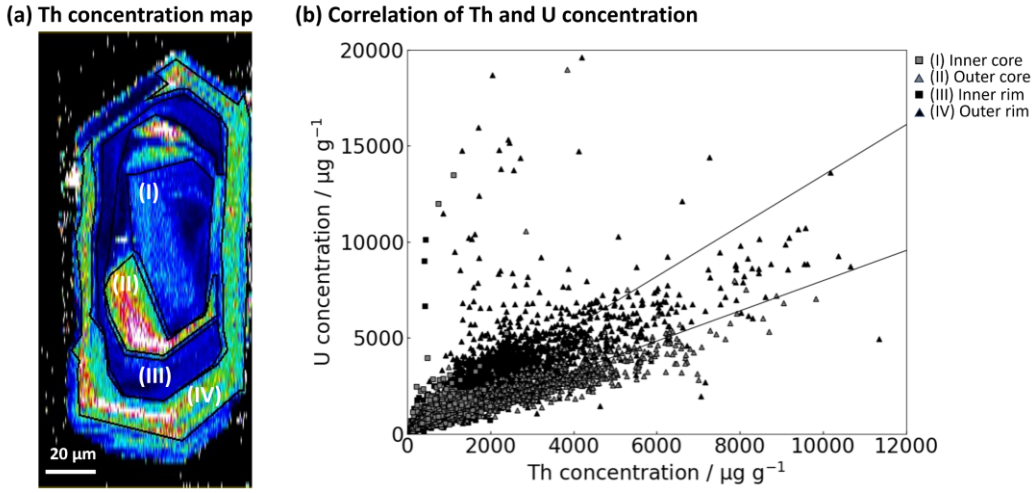

Figure 3.30 Correlation of Th and U concentration for the outer core, inner core, outer rim, and inner rim of the Ashizuri zircon. (a) Th concentration map of the Ashizuri zircon is shown to distinguish the internal structure of (I) Inner core, (II) Outer core, (III) Inner rim, and (IV) Outer rim. (b) The U concentration of data points for each zone is plotting on the Y-axis against the X-axis of Th concentration. The upper straight line is the regression line calculated from the data points of the outer rim, and the lower straight line is that of the inner rim.

Conventionally, preliminary analysis for careful selection of analysis spots before U–Pb and U–Th age determinations on zircon is merely dependent on luminescence intensities of CL images with less geochemical information. In contrast, with the elemental mapping images instead of CL images, the difference of multiple growth stages can be reasonably distinguished, and the detailed formation processes of minerals can be deduced. This is important in geochronological studies. The remaining challenge with the present imaging technique using fsLA-ICP-MS is to increase sample throughput. Although the present technique is one order of magnitude faster than SEM-WDS analysis, CL images can be derived within a few second. Significant efforts should be given to improve the analysis speed for superseding the CL method and advancing geochronological researches.

3.4.4 Conclusion

The main conclusion of this section is that both the high-spatial resolution imaging and elemental correlation analysis can be made by the LA-ICP-MS technique. Although elemental/isotopic analysis using smaller ablation pit sizes can cause poorer elemental sensitivity of the LA-ICP-MS, data quality can become rather better because of smaller magnitude of contribution of secondary phases/minerals. This is very important for the geochronological studies. The following is the three findings obtained in this chapter.

1. In this study, a femtosecond laser ablation (fsLA) system with 2-micron spot size was newly developed and, the spatial resolution of elemental maps obtained by fsLA-ICP-MS is improved. The improved spatial resolution can be utilised for elemental imaging analysis to distinguish the internal zoning textures of minerals.

2. By the present technique of fsLA-ICP-MS, trace elements of more than 10 $\mu g\ g^{-1}$ are quantitatively analysed with 2-micron spatial resolution, and the resulting sensitivity is more than ten-times higher than electron-microscopic techniques. The analysis throughput achieved by the present fsLA-ICP-MS method is almost one order of magnitude higher than that required in the SEM-WDS analysis. Compared with the CL imaging, further high-speed analysis using fsLA-ICP-MS is desired.

3. The present technique was applied to elemental imaging analysis of the zircon sample from Ashizuri. By analysing the correlation of U and Th concentrations in the obtained elemental map, four zones were classified into the core and rim structure of zircon.

Based on the data presented in this section, a realistic conclusion is that the LA-ICP-MS has immediate potential as a principal choice for both the imaging and correlation analyses for various mineral samples. The technique with increasingly improved instrumentations will, in the future, produce geochemical and geochronological data comparable or rather better to SIMS or EPMA techniques.

Chapter 4
Geochronological application

The fire at Lipara, Xenophanes says, ceased once for sixteen years, and came back in the seventeenth. And he says that the lava stream from Aetna is neither of the nature of fire, nor is it continuous, but it appears at intervals of many years.

This comes from De mirabilibus auscultationibus (On Marvellous Things Heard),[134)] a text written by Greek philosophers that was once believed to be the work of Aristotle. Since ancient times, volcanic eruptions have been a subject of human interest, with philosophers speculating about the sporadic nature of volcanic activities and striving to decode the mysteries. Today, we have analytical tools for deciphering the chronological sequence of igneous activities.

In Chapter 3, studies on analytical issues related to LA-ICP-MS is discussed, and specifically, methods for interference removal in ^{238}U–^{230}Th isotope analysis and high-spatial-resolution imaging mass spectrometry technique were developed for reliable ^{238}U–^{230}Th age determination. In Chapter 4, for the geochronological application of the developed techniques, the ^{238}U–^{230}Th dating of zircon from a Holocene rhyolite is conducted.

4.1 Introduction to magmatism in intra-oceanic arc systems

Intra-oceanic convergent margins are an important tectonic setting for generation of magma caused by the subduction of oceanic plates, and investigation on volcanoes located in the intra-oceanic arc systems is critical for understanding the time evolution of magmatism including generation, exhumation, storage, differentiation, assimilation, and eruption of magma. The detailed understanding of modern magmatism in intra-oceanic arc systems is also essential for elucidating crustal growth through the Earth's history.[135] Among the intra-oceanic arc systems, the Izu–Bonin arc located between the Pacific plate and the Philippine Sea plate is one of the well-studied regions as a representative of the intra-oceanic arc systems through previous geological, geochemical, and geophysical research.

The Izu–Bonin arc is characterised by igneous activities with bimodal compositions of mafic and felsic volcanic rocks. Based on the previous geochemical study, the mechanism for generation of felsic magma is not partial melting of basaltic rocks and subsequent fractionation, but partial melting of the underlying andesitic middle crust.[136] According to geophysical research, the spatial distribution of the rhyolite-dominant volcanoes is prominent in areas where the middle crust is thin,[137] and basaltic magma can be intruded. From these geochemical and geophysical studies, production of felsic magma is primarily controlled through partial melting of the andesitic middle crust caused by heating due to the intrusion of basaltic magma.[138]

For tracing the temporal evolution of intermittent magmatic activities of felsic volcanoes, volcanic islands with dominant rhyolite exposed above the sea level are appropriate because of the clear history of eruptive events based on stratigraphy defined by detailed geological survey. In the Izu–Bonin arc, those volcanic islands with rhyolite lavas are linearly distributed on the rear-arc side, such as Niijima and Kozushima

belonging to the Zenisu ridge (Fig. 4.1). Based on the previous geochemical and petrological research on the relevant areas, a two-stage eruption model is proposed; I. mixing of basaltic and rhyolitic magmas at the middle to lower crust and production of andesitic magma, and II. mingling of andesitic magma with rhyolitic magma at shallower regions, causing eruptions.[139] Age determinations of phenocryst minerals like zircon should provide key chronological information of the remelting and recrystallization within the magma reservoir associated with intermittent injections of andesitic magma. Therefore, detailed chronological studies are required.

Through the investigation on volcanic activities in Kozushima, tracking the temporal evolution of felsic igneous activity over a million years is achievable. The basal unit of Kozushima is comprised of orthopyroxene- and hornblende-bearing dacite, and the reported zircon U–Pb age of the dacite is 0.934 ± 0.026 Ma.[140] Since then, volcanic activities continue in the relevant area. There are at least sixteen volcanoes on Kozushima, and these can be classified into several older stages and the younger stage based on stratigraphy.[141] Lavas from the older stages show the variation in lithology, such as biotite rhyolite, cummingtonite-bearing rhyolite, and orthopyroxene-bearing rhyolites, while lavas from the younger stage are mostly biotite rhyolite. Recent studies revealed the eruption timings of the volcanoes based on thermochronological methods and the radiocarbon dating method, and the younger stage began after ca. 30ka.[142, 143] The volcanic activity after 30 ka continued until around 19 ka, with eruptions occurring at locations such as Matsuyamabana, Osawa, and Jyogo-yama etc, and then, setting aside minor eruptions (e.g., Kozushima-Chichibuyama-A'), the more recent volcanic activity includes eruptions in the northern volcanic chain (Kobe-yama, Anano-yama, and Hanatate) after 3 ka, culminating in the most recent eruption at Mt. Tenjo at 1.2 ka.[142, 143, 144]

The volcanic activity in Mt. Tenjo is the latest eruption in the Zenisu ridge, and Mt. Tenjo is suitable for elucidation of rhyolitic magmatic activity with a high temporal resolution of ^{238}U–^{230}Th chronology. For a rhyolite occurring in Mt. Tenjo, the ^{238}U–^{230}Th age was previously reported based on two-point isochron composed of the bulk data of glass and zircon fractions. The resulting age is 11 ± 2 ka, and this is significantly older than the eruption timing of 1.2 ka shown in Fig. 4.3.[145] The previous study suggested that the ^{238}U–^{230}Th age corresponds to the crystallisation age of zircon, and the time duration

between the zircon crystallisation timing and the eruption timing constrains a lower limit of lifetime for magma in the relevant area. However, zircon grains have internal growth textures, and bulk analysis of zircon fractions with more than 50 mg essentially yields averaged chronological data of different growth stages. Faced with this problem, the developed techniques of the imaging mass spectrometry for trace elements and the *in situ* ^{238}U–^{230}Th dating method were applied to individual zircon grains separated from the rhyolite to resolve magmatic processes recorded in the zircon textures.

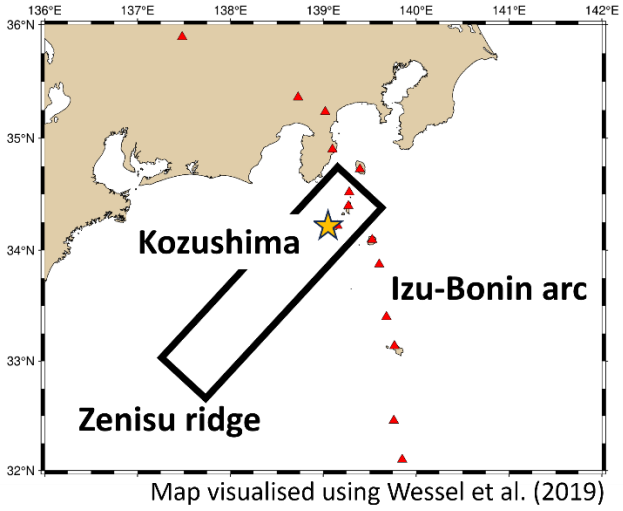

Figure. 4.1 Map showing the location of Izu–Bonin arc, Zrnisu ridge, and Kozushima visualised using a software by Wessel et al. (2019).[146)]

4.2 Experimental

4.2.1 Sample preparation of zircon

A heavy mineral fraction containing zircon was obtained from the rhyolite sample collected from Mt. Tenjo in Kozushima after the protocols of crushing, panning in water, magnetic separation, and heavy liquid separation. Subsequently, the zircon grains contained in the heavy mineral fraction were mounted in a PFA sheet and polished using waterproof abrasive sheets to expose the interior of the samples.

4.2.2 Experimental conditions of trace-element imaging analysis

The analysis protocol basically follows the methodology discussed in the section 3.4 with minor changes. The laser probing conditions were the repetition rate of 5 Hz, the fluence of 4 J cm^{-2}, and the raster scan speed was 2 μm s^{-1}, and the flow rates for the

carrier and make-up gas of the LA system were 0.6 L min^{-1} for He, and 1.05 L min^{-1} for Ar. For the enhancement of the ion transmission through the vacuum interface of the ICP-MS, the sensitivity-enhanced dry sampling cone was adopted. The analysed isotopes were ^{88}Sr, ^{90}Zr, ^{139}La, ^{140}Ce, ^{146}Nd, ^{157}Gd, ^{172}Yb, ^{178}Hf, ^{232}Th, and ^{238}U. Prior to the imaging analysis, the CL observations were conducted.

4.2.3 Experimental conditions of ^{238}U–^{230}Th age determination

The analysis protocol basically follows the methodology using fsLA-ICP-MS described in the chapter 3.3 with minor changes. The data acquisition was conducted for ^{29}Si, ^{44}Ca, ^{230}Th, ^{232}Th, ^{235}U, and ^{238}U. The repetition of laser was 100 Hz, and the sampling volume was 25 x 30 x 7 μm^3. For two zircon grains (KT1 and KT2) among five zircon grains, the core and rim structures were separately analysed. For the two zircon grains (KT3 and KT5), the age determinations were conducted only to the core region because of the lack in the spatial resolution for analysing thin layers of the rim. For the remaining one zircon (KT4), both the two analysis spots include the mixed areas of the core and rim due to the insufficient spatial resolution, and one also contains the inclusion phase within the analysed area observed by optical microscopy and the ^{44}Ca signal detected during the ^{238}U–^{230}Th isotope analysis. Hence, the data for KT4 is rejected from the age calculation and discussion.

4.3 Results and discussion

4.3.1 Internal zoning textures of zircon

As a general trend based on the observations of the CL images (Fig. 4.2–4.6), the all five zircons have the internal zoning structures of dark core and bright rim, and the dark core and bright rim correspond to the high- and low-concentration areas of incompatible elements, respectively. The CL intensity depends on the multiple factors including radiation damages and trace-element concentrations. The zircons analysed in this study are very young, and the contribution of the radiation damages are minimised. Hence, the difference in the CL brightness is likely to reflect the compositional differences in the internal zoning structures of zircon. Especially, the concentrations of U, Th, and Ce present in magma and zircon crystals as tetra-valent cations, except for Hf, shows clearer difference between the core and rim areas compared to other lanthanide

elements being tri-valent cations. This indicates a strong negative correlation between the concentrations of U, Th, and Ce and the CL intensity. The higher contents of incompatible elements for the rim portions imply the enrichment of them owing to the differentiation or fractionation of magma.

4.3.2 ^{238}U–^{230}Th ages of zircon

In this study, age calculation is conducted based on zircon data and the previously reported glass data. For the core portions of zircon, the resulting zircon core–glass isochron ^{238}U–^{230}Th age is 17 ± 5 ka (1s) (Fig. 4.3). For the data of the rim portions, the zircon rim–glass isochron ^{238}U–^{230}Th age is 5 ± 4 ka (1s) based on the same calculation as the core zones (Fig. 4.7). Despite the remaining large uncertainties, the previously reported ^{238}U–^{230}Th age based on the bulk analysis (ca. 11 ka)[145] is between the ages for the core and rim areas, that is potentially the erroneous mixed chronological data.

The ^{238}U–^{230}Th age of the zircon core is significantly older than the eruption timing of Mt. Tenjo at 1.2 ka and can correspond to the timing of the former eruptive activities during 19–30 ka. Hence, the core should be crystallised inside the magma reservoir during the former eruptive activities (30–19 ka). The ^{238}U–^{230}Th age of the zircon rim potentially being younger than that of the core suggests the following sequence of zircon formation. Firstly, newly generated magma was intruded into the magma reservoir, and solidified portions within the magma reservoir was remolten. Subsequently, During the remelting, zircon crystals with low solubility in magma were not molten,[29] and the crystallisation of the zircon rims occurred using the survived zircons as crystallisation nuclei along with the cooling and solidification. The ^{238}U–^{230}Th age of the zircon rims agrees with the latest volcanic activities in the northern part of Kozushima, and the zircon age potentially corresponds to the timing of melt intrusion triggering the latest volcanic activities.

The notable thing is that zircon from the older eruptive stages or basal rocks is absent. This is attributable to the differences in sources of magma and locations of magma reservoirs, and this is consistent with the lithological differences of rhyolites before and after 30 ka suggesting the possibility that the sources of magma involved in volcanic activities changed. The absence of the older zircons also indicates the generation of magma occurring under conditions without zircon, and limited contribution of the

assimilation of surrounding rocks during exhumation from middle crust and storage in the magma reservoir. Hence, the rhyolitic magma in the relevant area is not likely to be generated by recycling of zircon-bearing felsic crustal rocks. This is in good agreement with the model for generation of felsic magma within the middle crust composed of andesitic rocks.[136, 139)]

4.4 Conclusion

The developed analytical techniques of high-spatial-resolution elemental imaging and *in situ* ^{238}U–^{230}Th dating of zircon using LA-ICP-MS were applied to zircon samples collected from Mt. Tenjo in Kozushima. The two following remarks concludes Chapter. 4.

1. All five zircons analysed in this study demonstrates the clear zoning textures of the CL-bright core and CL-dark rim. There is a negative correlation for the brightness of CL images and the concentrations of incompatible elements, especially elements incorporated into zircon as tetra-valent cations (U, Th, and Ce), and the rim of zircon was likely to be formed from the more fractionated melt compared to the source melt of the core.
2. Despite the large uncertainty accompanied with the ^{238}U–^{230}Th ages, the ages for the zircon core and zircon rim are separately determined based on the observations of the internal textures, and the resulting age for the core and rim can correspond to the former melt injection event (30 ka–19 ka), and the melt injection event related to the latest magmatic activity. The combined approach of elemental mapping and *in situ* ^{238}U–^{230}Th age determination through the developed techniques utilising high-spatial-resolution LA-ICP-MS can be a powerful tool for resolving time differences among magmatic activities.

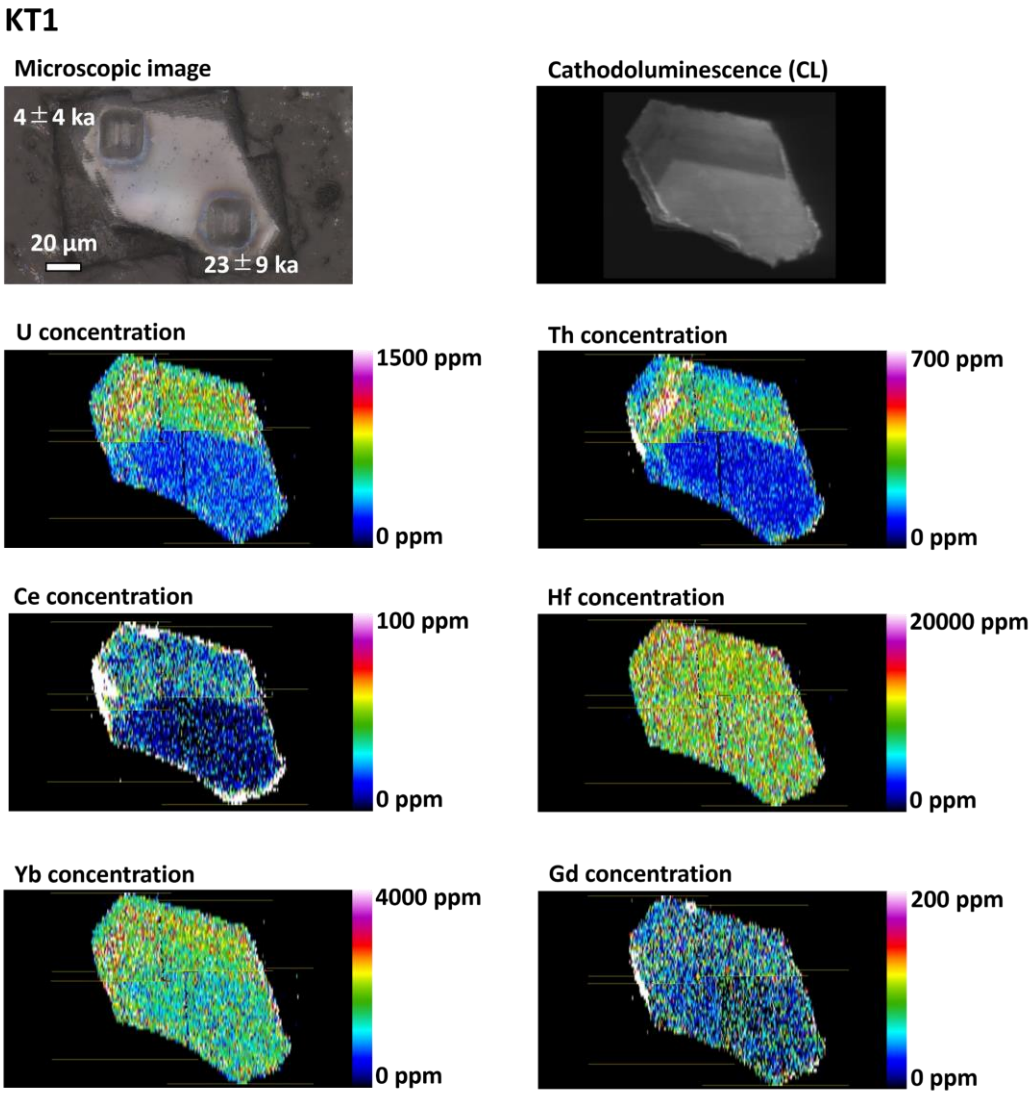

Figure 4.2 Optical microscopic, cathodoluminescence, and trace-element images for the analysed zircon of KT1. The ^{238}U–^{230}Th ages plotted on the optical microscopic images are two-point isochron ages calculated based on the combination with the previously reported data of glass.[140)]

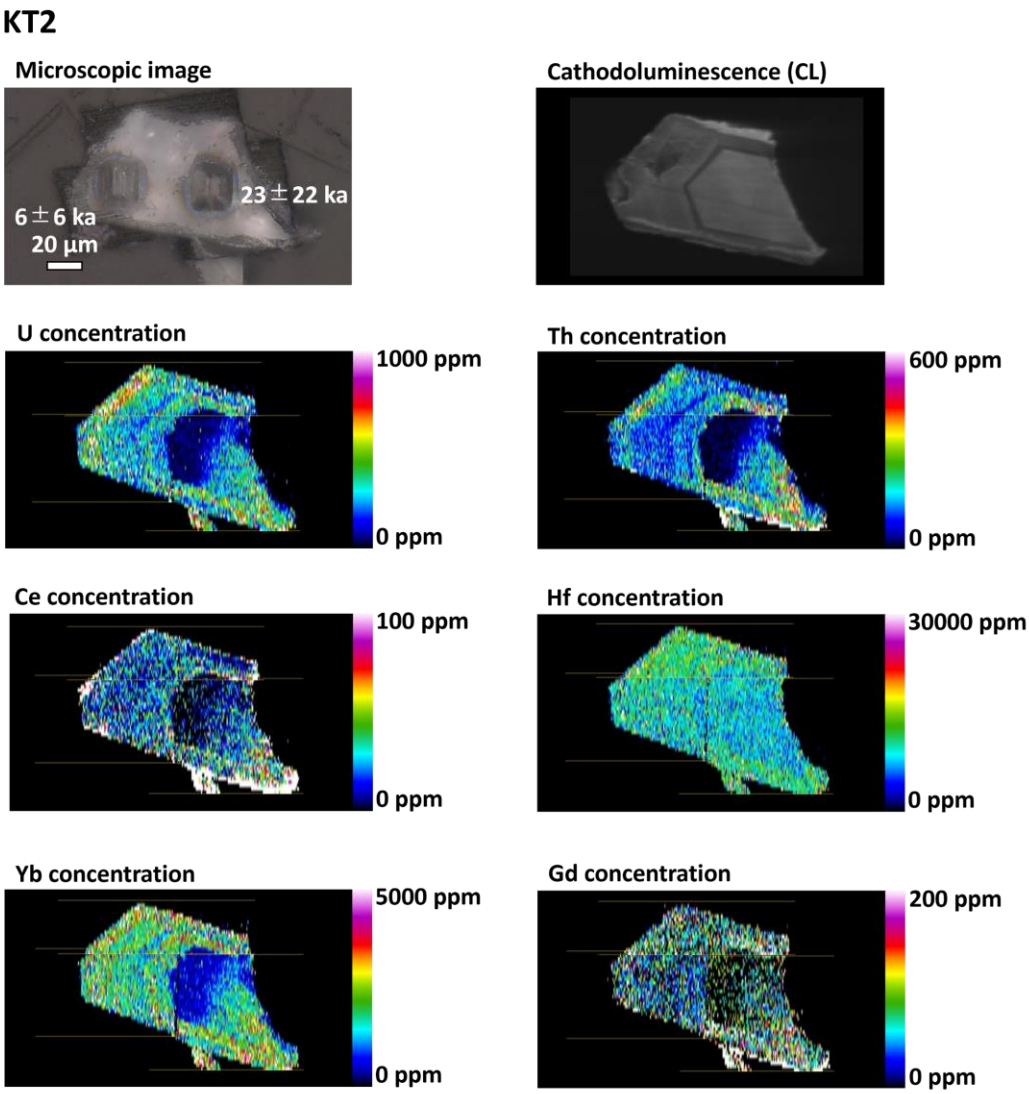

Figure 4.3 Optical microscopic, cathodoluminescence, and trace-element images for the analysed zircon of KT2. The ^{238}U–^{230}Th ages plotted on the optical microscopic images are two-point isochron ages calculated based on the combination with the previously reported data of glass.[140)]

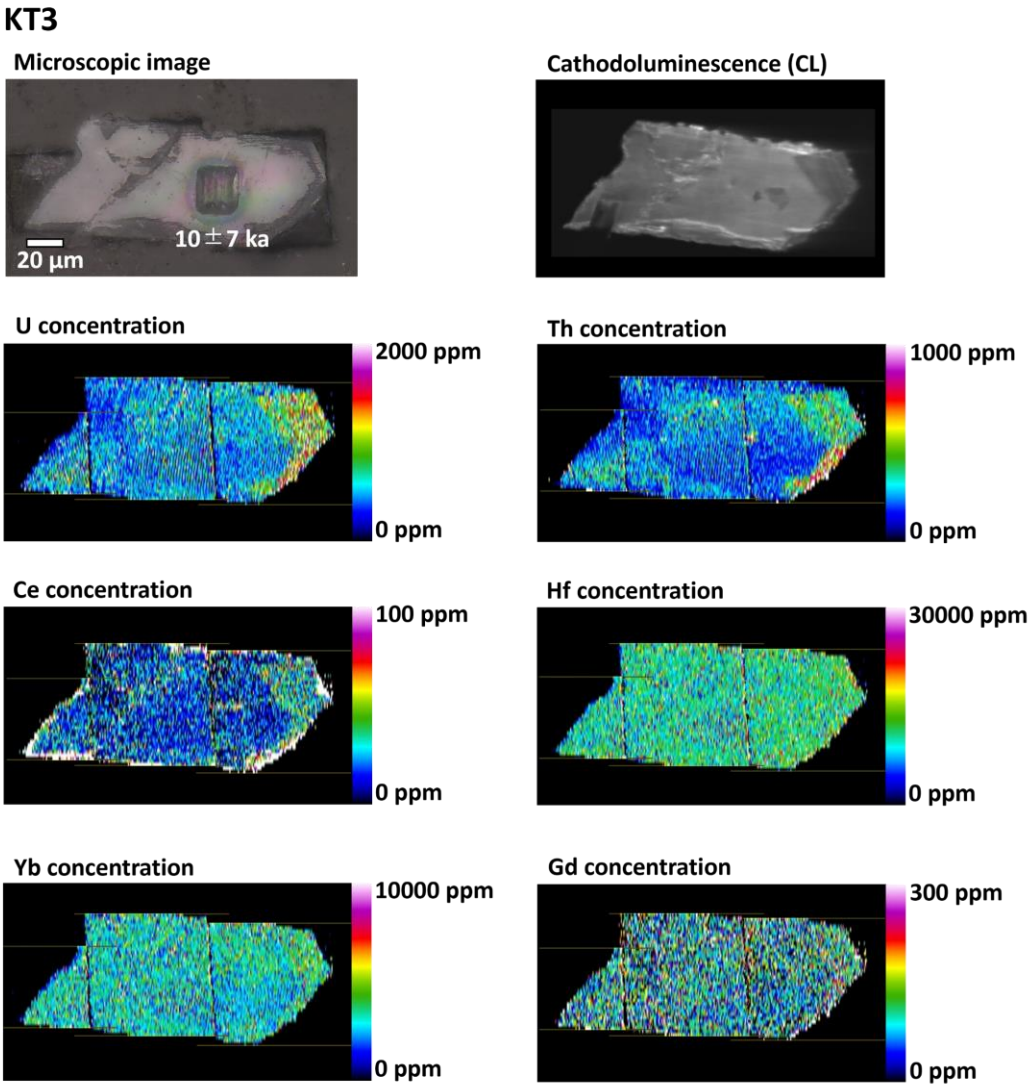

Figure 4.4 Optical microscopic, cathodoluminescence, and trace-element images for the analysed zircon of KT3. The ^{238}U–^{230}Th ages plotted on the optical microscopic images are two-point isochron ages calculated based on the combination with the previously reported data of glass.[140)]

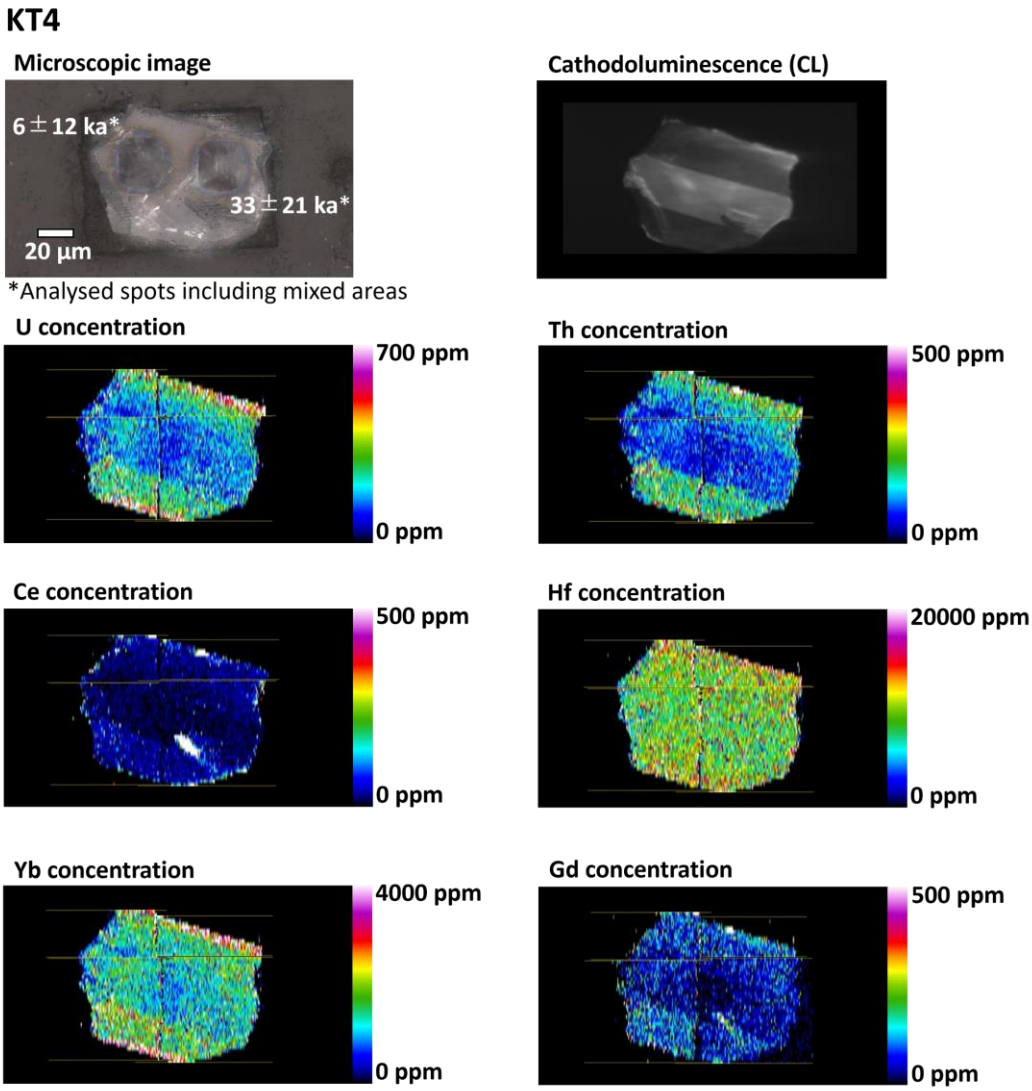

Figure 4.5 Optical microscopic, cathodoluminescence, and trace-element images for the analysed zircon of KT4. The ^{238}U–^{230}Th ages plotted on the optical microscopic images are two-point isochron ages calculated based on the combination with the previously reported data of glass.[140)]

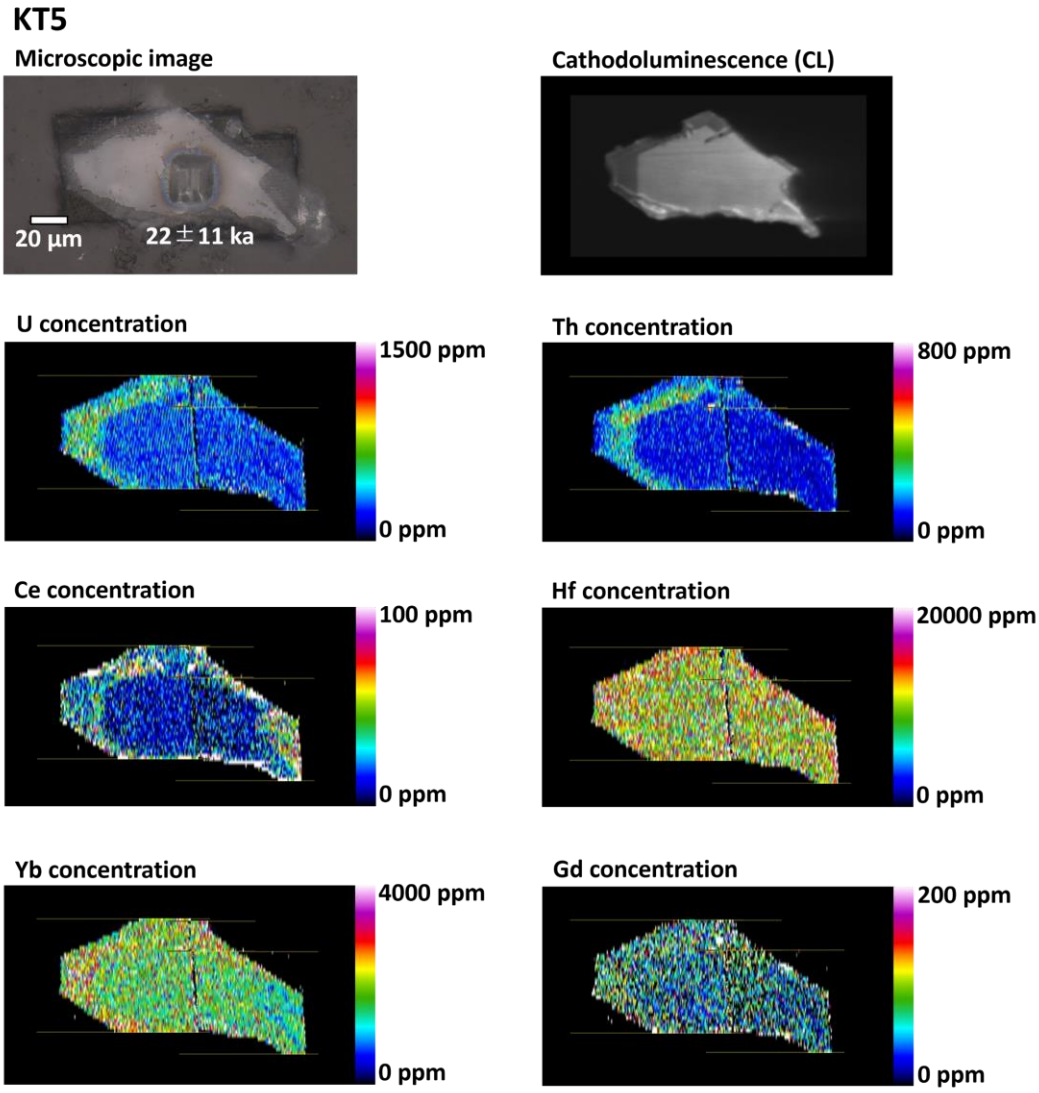

Figure 4.6 Optical microscopic, cathodoluminescence, and trace-element images for the analysed zircon of KT5. The ^{238}U–^{230}Th ages plotted on the optical microscopic images are two-point isochron ages calculated based on the combination with the previously reported data of glass.[140)]

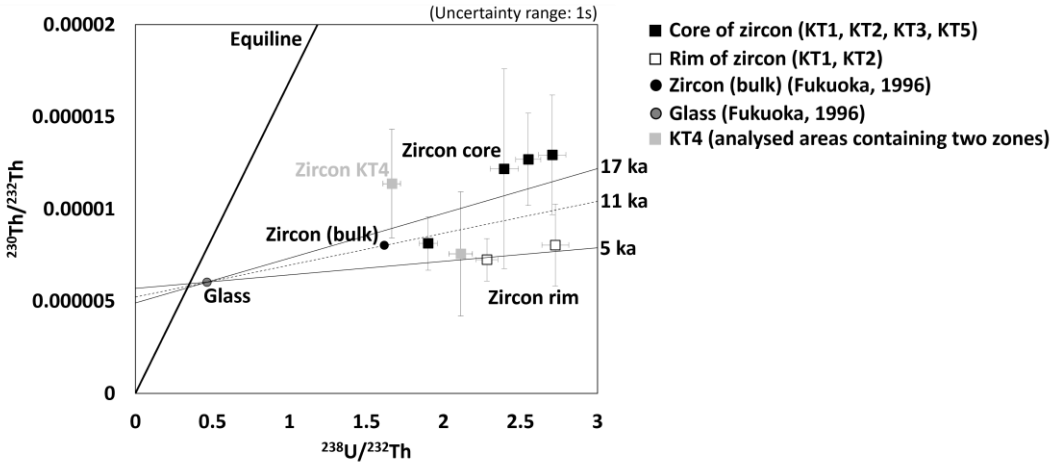

Figure 4.7 ^{238}U–^{230}Th isotope ratios plotted on the isochron diagram based on the obtained data and compiled data from Fukuoka (1996). The solid lines are the isochrons for the combination of the data for the zircon core and glass, and the zircon rim and glass. The dashed line corresponds the isochron of bulk analysis data of zircon and glass reported in Fukuoka (1996).[140)]

Chapter 5
Summary and outlook

The great ocean of truth lay all undiscovered before me. --- Isaac Newton.[147)]

Isaac Newton compared himself to a child playing on the seashore, facing the great ocean of truth. Similarly, we find ourselves merely standing on the seashore. Nevertheless, we must construct vessels and harbours rooted in analytical chemistry for exploration of the great ocean of truth in geochronology.

Summary

Among mass spectrometric techniques, ICP-MS with the high kinetic- and excitation-temperature ion source is a primary option for isotope analysis of Th demonstrating the refractory feature. The combination of ICP and LA sampling technique (LA-ICP-MS) without chemical decomposition and dilution of samples offers decisive advantages due to its high signal-to-background ratios for analytes and the capability for age determination with sufficiently high spatial resolution, enabling the analysis of individual grains or sub-grain textures.

Despite the importance of LA-ICP-MS, there are two major sources of errors for isotope analysis. First is derived from the analytical technique based on LA-ICP-MS. The analytical errors with mass spectrometry are further divided into mass spectrometric and non-spectral interferences. Second is originating from geological samples having multiple chronological information about formation processes. Based on the bulk analysis of geological samples, the resulting radioisotope age can be erroneous due to the mixed or averaged chronological information about multiple events. In this study, these issues were investigated for acquiring better analytical results using LA-ICP-MS.

The non-spectral interference derived from LA was investigated by the isotopic analysis of individual particles generated by LA through the combination of HTR-MC-ICP-MS and micron-resolution femtosecond LA systems. In this study, the $^{208}Pb/^{232}Th$ values and reduced diameters of the LA-generated particles monazite were determined for the elucidation of the behaviours for refractory and volatile elements. The measured values for $^{208}Pb/^{232}Th$ demonstrates the presence of the particles with the decoupled two components. The Pb-bearing particles can be generated through condensation from gas phases based on the difference in the size distribution depending on the atmospheric gas during LA. The larger number of coarser particles generated under the Ar atmosphere compared to the He atmosphere is attributed to the expanded volume of the LA-induced plume. The low thermal conductivity and high viscosity of Ar leads to the smaller-sized LA-induced plume than He, and the resulting particles can be coarser. The Pb-depleted particles have similar size distribution for both the He and Ar atmospheres during LA, and this indicates that these particles were released from the sub-surface molten region without undergoing condensational process from the vapor phases. The distribution of

elements between the gas phase and remaining liquid phase can depend on the physicochemical properties of elements themselves and sample matrices, the analytical error for elemental ratios due to the different transport efficiency in the condensational particles and the molten particles can be significant in geochronological studies.

The generation of coarse Pb-depleted particles can also cause the analytical error. When the coarse particles (e.g., 300 nm) is introduced into ICP, the resulting ion signal intensity are more than 3×10^7 counts per second. The intense signal can paralyse the ion detector based on the pulse-counting system. The counting loss of ^{232}Th due to the paralysation leads to the overestimation of ^{208}Pb/^{232}Th for a high-Th-content samples, resulting in the older ^{232}Th–^{208}Pb age than the actual value. To avoid the error, age calculation based on the Pb-bearing particles without using Pb-depleted particles is necessary, and through the analysis of the Namaqualand monazite and the 44069 monazite, the improved accuracy of the ^{232}Th–^{208}Pb dating method for monazite with the discrimination of Pb-depleted and Pb-bearing particles using HTR-MC-ICP-MS was demonstrated.

The second issue concerning the mass spectrometric interference at *m*/*z* 230 is problematic for the in situ ^{238}U–^{230}Th dating method of minerals, especially zircon. The major interference ions are polyatomic ions, such as $Zr_2O_3^+$, and the tailing from the adjacent peak of $^{232}Th^+$. In conventional sector-field-based ICP-MS, the contribution of the interfering ions is significant, and the complicated correction scheme for them is required for accurate age determination. In this study, kinetic energy discrimination (KED) using collision cell technique (CCT) is utilised for the removal of the interfering ions. The KED mode is an effective method for eliminating polyatomic ions according to the larger collision cross section compared to $^{230}Th^+$, and the thermalisation of ion beams improved the abundance sensitivity. After the optimisation of the KED condition, the ^{238}U–^{230}Th isotope analyses of zircon references demonstrate the analytical accuracy of the present technique with the negligible contribution of the interfering ions. Hence, the *in situ* ^{238}U– ^{230}Th dating method using LA-ICP-MS can be carried without interference correction scheme.

Unlike the two issues related to mass spectrometry, the third issue come from geological samples formed through multiple events. Mineral samples crystallised in the magma reservoir can have internal zoning textures reflecting each growth stage during

the formation processes. The bulk analysis of them can yield erroneous ages, and *in situ* analysis for each texture is necessary. To resolve growth textures inside minerals, trace-element imaging analysis is important because of elemental concentrations or elemental ratios reflecting the formation conditions. Despite the importance of elemental imaging, conventional LA-ICP-MS systems lack in spatial resolutions, mainly due to the size of laser beam (e.g., > 10 μm). The resulting spatial resolution achieved by the LA-ICP-MS is generally poorer than those obtained by electron microscopy or secondary ion mass spectrometry, and the spatial resolution of LA-ICP-MS imaging is often insufficient for distinguishing micron-scaled zonation inside mineral samples. In this study, to overcome this, the micron-resolution femtosecond LA system is newly developed. the ablation pit sizes can be minimised to 2 μm, and multiple elemental analysis for trace-elements being > 10 μg g^{-1} can be made. To demonstrate the analytical capability of the present system, imaging analysis was conducted on zircon from Ashizuri. For comparison, imaging analysis was conducted by conventional laser ablation system (i.e., ablation pit size of 10–20 μm), and the spatial resolution could be effectively improved by the present system setup. Moreover, mapping images for U and Th revealed that the zircon crystal was grown up through multiple step growth stages, and this is a critical advantage against imaging methods that cannot quantify trace-elemental concentration.

Finally, the developed technique was applied to geochronological study on zircon separated from a Holocene rhyolite lava occurring in Mt. Tenjo, Kozushima. The trace-element imaging analysis was conducted for zircons prior to ^{238}U–^{230}Th age determination. Based on the acquired elemental images, the zircons demonstrate the zoning texture of the core with low concentrations of incompatible elements and the rim with high concentrations of them. There is a strong negative correlation between the U, Th, and Ce concentrations and the cathodoluminescence intensity. The separate ^{238}U–^{230}Th dating of the core and rim were conducted, and the resulting ^{238}U–^{230}Th ages were 17 ± 5 ka (1s) and 5 ± 4 ka (1s), respectively. The obtained age data of the core and rim imply two-stage formation processes of zircon within the magma reservoir. The core age can correspond to the timing of the former eruptive activity in the relevant area, and the rim can be attributed to the magmatic intrusion potentially triggering the latest eruptive activity. The obtained results for ^{238}U–^{230}Th ages indicate that the combination of the high-spatial-resolution elemental imaging analysis and *in situ* ^{238}U–^{230}Th dating method

based on LA-ICP-MS can be an important tool for understanding detailed magmatic processes with a high temporal resolution.

Outlook

Further improvements in LA-ICP-MS are important for advances in geochronology. Regarding future directions, there are two key approaches. The first strategy is accurate elemental/isotopic analysis without matrix-matched references, and the second is high-speed imaging analysis.

As for matrix-matched references, research on zircon has advanced because of the numerous well-characterised zircon references for elemental and isotopic analysis. Hence, studies throughout the entire history of the Earth primarily rely on zircon-oriented geochronology. However, minerals other than zircon typically lack matrix-matched references, and the development of novel dating methods for them requires the development of matrix-matched references. Due to the necessity of matrix-matched references, multi-geochronological studies based on the comparison of various chronological data have been still retarded.

In this study, we have developed the new method for elemental and isotopic analysis of individual particles generated by LA, and this technique spearheads advancements in understanding the fundamental reasons behind the analytical errors. In this study, the behaviour of Th and Pb during LA is investigated as a representative of refractory and volatile elements. To grasp the general trends depending on the difference in volatility, studies on various elements with the wide range of melting and boiling points are required by using the analytical protocol developed in this study. Based on another finding in this study, paralysation of ion detectors is a cause of analytical errors arising from the fact that elemental and isotopic analysis using LA-ICP-MS is the summation of analyses for individual particles. This indicates that the development of the ion detector with the extensive dynamic range is necessary for accurate measurements for particles across a wide size range. The continuous efforts to comprehend the causes of analytical errors will lead to accurate elemental and isotopic analysis without calibration based on matrix-matched references. If matrix-matched references become unnecessary, multi-geochronology could advance, and ultimately, it might lead to the discovery of Hadean minerals, which so far has only been found in zircon.

High-speed imaging analysis is also important for acquisition of reliable chronological data from minerals. In this study, the spatial resolution of the present

technique is enough high for resolving the internal textures of minerals. Despite this, the analysis throughput of the present system setup is much slower than the CL imaging technique commonly used for geochronology. Hence, the acceleration of elemental imaging analysis is required through improvements in the mechanism of the particle transport from the LA sample chamber. The combination of high-speed elemental imaging analysis for various geological samples (hereafter referred to as geoimaging) and multi-geochronology based on radioisotope dating methods for diverse minerals will pave the way for hybrid geochronology beyond zircon geochronology, where geochemical and chronological insights are integrated.

Toward future direction in Quaternary geochronology, three approaches are important; the development of reference materials, ^{238}U–^{230}Th dating of low-U-concentration minerals, and radioisotope dating based on further younger samples. The first is necessary to ensure traceability of the measurements through the mutual comparison of ^{238}U–^{230}Th age data for age reference minerals among researchers and laboratories. As reference materials, homogeneity in terms of ^{238}U–^{230}Th ages is required. From the ^{238}U–^{230}Th ages obtained in this study, zircon from the Toya tephra is promising for the Quaternary reference because of the absence of old xenocrysts.

The second is essential for the age determination of rocks without zircon and monazite. Zircon and monazite analysed in this study mainly occurs in felsic volcanic rocks with high U and Th concentrations, while other rocks with lower U and Th concentrations compared to felsic rocks, such as mafic rocks, sometimes barely contains them. Hence, the potential application of zircon and monazite chronometers can be often restricted to felsic igneous activities. Then, candidates for age determination other than zircon and monazite are ilmenite and calcite. Despite the low U concentrations of ilmenite and calcite, they have high U/Th like zircon.[148, 149] For precise ^{238}U–^{230}Th age determination of those minerals occurring in zircon-absent rocks, the developed technique in this study will be advantageous in terms of the high SBR, and further improvements in the sensitivity of the present technique will be also important for high-precision age determination.

Third direction is radioisotope dating of further younger samples compared to the analysed samples in this study. The precise age determination for those young samples can be achieved with the radioisotope dating methods utilising nuclides with shorter half-

lives than ^{230}Th, such as ^{231}Pa and ^{226}Ra. Accurate analysis of ^{231}Pa is important for the ^{235}U–^{231}Pa dating method of minerals, and through evaluation of the concordance of the ^{238}U–^{230}Th and ^{235}U–^{231}Pa isotope systematics, the reliability of age determinations can be improved as well as the combination of the ^{238}U–^{206}Pb and ^{235}U–^{207}Pb isotope systems. Radioisotope dating methods based on ^{226}Ra can be applied to conventionally subsidised U-enriched or Th-enriched minerals and Ra-enriched minerals. Radium demonstrates the compatibility with K-bearing minerals because of the large ionic radius, and novel chronological data can be derived from K-bearing rock-forming minerals, especially for elucidating alkaline magmatism.

The major problems with the isotope analysis of these nuclides are the necessity of higher selectivity and sensitivity compared to the present system setup. Since the abundance of these isotopes is two orders of magnitude less than that of ^{230}Th, the measurements of them are more susceptible to errors derived from mass spectrometric interference and counting statistics of low ion signals. The further selectivity can be achieved by utilising the MS/MS with collision cell technique, which has two mass filter before and after the collision cell. The resulting abundance sensitivity is better than 1 ppb, and even ^{231}Pa adjacent to the intense ^{232}Th peak on mass spectrum can be analysed without background counts. Hence, the insufficient sensitivity of ICP-MS is more problematic than the selectivity. One potential approach is utilising sector-field-based MS with CCT instead of quadrupole-based MS. The typical ion transmission of sector-field-based-MS is one order of magnitude higher than that of quadrupole-based MS. Despite the potential improvement in the ion transmission, the sensitivity will be still insufficient. The major cause for loss of ions is the vacuum interface of the ICP-MS system. Through the vacuum interface, more than 90% of the produced ions inside the atmospheric ICP is lost due to the evacuation. To deal with the problem, further improvements towards the suppression of ion loss through the vacuum interface is required. Then, optimisation of the vacuum interface region of the ICP-MS system will be necessary, especially for the angle of the orifice in the sampling cone, which is a key factor for supressing the ion expansion in the vacuum region.[97] As the efficiency of extracting ions from ICP improves, the intake of atmospheric O_2 and N_2 increases as well, resulting in a higher production rate of polyatomic interfering ions. Hence, the technique of removing interferences using the CCT presented in this study will become even more important. Ultimately, ionisation

under vacuum conditions can enhance the ion transmission during introduction of ions into a mass spectrometer operating under vacuum conditions. Therefore, we must develop an ion source with high ionisation capacity comparable to ICP operating under vacuum conditions. While the problem faced is substantial, continuous efforts will pave the way for high-temporal-resolution geochronology.

Bibliography

1 Chinese Text Project (中國哲學書電子化計劃), https://ctext.org/dictionary.pl?if=gb&id=9289, (accessed December 12, 2023).

2 A. Holmes, *Nature*, 1913, **91**, 343–344.

3 P. R. Renne, W. D. Sharp, A. L. Deino, G. Orsi and L. Civetta, *Science*, 1997, **277**, 1279–1280.

4 P. E. Damon, J. C. Lerman and A. Long, *Annual Review of Earth and Planetary Sciences*, 1978, **6**, 457–494.

5 M. R. Reid, C. D. Coath, T. Mark Harrison and K. D. McKeegan, *Earth and Planetary Science Letters*, 1997, **150**, 27–39.

6 S. M. White, J. A. Crisp and F. J. Spera, *Geochemistry, Geophysics, Geosystems*, 2006, **7**, Q03010.

7 E. C. Anderson, W. F. Libby, S. Weinhouse, A. F. Reid, A. D. Kirshenbaum and A. V. Grosse, *Science*, 1947, **105**, 576–577.

8 J. R. Arnold, *Science*, 1956, **124**, 584–585.

9 K. S. Heier, *Nature*, 1965, **208**, 479–480.

10 A. J. Dempster, *Nature*, 1935, **136**, 180–180.

11 E. Rutherford and B. A. F. Soddy, *The London, Edinburgh, and Dublin Philosophical Magazine and Journal of Science*, 1902, **4**, 370–396.

12 J. L. Rose and R. K. Stranathan, *Phys. Rev.*, 1936, **50**, 792–796.

13 A. O. Nier, *Phys. Rev.*, 1939, **55**, 150–153.

14 G. W. Wetherill, *Eos, Transactions American Geophysical Union*, 1956, **37**, 320–326.

15 *Chronological scientific tables (Rikanenpyo)*, Maruzen Publishing Co., Ltd., Tokyo, 2022.

16 U. Schärer, *Earth and Planetary Science Letters*, 1984, **67**, 191–204.

17 S. Sakata, S. Hirakawa, H. Iwano, T. Danhara, M. Guillong and T. Hirata, *Quaternary Geochronology*, 2017, **38**, 1–12.

18 J. N. Rosholt, *Anal. Chem.*, 1954, **26**, 1307–1311.

19 M. de Bruin, *Pure and Applied Chemistry*, 1982, **54**, 1533–1554.

20 B. L. K. Somayajulu, M. Tatsumoto, J. N. Rosholt and R. J. Knight, *Earth and Planetary Science Letters*, 1966, **1**, 387–391.

21 M. Condomines, Ch. Hemond and C. J. Allègre, *Earth and Planetary Science Letters*, 1988, **90**, 243–262.

22 T. Fukuoka and K. Kigoshi, *Geochemical Journal*, 1974, **8**, 117–122.

23 A. K. Schmitt, *American Mineralogist*, 2007, **92**, 691–694.

24 P. Boehnke, M. Barboni and E. A. Bell, *Quaternary Geochronology*, 2016, **34**, 69–74.

25 S. Sakata, *Geochem. J.*, 2018, **52**, 281–286.

26 S. Barth, F. Oberli and M. Meier, *Earth and Planetary Science Letters*, 1994, **124**, 149–159.

27 K. Kigoshi, *Science*, 1967, **156**, 932–934.

28 H. Cheng, R. Lawrence Edwards, C.-C. Shen, V. J. Polyak, Y. Asmerom, J. Woodhead, J. Hellstrom, Y. Wang, X. Kong, C. Spötl, X. Wang and E. Calvin Alexander, *Earth and Planetary Science Letters*, 2013, **371–372**, 82–91.

29 E. B. Watson, *Contr. Mineral. and Petrol.*, 1979, **70**, 407–419.

30 R. H. Steiger and G. J. Wasserburg, *Journal of Geophysical Research (1896-1977)*, 1966, **71**, 6065–6090.

31 W. Compston and R. T. Pidgeon, *Nature*, 1986, **321**, 766–769.

32 S. A. Wilde, J. W. Valley, W. H. Peck and C. M. Graham, *Nature*, 2001, **409**, 175–178.

33 D. J. Cherniak, W. A. Lanford and F. J. Ryerson, *Geochimica et Cosmochimica Acta*, 1991, **55**, 1663–1673.

34 J. Blundy and B. Wood, *Reviews in Mineralogy and Geochemistry*, 2003, **52**, 59–123.

35 M. Guillong, J. T. Sliwinski, A. Schmitt, F. Forni and O. Bachmann, *Geostandards and Geoanalytical Research*, 2016, **40**, 377–387.

36 R. P. Rapp and E. B. Watson, *Contr. Mineral. and Petrol.*, 1986, **94**, 304–316.

37 J. P. Marble, *American Mineralogist*, 1936, **21**, 456–457.

38 K. Suzuki and M. Adachi, *Geochemical Journal*, 1991, **25**, 357–376.

39 S. Skora and J. Blundy, *Journal of Petrology*, 2010, **51**, 2211–2243.

40 A. S. Stepanov, J. Hermann, D. Rubatto and R. P. Rapp, *Chemical Geology*, 2012, **300–301**, 200–220.

41 S. Niki, S. Kosugi, H. Iwano, T. Danhara and T. Hirata, *Geostandards and Geoanalytical Research*, 2022, **46**, 589–602.

42 A. Kleinert, *N.T.M.*, 2009, **17**, 199–206.

43 A. O. Nier, *Review of Scientific Instruments*, 2004, **11**, 212–216.

44 T. E. Krogh, *Geochimica et Cosmochimica Acta*, 1973, **37**, 485–494.

45 D. M. Wayne, W. Hang, D. K. McDaniel, R. E. Fields, E. Rios and V. Majidi,

International Journal of Mass Spectrometry, 2002, **216**, 41–57.

46 A. K. Schmitt, *Annual Review of Earth and Planetary Sciences*, 2011, **39**, 321–349.

47 G. D. Layne and K. W. Sim, *International Journal of Mass Spectrometry*, 2000, **203**, 187–198.

48 O. Bachmann, B. L. A. Charlier and J. B. Lowenstern, *Geology*, 2007, **35**, 73–76.

49 R. A. Stern and Y. Amelin, *Chemical Geology*, 2003, **197**, 111–142.

50 R. C. Marsden, C. L. Kirkland, M. Danišík, M. L. Daggitt, U.-S. Ahn, B. Friedrichs and N. J. Evans, *Computers & Geosciences*, 2022, **158**, 104947.

51 R. S. Houk, V. A. Fassel, G. D. Flesch, H. J. Svec, A. L. Gray and C. E. Taylor, *Anal. Chem.*, 1980, **52**, 2283–2289.

52 H. Niu and R. S. Houk, *Spectrochimica Acta Part B: Atomic Spectroscopy*, 1996, **51**, 779–815.

53 S. D. Tanner, *J. Anal. At. Spectrom.*, 1993, **8**, 891.

54 R. S. Houk and N. Praphairaksit, *Spectrochimica Acta Part B: Atomic Spectroscopy*, 2001, **56**, 1069–1096.

55 K. Itano and T. Iizuka, *J. Anal. At. Spectrom.*, 2017, **32**, 2003–2010.

56 E. Bolea-Fernandez, A. Rua-Ibarz, M. Velimirovic, K. Tirez and F. Vanhaecke, *J. Anal. At. Spectrom.*, 2020, **35**, 455–460.

57 S. Fukuda and S. Nakai, *Geochemical Journal*, 2002, **36**, 465–473.

58 R. F. Browner and A. W. Boorn, *Analytical Chemistry*, 1984, **56**, 786A-798A.

59 A. L. Gray, *Analyst*, 1985, **110**, 551–556.

60 I. Horn and D. Günther, *Applied Surface Science*, 2003, **207**, 144–157.

61 T. Hirata and Z. Miyazaki, *Anal. Chem.*, 2007, **79**, 147–152.

62 T. Hirata and R. W. Nesbitt, *Geochimica et Cosmochimica Acta*, 1995, **59**, 2491–2500.

63 H.-R. Kuhn and D. Günther, *Journal of Analytical Atomic Spectrometry*, 2004, **19**, 1158–1164.

64 D. Günther and C. A. Heinrich, *J. Anal. At. Spectrom.*, 1999, **14**, 1369–1374.

65 R. E. Russo, X. Mao, J. J. Gonzalez and S. S. Mao, *J. Anal. At. Spectrom.*, 2002, **17**, 1072–1075.

66 J. Koch, M. Wälle, J. Pisonero and D. Günther, *J. Anal. At. Spectrom.*, 2006, **21**, 932–940.

67 M. Guillong, A. K. Schmitt and O. Bachmann, *Journal of Volcanology and Geothermal Research*, 2015, **296**, 101–103.

68 J. M. Hanchar and C. F. Miller, *Chemical Geology*, 1993, **110**, 1–13.

69 L. Nasdala, M. Zhang, U. Kempe, G. Panczer, M. Gaft, M. Andrut and M. Plötze, *Reviews in Mineralogy and Geochemistry*, 2003, **53**, 427–467.

70 C. Pineda, A. K. Schmitt and D. Morata, *Chemical Geology*, 2022, **603**, 120911.

71 D. Chew, K. Drost, J. H. Marsh and J. A. Petrus, *Chemical Geology*, 2021, **559**, 119917.

72 T. Lee, D. A. Papanastassiou and G. J. Wasserburg, *Geochimica et Cosmochimica Acta*, 1977, **41**, 1473–1485.

73 N. M. W. Roberts, E. T. Rasbury, R. R. Parrish, C. J. Smith, M. S. A. Horstwood and D. J. Condon, *Geochemistry, Geophysics, Geosystems*, 2017, **18**, 2807–2814.

74 W.-T. Chan, X. L. Mao and R. E. Russo, *Appl. Spectrosc., AS*, 1992, **46**, 1025–1031.

75 M. Thompson, J. E. Goulter and F. Sieper, *Analyst*, 1981, **106**, 32–39.

76 A. Ben-Yakar, A. Harkin, J. Ashmore, R. L. Byer and H. A. Stone, *J. Phys. D: Appl. Phys.*, 2007, **40**, 1447.

77 P. Shaw and A. Donard, *Journal of Analytical Atomic Spectrometry*, 2016, **31**, 1234–1242.

78 A. Donard, F. Claverie, F. Pointurier, C. Blitz Frayret, B. Svatosova and C. Pécheyran, *Anal. Chem.*, 2017, **89**, 8791–8799.

79 T. Hirata, S. Yamashita, M. Ishida and T. Suzuki, *Mass Spectrometry*, 2020, **9**, A0085–A0085.

80 T. Hirata, S. Niki, S. Yamashita, H. Asanuma and H. Iwano, *J. Anal. At. Spectrom.*, 2021, **36**, 70–74.

81 A. Tunheng and T. Hirata, *Journal of Analytical Atomic Spectrometry*, 2004, **19**, 932–934.

82 A. Simonetti, L. M. Heaman, T. Chacko and N. R. Banerjee, *International Journal of Mass Spectrometry*, 2006, **253**, 87–97.

83 R. H. Steiger and E. Jäger, *Earth and Planetary Science Letters*, 1977, **36**, 359–362.

84 J. N. Aleinikoff, W. S. Schenck, M. O. Plank, L. Srogi, C. M. Fanning, S. L. Kamo and H. Bosbyshell, *GSA Bulletin*, 2006, **118**, 39–64.

85 M. Knoper, R. A. Armstrong, M. A. G. Andreoli and L. D. Ashwal, *Journal of African Earth Sciences*, 2000, **31**, 38–39.

86 T. Hokada, K. Horie, T. Adachi, Y. Osanai, N. Nakano, S. Baba and T. Toyoshima, *Precambrian Research*, 2013, **234**, 183–209.

87 K. P. Jochum, U. Weis, B. Stoll, D. Kuzmin, Q. Yang, I. Raczek, D. E. Jacob, A.

Stracke, K. Birbaum, D. A. Frick, D. Günther and J. Enzweiler, *Geostandards and Geoanalytical Research*, 2011, **35**, 397–429.

88 A. J. Walder, I. D. Abell, I. Platzner and P. A. Freedman, *Spectrochimica Acta Part B: Atomic Spectroscopy*, 1993, **48**, 397–402.

89 X. Tang, Q.-L. Li, B. Zhang, P. Wang, L.-X. Gu, X.-X. Ling, C.-H. Fei and J.-H. Li, *Minerals*, 2020, **10**, 504.

90 Y. Hikichi and T. Nomura, *Journal of the American Ceramic Society*, 1987, **70**, C-252-C–253.

91 H. Ito, *Journal of Volcanology and Geothermal Research*, 2014, **289**, 210–223.

92 J. P. Bernal, L. A. Solari, A. Gómez-Tuena, C. Ortega-Obregón, L. Mori, M. Vega-González and D. G. Espinosa-Arbeláez, *Quaternary Geochronology*, 2014, **23**, 46–55.

93 S. D. Tanner and V. I. Baranov, *J. Am. Soc. Mass Spectrom.*, 1999, **10**, 1083–1094.

94 J. T. Rowan and R. S. Houk, *Appl. Spectrosc., AS*, 1989, **43**, 976–980.

95 S. F. Boulyga and J. S. Becker, *J. Anal. At. Spectrom.*, 2002, **17**, 1202–1206.

96 D. J. Douglas and J. B. French, *J. Anal. At. Spectrom.*, 1988, **3**, 743–747.

97 M. Nakazato, H. Asanuma, S. Niki, H. Iwano and T. Hirata, *Geostandards and Geoanalytical Research*, 2022, **46**, 603–620.

98 Y. Makino, Y. Kuroki and T. Hirata, *J. Anal. At. Spectrom.*, 2019, **34**, 1794–1799.

99 M. Wiedenbeck, P. Allé, F. Corfu, W. l. Griffin, M. Meier, F. Oberli, A. V. Quadt, J. c. Roddick and W. Spiegel, *Geostandards Newsletter*, 1995, **19**, 1–23.

100 A. B. Chase and J. A. Osmer, *J. Electrochem. Soc.*, 1966, **113**, 198.

101 J. Sláma, J. Košler, D. J. Condon, J. L. Crowley, A. Gerdes, J. M. Hanchar, M.

S. A. Horstwood, G. A. Morris, L. Nasdala, N. Norberg, U. Schaltegger, B. Schoene, M. N. Tubrett and M. J. Whitehouse, *Chemical Geology*, 2008, **249**, 1–35.

102 S. E. Jackson, N. J. Pearson, W. L. Griffin and E. A. Belousova, *Chemical Geology*, 2004, **211**, 47–69.

103 H. Iwano, Y. Orihashi, T. Hirata, M. Ogasawara, T. Danhara, K. Horie, N. Hasebe, S. Sueoka, A. Tamura, Y. Hayasaka, A. Katsube, H. Ito, K. Tani, J.-I. Kimura, Q. Chang, Y. Kouchi, Y. Haruta and K. Yamamoto, *Island Arc*, 2013, **22**, 382–394.

104 A. H. Jaffey, K. F. Flynn, L. E. Glendenin, W. C. Bentley and A. M. Essling, *Phys. Rev. C*, 1971, **4**, 1889–1906.

105 Y. Goto, K. Suzuki, T. Shinya, A. Yamauchi, M. Miyoshi, T. Danhara and A. Tomiya, *Journal of Geography (Chigaku Zasshi)*, 2018, **127**, 191–227.

106 M. Shirai, R. Tada and K. Fujioka, *The Quaternary Research (Daiyonki-Kenkyu)*, 1997, **36**, 183–196.

107 A. Tomiya and I. Miyagi, *Bulletin of the Volcanological Society of Japan*, 2020, **65**, 13–18.

108 J.-I. Kimura, S. Okada, K. Nakayama, K. Umeda, T. Kusano, Y. Asahara, M. Tateno and T. Danhara, *The Quaternary Research (Daiyonki-Kenkyu)*, 1999, **38**, 145–155.

109 H. Machida and F. Arai, *Atlas of tephra in and around Japan*, University of Tokyo Press., Second edition.

110 H. Nishiyama, A. Hayashida, Y. Sawada, T. Danhara and S. Kawano, Sapporo, 2014.

111 T. Fukuoka and S. Matsui, *Earth Science (Chikyu Kagaku)*, 2002, **56**, 105–122.

112 S. Maruyama, K. Takemura, T. Hirata, T. Yamashita and T. Danhara, *Journal of Geography (Chigaku Zasshi)*, 2019, **128**, 879–903.

113 J.-I. Kimura, T. Kunikiyo, I. Osaka, T. Nagao, S. Yamauchi, S. Kakubuchi, S. Okada, N. Fujibayashi, R. Okada, H. Murakami, T. Kusano, K. Umeda, S. Hayashi, T. Ishimaru, A. Ninomiya and A. Tanase, *Island Arc*, 2003, **12**, 22–45.

114 S. Kameyama, S. Shimoyama, S. Miyabe, Y. Miyata, T. Sugiyama, H. Iwano, T. Danhara, K. Endo and A. Matsukuma, *The Quaternary Research (Daiyonki-Kenkyu)*, 2005, **44**, 15–29.

115 D. York, *Earth and Planetary Science Letters*, 1968, **5**, 320–324.

116 K. I. Mahon, *International Geology Review*, 1996, **38**, 293–303.

117 K. R. Ludwig, *Geochimica et Cosmochimica Acta*, 1998, **62**, 665–676.

118 K. Yamamoto, H. Asanuma, H. Takahashi and T. Hirata, *J. Anal. At. Spectrom.*, 2021, **36**, 668–675.

119 J. S. Becker, M. Zoriy, A. Matusch, B. Wu, D. Salber, C. Palm and J. S. Becker, *Mass Spectrometry Reviews*, 2010, **29**, 156–175.

120 F. Corfu, J. M. Hanchar, P. W. O. Hoskin and P. Kinny, *Reviews in Mineralogy and Geochemistry*, 2003, **53**, 469–500.

121 P. Kuisma-Kursula, *X-Ray Spectrometry*, 2000, **29**, 111–118.

122 J. T. van Elteren and F. Vanhaecke, *J. Anal. At. Spectrom.*, 2016, **31**, 1998–2004.

123 T. D. Yokoyama, T. Suzuki, Y. Kon and T. Hirata, *Anal. Chem.*, 2011, **83**, 8892–8899.

124 Sawaki Y., Suzuki K., Asanuma H., Okabayashi S., Hattori K., Saito T. and Hirata T., *Island Arc*, 2017, **26**, e12216.

125 M. Wiedenbeck, J. M. Hanchar, W. H. Peck, P. Sylvester, J. Valley, M.

Whitehouse, A. Kronz, Y. Morishita, L. Nasdala, J. Fiebig, I. Franchi, J.-P. Girard, R. c. Greenwood, R. Hinton, N. Kita, P. r. d. Mason, M. Norman, M. Ogasawara, P. m. Piccoli, D. Rhede, H. Satoh, B. Schulz-Dobrick, O. Skår, Mj. Spicuzza, K. Terada, A. Tindle, S. Togashi, T. Vennemann, Q. Xie and Y.-F. Zheng, *Geostandards and Geoanalytical Research*, 2004, **28**, 9–39.

126 Hayashi S., Ishihara S. and Sakamaki Y., *Rept. Geol. Surv. Japan*, 1969, **232**, 93–103.

127 S. Ishihara and M. Hoshino, *Bull. Geol. Surv. Japan*, 2013, **64**, 1–24.

128 T. Suzuki, S. Sakata, Y. Makino, H. Obayashi, S. Ohara, K. Hattori and T. Hirata, *Mass Spectrometry*, 2018, **7**, A0065–A0065.

129 T. Iizuka and T. Hirata, *Geochem. J.*, 2004, **38**, 229–241.

130 S. Fourcade and C. J. Allegre, *Contr. Mineral. and Petrol.*, 1981, **76**, 177–195.

131 K. Suzuki, M. Adachi, K. Yamamoto and Y. Nakai, *Geochemical Journal*, 1992, **26**, 383–394.

132 J. Blundy and B. Wood, *Reviews in Mineralogy and Geochemistry*, 2003, **52**, 59–123.

133 S. Prowatke and S. Klemme, *Geochimica et Cosmochimica Acta*, 2006, **70**, 4513–4527.

134 A. Fairbanks, *The First Philosophers of Greece*, Kegan Paul, Trench, Trübner & Co. Ltd., London, 1898.

135 R. J. Stern, *Geological Society, London, Special Publications*, 2010, **338**, 7–34.

136 Y. Tamura and Y. Tatsumi, *Journal of Petrology*, 2002, **43**, 1029–1047.

137 S. Kodaira, T. Sato, N. Takahashi, A. Ito, Y. Tamura, Y. Tatsumi and Y. Kaneda, *Journal of Geophysical Research: Solid Earth*, 2007, **112**, B05104.

138 Y. Tamura, J. B. Gill, D. Tollstrup, H. Kawabata, H. Shukuno, Q. Chang, T. Miyazaki, T. Takahashi, Y. Hirahara, S. Kodaira, O. Ishizuka, T. Suzuki, Y. Kido, R. S. Fiske and Y. Tatsumi, *Journal of Petrology*, 2009, **50**, 685–723.

139 Y. Arakawa, D. Endo, J. Oshika, T. Shinmura and K. Ikehata, *Lithos*, 2019, **330–331**, 223–237.

140 K. Tani, R. S. Fiske, D. J. Dunkley, O. Ishizuka, T. Oikawa, I. Isobe and Y. Tatsumi, *Earth and Planetary Science Letters*, 2011, **303**, 225–239.

141 N. Isshiki, *Geology of the Kozushima district, Quadrangle Series, scale 1:50, 000.*, Geol. Surv. Jpn., 1982.

142 T. Yokoyama, A. Shimada, T. Umemura and S. Toyoda, *Bulletin of the Volcanological Society of Japan*, 2004, **49**, 23–32.

143 M. Murata, M. Kobayashi, K. Aoki, T. Takahashi, F. Nishizawa and T. Suzuki, *Journal of Geography (Chigaku Zasshi)*, 2021, **130**, 379–402.

144 H. Taniguchi, *Second Series Bulletin of the Volcanological Society of Japan*, 1980, **25**, 102–103.

145 Fukuoka T., *Chishitsu news*, 1996, **502**, 7–13.

146 P. Wessel, J. F. Luis, L. Uieda, R. Scharroo, F. Wobbe, W. H. F. Smith and D. Tian, *Geochemistry, Geophysics, Geosystems*, 2019, **20**, 5556–5564.

147 D. Brewster, *CHAPTER XXVII. In: Memoirs of the Life, Writings, and Discoveries of Sir Isaac Newton*, Cambridge University Press, Cambridge, 2010.

148 F. Keller, M. Guillong, R.-G. Popa and O. Bachmann, *Geostandards and Geoanalytical Research*, 2022, **46**, 465–475.

149 K. R. Ludwig, K. R. Simmons, B. J. Szabo, I. J. Winograd, J. M. Landwehr, A. C. Riggs and R. J. Hoffman, *Science*, 1992, **258**, 284–287.

Acknowledgements

I would like to show my deepest gratitude to my supervisor, Prof. Takafumi Hirata, for the guidance and instruction on how to behave as a scientific researcher. I am truly grateful to Mr. Hideyuki Obayashi, Mr. Kentaro Hattori, Dr. Shuhei Sakata, Dr. Hisashi Asanuma, and Dr. Yusuke Miyajima for teaching me the fundamentals of chronology and mass spectrometry since the beginning of my study, as well as for providing advice and encouragement. I am deeply thankful to Dr. Hideki Iwano and Mr. Tohru Danhara for careful preparation of zircon references and critical advice regarding geochronology. I would like to extend my sincere thanks to Mr. Tetsuya Tamaki and Mr. Junichi Kimura for their technical support and advice on laser ablation. I would like to express my gratitude to Dr. Shuji Yamashita and Mr. Masaki Nakazato for their advice based on their cutting-edge techniques in nanoparticle analysis, and Mr. Shuhei Kosugi, Dr. Kengo Ito, and Mr. Tairiku Kawashima for daily discussion in geochronology.

I would like to thank Prof. Tsuyoshi Iizuka, Prof. Tetsuo Kawakami, Mr. Shunpei Kudo, and Prof. Takeshi Imayama for kindly providing monazite references. I am indebted to Mr. Tatsuya Tamura and Ms. Yui Sasai for their support for field survey in Kozushima. My sincere appreciation is extended to Dr. Yusuke Sawaki and Prof. Tsuyoshi Komiya for technical support concerning electron-microscopic observations. My heartfelt appreciation goes to Dr. Kenta Yoshida, Dr. Hikaru Sawada, Dr. Ryosuke Oyanagi, Dr. Mitsuhiro Nagata, Dr. Hideyuki Hayashi, and Mr. Yoshiyuki Yasuike for scientific advice concerning petrology, mineralogy, and volcanology.

I would recognise the invaluable assistance in daily studies from laboratory members, Dr. Yuko Yamagata, Dr. Yoshiki Makino, Mr. Kota Yamamoto, Dr. Wataru Takahagi, Dr. Huihsin Khoo, Mr. Haruka Kikuchi, Dr. Ryota Fukai, Mr. Menghao Yang, Ms. Norika Numa, Ms. Mai Akamune, Ms. Haruka Nakano, Mr. Yuta Kemuyama, Mr. Eisei Tanaka, Mr. Kou Horikoshi, Ms. Kanoko Kurihara, Dr. Yuta Ijichi, Mr. Hiroki Nawa, Ms. Maki Uezono, Mr. Satoru Fujita, Ms. Xinya Zhao, Mr. Chihaya Kinoshita, and Ms.

Eri Onishi. I would like to pay my special regards to my elder sister, my father, and my late mother.

Appendix A

Publication lists

Publications (international journal)

1. **S. Niki**, S. Kosugi, H. Iwano, T. Danhara and T. Hirata, *Geostandards and Geoanalytical Research*, 2022, **46**, 589–602.

2. **S. Niki**, K. Yoshida, H. Sawada, R. Oyanagi and T. Hirata, *Journal of Mineralogical and Petrological Sciences*, 2022, **117**, 210814.

3. T. Hirata, **S. Niki**, S. Yamashita, H. Asanuma and H. Iwano, *J. Anal. At. Spectrom.*, 2021, **36**, 70–74.

4. N. Kasahara, **S. Niki**, E. Uchida, K. Yarimizu, R. Cheng and T. Hirata, *Heliyon*, 2021, **7**, e06752.

5. H. Shinjoe, Y. Orihashi, **S. Niki**, A. Sato, M. Sasaki, T. Sumii and T. Hirata, *Island Arc*, 2021, **30**, e12383.

6. R. Yamada, H. Sawada, S. Aoyama, W. Ouchi, **S. Niki**, M. Nagata, T. Takahashi and T. Hirata, *Journal of Mineralogical and Petrological Sciences*, 2021, **116**, 61–66.

7. K. Yoshida, **S. Niki**, H. Sawada and R. Oyanagi, *Journal of Mineralogical and Petrological Sciences*, 2021, **116**, 1–8.

8. K. Yoshida, **S. Niki**, H. Sawada, R. Oyanagi, T. Hirata, K. Asakura and T. Hirajima, *Lithos*, 2021, **398–399**, 106349.

9. M. Nakazato, H. Asanuma, **S. Niki**, H. Iwano and T. Hirata, *Geostandards and Geoanalytical Research*, 2022, **46**, 603–620.

10. A. Sakuma, A. Kano, Y. Kakizaki, H. Kato, A. Murata, H. Matsuda, T. Hirata and **S. Niki**, *Sedimentary Geology*, 2022, **442**, 106280.

11. H. Sawada, **S. Niki**, M. Nagata and T. Hirata, *Minerals*, 2022, **12**, 107.

12. E. Uchida, S. Nagano, **S. Niki**, K. Yonezu, Y. Saitoh, K.-C. Shin and T. Hirata, *Journal of Asian Earth Sciences: X*, 2022, **8**, 100111.

13. K. Kurihara, N. Numa, **S. Niki**, M. Akamune, M. Nakazato, S. Yamashita, S. Itoh and T. Hirata, *Geochemical Journal*, 2023, **57**, e9–e16.

14. E. Uchida, S. Nagano, **S. Niki**, K. Yonezu, T. Yokokura, R. Cheng and T. Hirata, *Heliyon*, 2023, **9**, e19734.

Publications (in Japanese)

1. 羽地俊樹, 山路敦, 仁木創太, 平田岳史, 地質学雑誌, 2019, **125**, 867–785.

2. 宮田和周, 長田充弘, 仁木創太, 服部健太郎, 大林秀行, 平田岳史, 大藤茂, 地質学雑誌, 2020, **126**, 251–266.

3. 羽地俊樹, 工藤崇, 仁木創太, 平田岳史, 地質学雑誌, 2023, **129**, 341–354.

4. 羽地俊樹, 佐藤大介, 仁木創太, 平田岳史, 地質学雑誌, 2023, **129**, 223–238.

Appendix B
Presentation lists

Presentation

1. **Sota Niki**, Hirochika Sumino, Masahiro Kobayashi, Hiroyuki Kagi, and Takafumi Hirata, Chris Ballentine, ”FTIR spectroscopy and noble gas mass spectrometry for a single olivine grain”, Japan Geoscience Union Meeting, May, 2019. [ポスター]

2. 仁木創太, 平田岳史, 岩野英樹, 坂田周平, “初期鉛を含む鉱物の U–Th–Pb 年代測定における Th–Pb 系列の有用性”, 日本質量分析学会同位体比部会, 11 月, 2019. [ポスター]

3. 仁木創太, 岩野秀樹, 坂田周平, 木村優斗, 平田岳史 ”高速多点フェムト秒レーザーアブレーション ICP 質量分析法を用いた高精度ウラン–トリウム–鉛年代測定法”, 2020 年度日本地球化学会第 67 回オンライン年会, 11 月, 2020. [オンライン口頭][学生優秀賞受賞]

4. **Sota Niki**, Hideki Iwano, Tsuyoshi Iizuka, and Takafumi Hirata, ” In-situ apatite Lu–Hf dating by LA-ICP-MS with a collision/reaction cell”, Japan Geoscience Union Meeting, July, 2020. [オンラインポスター]

5. **Sota Niki**, Kenta Yoshida, Hikaru Sawada, Ryosuke Oyanagi, and Takafumi Hirata, ” A Two Stage P-T-T History of the Sanbagawa Metamorphic Terrane Constrained by Grossular U–Pb Geochronology”, Goldschmidt Conference, June, 2020. [オンライ

ン口頭]

6. **Sota Niki**, Kenta Yoshida, Hikaru Sawada, Ryosuke Oyanagi, and Takafumi Hirata, ” 三波川変成帯五良津東部岩体中の高圧結晶質石灰岩に対する柘榴石ウラン–鉛年代測定”, Japan Geoscience Union Meeting, June, 2021. [オンライン口頭][学生優秀賞受賞]

7. 仁木創太, 小杉周平, 岩野英樹, 平田岳史, “高速多点フェムト秒レーザーアブレーション ICP トリプル四重極型質量分析法による局所ウラン–トリウムおよびウラン–プロトアクチニウム放射非平衡年代測定法”, 2021 年度日本地球化学会第 68 会オンライン年会, 9 月, 2021. [オンライン口頭]

8. 仁木創太, 河上哲生, 足立達朗, 宇野正起, 東野文子, 平田岳史, “東南極セール・ロンダーネ山地メーニパに産する泥質片岩中の灰礬柘榴石，チタン石および燐灰石ウラン–鉛年代”, 2021 年度鉱物科学会年会, 9 月, 2021. [オンライン口頭]

9. 仁木創太, 河上哲生, 足立達朗, 宇野正起, 東野文子, 平田岳史, “東南極セール・ロンダーネ山地メーニパに産する泥質片岩中の灰礬柘榴石，チタン石および燐灰石ウラン–鉛年代”, 2021 年度鉱物科学会年会, 9 月, 2021. [オンライン口頭]

10. 仁木創太, 小杉周平, 岩野英樹, 平田岳史, “レーザーアブレーション ICP トリプル四重極型質量分析法を用いた地質試料に含有されるウラン系列および

アクチニウム系列中間生成核種の局所分析”, 日本質量分析学会同位体比部会, 11 月, 2021. [オンライン口頭][最優秀発表賞受賞]

11. 仁木創太, 河上哲生, 足立達朗, 宇野正起, 東野文子, 平田岳史, ”東南極セール・ロンダーネ山地メーニパに産する泥質変成岩の柘榴石，チタン石および燐灰石ウラン–鉛年代系に基づく三種年代分析”, Japan Geoscience Union Meeting, May, 2022. [オンラインポスター]

12. 仁木創太, 小杉周平, 岩野英樹, 檀原徹, 平田岳史, “完新世試料年代分析のためのレーザーアブレーション ICP トリプル四重極型質量分析法を用いたウラン系列放射非平衡年代測定法の開発”, 第 70 回質量分析総合討論会, 6 月, 2022. [口頭]

13. **Niki, S.**, Kosugi, S., Iwano, H., Danhara, T., and Hirata, T., “In situ U-Th disequilibrium dating of Quaternary zircon samples utilising multiple-spot femtosecond laser ablation-ICP-triple quadrupole mass spectrometry”, Goldschmidt Conference, July, 2022. [口頭]

14. 仁木創太, 小杉周平, 岩野英樹, 檀原徹, 平田岳史, “モナズ石に対するレーザーアブレーション ICP-MS/MS を用いたウラン系列年代分析法”, 2022 年度日本地球化学会年会, 9 月, 2022. [口頭]

15. 仁木創太, 平田岳史, “単一粒子 ICP 質量分析法を用いたレーザーアブレーション生成粒子の個別元素分析”, 第 71 回質量分析総合討論会, 5 月, 2023. [ポ

スター]

16. 仁木創太, 小杉周平, 岩野英樹, 檀原徹, 平田岳史, “レーザーアブレーション ICP 質量分析法を用いた第四紀モナズ石の年代測定”, Japan Geoscience Union Meeting, May, 2023. [口頭][学生優秀賞受賞]

17. **Sota Niki**, Yusuke Sawaki, Tsuyoshi Komiya, and Takafumi Hirata, “Geoimaging: revolution in U–Pb geochronology”, KBSI JAST Conference, June, 2023. [口頭]

18. **Sota Niki**, Yusuke Sawaki, Tsuyoshi Komiya, and Takafumi Hirata, “Micron-resolution trace element imaging analysis utilising multiple-spot femtosecond laser ablation-ICP-mass spectrometry”, Goldschmidt Conference, July, 2023. [口頭]

19. 仁木創太, 平田岳史, “レーザーアブレーション分流 ICP 質量分析法による局所オスミウム同位体比分析法の開発”, 2023 年度日本地球化学会年会, 9 月, 2023. [口頭][学生優秀賞受賞]

20. 仁木創太, 平田岳史, “レーザーアブレーションにまつわるマトリクス効果の謎を解く”, 日本質量分析学会同位体比部会, 11 月, 2023. [口頭]